Structure Functions in Medium and the Polarized EMC Effect

Stephen Tronchin

This dissertation is submitted toward the degree in *Master of Philosophy*

Principal Supervisor: Professor Anthony Thomas

Co-Supervisor: Associate Professor James Zanotti

The University of Adelaide

School of Physical Sciences

Department of Physics

May 2018

Dedicated to the Holy Gremlin

Contents

Abstract

The ratio of the in-medium to free nucleon structure functions for both the unpolarized and polarized case is obtained using the bag model, along with the QMC model to incorporate the in-medium modifications to the structure functions. The unpolarized EMC effect, $F_2^*(x)/F_2(x)$, is compared to data and the trend is certainly observed. A prediction of the polarized EMC effect, $g_1^*(x)/g_1(x)$, is made and found to be almost identical to the unpolarized case. The in-medium modifications; the σ mean field, Fermi motion, and ω mean field are included into the calculations one at a time to see how the EMC ratio develops for both the unpolarized and polarized case, and to see which in-medium modifications play the dominant role in producing the EMC effect.

Declaration

I certify that this work contains no material which has been accepted for the award of any other degree or diploma in any university or other tertiary institution and, to the best of my knowledge and belief, contains no material previously published or written by another person, except where due reference has been made in the text. In addition, I certify that no part of this work, in the future, be used in a submission for any other degree or diploma in any university or other tertiary institution without the prior approval of the University of Adelaide and where applicable, any partner institution responsible for the joint-award of this degree.

I give consent to this copy of my thesis, when deposited in the University Library, being made available for loan and photocopying, subject to provisions of the Copyright Act 1968.

I also give permission for the digital version of my thesis to be made available on the web, via the University's digital research repository, the Library catalogue and also through web search, unless permission has been granted by the University to restrict access for a period of time.

I acknowledge the support I have received for my research through the provision of an Australian Government Research Training Program Scholarship.

Stephen Tronchin

Acknowledgements

I would like to give my most sincere thanks to my supervisor, Anthony Thomas, for his guidance and support throughout the research and the writing of this thesis. Thank you to my co-supervisor, James Zanotti, for his assistance and useful feedback throughout this project.

I would also like to thank Hrayr Matevosyan for his help in using the QCDNUM evolution program, as well as providing his interface for the program.

With the deepest of gratitude, thank you to my parents Angela and Enzo, and my brother James, for their endless love and support in all aspects of life.

Chapter 1

Introduction

The discovery by the European Muon Collaboration (EMC) that the nucleon structure functions differ substantially in-medium compared to the free case surprised the nuclear physics community. The ratio of the in-medium to free structure function of the nucleon was found to drop below unity, indicating a suppression of the bound nucleon's structure function, this became known as the EMC effect. With many unsuccessful attempts to explain the EMC effect through conventional nuclear effects, such as Fermi motion and nuclear binding, it became clear that a change in the quark structure of the bound nucleon could provide an explanation for this effect.

In this research we will investigate both the unpolarized and polarized EMC effect, where we will build our nucleon from the quark level. We will employ the MIT bag to model the free nucleon. With this we will produce the unpolarized and polarized structure functions of the free nucleon. For the in-medium case we will apply the mean field approximation along with the QMC model, thus including the quark degrees of the freedom, such that the quark structure of the bound nucleon is allowed to be altered. To calculate the structure functions of the bound nucleon, we will consider the in-medium modifications to the bound nucleon and how these will impact its structure. Our calculations for the bound nucleon will take into account the mean scalar field generated by the σ meson exchanges, which is first included through the altered quark wave function of the bound nucleon, and then through the effective nucleon and diquark state masses. We will then consider the Fermi motion of the bound nucleon, which is included through a convolution with a Fermi smearing function. Finally, we will take into account the mean vector field generated by the ω meson exchanges, which gives rise to a vector potential and is included through scaling the quark distributions and shifting the Bjorken variable. With this we will produce the in-medium unpolarized and polarized structure functions of the nucleon.

With our in-medium and free structure functions we will then be able to produce a theoretical result for both the unpolarized and polarized EMC effect. We will call the ratio of the in-medium to free structure function of the nucleon the *EMC ratio*. We

will try various parameter choices to see how each parameter effects the result of both the unpolarized and polarized EMC ratio. We will also see what choices best fit the experimental data for the unpolarized EMC effect. As there is no experimental data for the polarized EMC effect, we will use the best fit parameter set from the unpolarized case to present the unpolarized and polarized EMC ratios together. We will then be able to compare our prediction of the polarized EMC effect from the bag model with those from the NJL model [1], and see whether the enhanced polarized EMC effect found in the NJL is a model dependent phenomena, or consistent with other model predictions.

We will then go through the contribution to both the unpolarized and polarized EMC ratio for each in-medium effect accounted for, where the in-medium modifications will be included one at a time to see how the EMC ratio develops with each added effect, and to find out what in-medium modifications play the dominant role in producing the EMC effect.

Finally, we will consider one correction to our calculations, namely the deuteron structure function. Our free structure function will be that of a free proton, whereas in reality the EMC ratio is performed with the deuteron structure function. Therefore, we will consider how including the deuteron structure function correction into our calculations changes our prediction of the unpolarized EMC effect.

Does the internal structure of a nucleon change when it is immersed in a nuclear medium? If so, what causes this change? Is this change different when looking at the polarized quark distribution compared to the unpolarized case? These are the questions we will explore.

Chapter 2

Background

Before delving into the exciting results from the EMC, a review of the structure of the nucleon as well as a description of deep inelastic scattering and structure functions will prove to be very useful.

2.1 Nucleon Structure

During the 1950's there were an ever growing number of particles called hadrons being discovered. Hadrons, such as the kaon, pion, neutron, and proton, along with a collection of other hadrons, were believed to be equally fundamental. As more and more hadrons were discovered it was becoming questionable as to whether they could all be fundamental particles. Around 50 years ago, during the 1960's, physicists were beginning to realize that the protons and neutrons that make up the atomic nucleus are not elementary particles, but contain their own sub-structure. On the theoretical front, in 1961, Murray Gell-Mann and Yuval Ne'eman introduced a system to give order to the ever growing number of hadrons being discovered. The system was known as SU3 symmetry [2] [3].

In 1964, seeking deeper understanding of the SU3 classification scheme, Murray Gell-Mann [4] and George Zweig [5] independently proposed the existence of the particle known as the quark. Gell-Mann was at the California Institute of Technology, while Zweig was at CERN. They proposed that the properties of hadrons, previously thought to be indivisible fundamental particles, could best be described if they were composed of smaller sub-atomic particles, termed *quarks* by Gell-Mann.

In the SU3 scheme there are three fundamental quarks; up (u), down (d), and strange (s), where each has its own anti-particle that has the opposite charge. The quarks are spin-$\frac{1}{2}$ fermions. Hadrons could then be split into two groups; mesons, which are composed of a quark and an anti-quark, and baryons, which are composed of three quarks. For example, the neutral kaon is a meson composed of a down quark and a strange anti-quark ($d\bar{s}$), and the proton is a baryon composed of two up quarks and a down quark (uud).

The SU3 classification scheme then gave a system to the collection of hadrons, known as the Eightfold Way, since many hadrons could be collected into octets. Particles with spin-0, such as the pions and kaons, form a group of eight mesons called a meson octet. Particles with spin-1 also form another meson octet. Particles with spin-$\frac{1}{2}$, such as the proton and neutron, form a baryon octet. Particles with spin-$\frac{3}{2}$ form a group of ten baryons, known as a baryon decuplet. Effectively, Gell-Mann and Ne'eman came up with a periodic table of hadrons, and the system could even be used to predict particles that were later discovered with the correct properties. An example of such a case is the omega$^-$ (Ω^-) particle, which is a part of the spin-$\frac{3}{2}$ baryon decuplet. Gell-Mann predicted in 1962 that this particle would be composed of three strange quarks (sss), have an electric charge of -1, and a mass around 1680 MeV. In 1964, a particle with very similar attributes was discovered [6], supporting SU3 symmetry as the correct representation for reality.

Quarks carry fractional electric charge in units of proton (or electron) charge, and by assigning a charge equal to $\frac{2}{3}e$ for the up quark and -$\frac{1}{3}e$ for the down and strange quarks, the charges of the known mesons and baryons came out correctly. However, the idea of fractional charges was not popular at the time. After several years of searching, it was agreed by most particle physicists that while quarks might be a useful mathematical construct, they had no reality as physical objects [7]. Theories that attempted to describe the growing variety of hadrons as combinations of a small set of fundamental particles, such as quarks, were a small minority.

It wasn't until the MIT-SLAC experiments through the late 1960's to early 1970's where evidence was found that would give the physical existence of quarks growing support. Deep inelastic scattering (DIS) has played a vital role in discovering and investigating the sub-atomic structure of the nucleon. DIS is the process where a high energy incident lepton interacts with a nucleon target such that insight into the structure of the target can be obtained, this is discussed in more detail in section 2.2. DIS provides us with structure functions, which contain information about the momentum distributions of the quarks inside the nucleon.

During April of 1968, Bjorken and Kendall took the data from the initial MIT-SLAC scattering experiments and looked at how the structure functions varied with the momentum transfer Q^2, the momentum transferred from the incident lepton to the target. They found that the structure functions scaled to a good approximation, meaning that the structure functions depend only on a variable x (later interpreted as the fraction of proton momentum carried by the struck quark) and are independent of Q^2. Although scaling had been predicted by Bjorken [8], it was Feynman's idea in 1969 that gave the clearest physical explanation of what scaling really means [9]. He introduced the Parton Model of the nucleon. The key feature of the model is that the proton is composed of point-like constituents he called *partons*. In such a model, scaling arises naturally because the high energy leptons rebound from the charged partons, which absorb the virtual boson. Extensive DIS experiments over the following decade confirmed that the

partons in Feynman's model were the quarks and gluons predicted by Gell-Mann and Zweig. Further experimental and theoretical efforts found that the nucleon consisted of three valence quarks.

Continued experiments found that the structure functions actually have a slight dependence on Q^2, which indicated a scaling violation. This was confirmed by SLAC in 1973 through deep inelastic electron scattering. With more experiments it became clear that the structure functions are not completely independent of Q^2, confirming the scaling violation. This discovery played a major role in developing an understanding of the nucleon. This slight Q^2 dependence of the nucleon structure functions had been anticipated in parton models that had included gluons [10]. By including a cloud of gluons around the charged quarks, it gave them a structure that naturally led to small scaling violations, as had been observed. In this model, the quarks interact via the exchange of spin-1 gluons at short distances. Analogous to photon exchange in QED, where radiative corrections must be made for charged particle scattering, here we must make radiative corrections for the gluons being emitted from the quarks. In the process of lepton scattering off a quark, one must take into account the scattering process in which a gluon is also radiated. Due to these radiative corrections the cross section for scattering off a particular parton develops a logarithmic dependence on Q^2, this dependence is exactly the observed scaling violation. The picture of the nucleon was starting to evolve, where the nucleon was considered to be made of three valence quarks surrounded by a gluon cloud.

One outstanding issue was that if the nucleon consisted of quarks, then why had they never before been detected despite continued efforts to find them. Light was shed on this question during the early 1970's with the development of the theory of the strong interactions, named Quantum Chromodynamics (QCD). QCD is the theory of the strong interaction which describes how quarks interact through the exchange of gluons. In QCD both the quarks and gluons carry colour charge, which is analogous to electric charge in electrodynamics, and the gluons interact with the quarks through this colour charge. QCD exhibits two main properties; colour confinement, and asymptotic freedom.

Colour confinement is the phenomenon that colour-charged particles such as quarks and gluons cannot be isolated, and can only exist in a composite particle so that a colour neutral particle is made. Although this has never been analytically proven, it is well established from calculations in lattice QCD as well as many years of experiments [11]. The property of confinement introduced by QCD provided an explanation as to why no isolated quarks could be observed.

Asymptotic freedom, discovered in 1973 [12] [13], is a reduction in the strength between quarks and gluons as the length scale between them decreases, this is opposite to electric charge which increases as charged particles move closer together. Gluons are self interacting, which makes QCD a complex theory to work with, and this provides the mechanism for confinement. As two quarks move away from each other the gluon field between them becomes increasingly energetic, so that eventually it will become energetically favourable for the gluon field to break into a quark-anti-quark pair. Hence

the initial quarks moving away from each other now form a quark pair and so no isolated quark is observed.

The development of QCD along with continued theoretical and experimental efforts, has led to a picture of the nucleon being formed in which it consists of the three valence quarks, a fluctuating sea of quark-anti-quark pairs, and neutral gluons carrying the strong force acting as the exchange particle between quarks. To date there are 6 quarks; up, down, strange, charm, top, and bottom, with a corresponding anti-quark for each that has opposite charge. The proton is made from two up and one down (uud) valence quarks, and the neutron is made from one up and two down (udd) valence quarks.

This internal structure of the nucleon was believed to be the same for a bound nucleon compared to a free nucleon. Our interest is investigating what happens to the quark structure of the nucleon when it is immersed in a nuclear medium.

2.2 Deep Inelastic Scattering and Structure Functions

In this section we will provide an overview of Deep Inelastic Scattering (DIS) and the kinematics of the process. We will then discuss both the unpolarized and polarized structure functions of the nucleon.

2.2.1 Kinematics of Lepton DIS

Deep inelastic scattering is the process where high energy leptons are scattered off a nucleon target, such as a proton. The leptons are accelerated to high speeds through a particle accelerator. The high energy of the incident projectile allows it to resolve the internal structure of the nucleon target. During *elastic* scattering, a lepton is incident on a nucleon at low energies and as a result the nucleon stays intact, which leads to form factors. However, at higher energies the incident lepton is able to probe the internal structure by exciting the nucleon, this being referred to as deep *inelastic* scattering. The term inelastic means that the target absorbs some momentum, and hence there is a momentum transfer from the incident lepton to the nucleon, with the final state being more than just a nucleon. At high energies this momentum transfer is sufficient to cause the nucleon to shatter. By inspecting the scattered lepton and the interaction products one can gain insight into the nature of the process. Deep inelastic scattering allows us to see how the momentum of the nucleon is distributed among its constituents.

In Fig. 2.1 we depict a lepton scattering off a hadronic target via the exchange of a virtual boson, where the final hadronic state X is undefined. It is very useful to define some quantities associated with deep inelastic scattering:

- The target has 4-momentum P^μ, in the lab frame the target is at rest and hence

$$P^\mu = \left(M, \vec{0}\right). \tag{2.1}$$

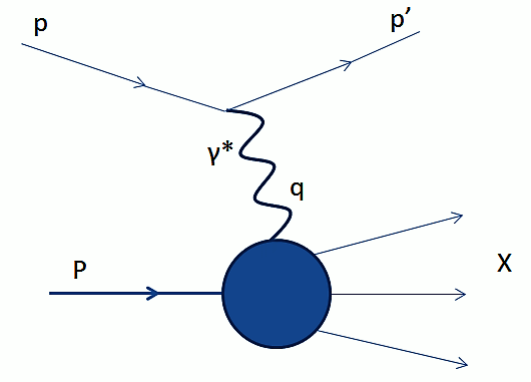

Figure 2.1: Deep inelastic scattering of a lepton off a nucleon via the exchange of a virtual boson.

- The incident lepton has 4-momentum p^μ with incident energy ϵ,

$$p^\mu = (\epsilon, \vec{p}\,). \tag{2.2}$$

- The scattered lepton has 4-momentum p'^μ with energy ϵ',

$$p'^\mu = \left(\epsilon', \vec{p}\,'\right). \tag{2.3}$$

- The virtual boson transferred from the lepton to the target has 4-momentum q^μ with energy ν,

$$q^\mu = (\nu, \vec{q}\,), \tag{2.4}$$

  where the energy transferred from the incident lepton to the target via the virtual boson is

$$\nu = \frac{P \cdot q}{M} = \epsilon - \epsilon'. \tag{2.5}$$

- The lepton scattering angle in the lab frame is θ.
- The solid angle into which the lepton is scattered is $d\Omega$.
- The squared 4-momentum transfer is (neglecting small lepton mass)

$$Q^2 = -q^2 = -(p - p')^2 = 4\epsilon\epsilon' sin^2\left(\frac{\theta}{2}\right). \tag{2.6}$$

- The Bjorken variable x is the fractional momentum of the nucleon that a quark must carry in order to absorb the virtual boson, this is given by

$$x = \frac{Q^2}{2P \cdot q} = \frac{Q^2}{2M\nu}. \tag{2.7}$$

The value of Q^2 gives the resolving power of the incoming lepton. The spatial wavelength a lepton can resolve is related to the Q^2 value by $\lambda \simeq \frac{1}{\sqrt{Q^2}}$. So if one looks at a nucleon with a low Q^2, hence a large wavelength and poor spatial resolution, one cannot resolve much of the internal structure of the nucleon. For Q^2 of around 1 GeV^2 the probed distances are comparable to the size of the proton. As the value of Q^2 increases the resolving power of the probe increases and the internal structure of the nucleon is able to be resolved. Up to values of 1 GeV^2 the process would be dominated by scattering off the valence quarks. For larger values of Q^2 the resolving power of the incident lepton is able to see more of the quark-anti-quark pairs and gluons that make up the nucleon. To a good approximation, one is able resolve objects of order $\frac{1}{10}$ fm at $Q^2 = 4$ GeV^2 and order $\frac{1}{100}$ fm at $Q^2 = 100$ GeV^2.

2.2.2 Unpolarized Structure Functions

Deep inelastic scattering provides us with structure functions, which contain information about the momentum distributions of the quarks inside the nucleon. We will denote $q_f(x)$ as the number density of quarks with flavour f carrying a fraction x of the nucleon's momentum. The distributions $q_f(x)$ are known as *parton distribution functions* and from these we can get the structure functions. The structure functions are Lorentz invariant and so one can formulate the parton model in any frame. Conceptually the simplest frame is the one in which the nucleon has momentum approaching infinity along the z-direction. This is referred to as the *infinite momentum frame* [14]. In this frame, time dilation implies there is no time for interaction between the quarks during the absorption of the virtual boson and hence we can treat the process in the impulse approximation. Since the quarks are all non-interacting and point-like, the cross section for interaction is just the sum of the cross sections for scattering from each individual quark. Thus the structure functions, F_1 and F_2, are proportional to $\sum_f e_f^2 q_f(x)$, where e_f is the charge of the quark of flavour f in units of the proton charge. The unpolarized structure function $F_1(x)$ is given by [14]

$$F_1(x) = \frac{1}{2} \sum_f e_f^2 q_f(x). \tag{2.8}$$

The Callan-Gross relation [15] shows that F_2 is related to F_1 by

$$F_2(x) = 2xF_1(x) = x \sum_f e_f^2 q_f(x), \tag{2.9}$$

where Eq. (2.8) and (2.9) are only true at leading order in α_s.

When considering the spin-independent case we include all spin orientations of the quarks inside the nucleon. We will introduce the concept of helicity, which describes a particles spin direction related to its momentum direction. If a particle has positive

helicity (+1) then the direction of motion is parallel to its spin direction, if a particle has negative helicity (−1) then the direction of motion is anti-parallel to its spin direction. Mathematically, helicity is the projection of the spin vector onto the momentum vector,

$$h \equiv \vec{\sigma} \cdot \frac{\vec{p}}{|\vec{p}|} = \pm 1. \tag{2.10}$$

If we consider a proton with positive helicity in an infinite momentum frame. We then define $q_f^{\uparrow}$ and $q_f^{\downarrow}$ to be the number density of quarks of flavour i with helicity parallel and anti-parallel to the target proton, respectively. The unpolarized case has distributions related by $q = q^{\uparrow} + q^{\downarrow}$.

We can now expand out the sum in Eq. (2.9) into the quark flavours u, d and s, hence the spin-independent structure function for the proton is

$$F_{2p}(x, Q^2) = x \left[\frac{4}{9} u(x, Q^2) + \frac{1}{9} d(x, Q^2) + \frac{1}{9} s(x, Q^2) \right], \tag{2.11}$$

where

$$\begin{aligned} u(x, Q^2) &= u^{\uparrow}(x, Q^2) + u^{\downarrow}(x, Q^2) + \bar{u}^{\uparrow}(x, Q^2) + \bar{u}^{\downarrow}(x, Q^2), \\ d(x, Q^2) &= d^{\uparrow}(x, Q^2) + d^{\downarrow}(x, Q^2) + \bar{d}^{\uparrow}(x, Q^2) + \bar{d}^{\downarrow}(x, Q^2), \\ s(x, Q^2) &= s^{\uparrow}(x, Q^2) + s^{\downarrow}(x, Q^2) + \bar{s}^{\uparrow}(x, Q^2) + \bar{s}^{\downarrow}(x, Q^2). \end{aligned} \tag{2.12}$$

Assuming charge symmetry [16], we have:

$$d^n = u^p \equiv u \qquad u^n = d^p \equiv d, \tag{2.13}$$

so the spin-independent structure function for the neutron is

$$F_{2n}(x, Q^2) = x \left[\frac{4}{9} d(x, Q^2) + \frac{1}{9} u(x, Q^2) + \frac{1}{9} s(x, Q^2) \right]. \tag{2.14}$$

In the parton distributions we note the inclusion of both the quark and anti-quark distributions. We will not be explicitly calculating the anti-quark distributions, but these will be included through an approximation. The strange quark distribution is also not explicitly calculated, but is included due to manifestation of the strange quark distribution in the QCD evolution process, discussed in Section 3.3. In these expressions we include the dependence on Q^2.

2.2.3 Polarized Structure Functions

Spin dependent measurements are able to reveal more information about the internal structure of the nucleon. Many new and exciting developments have been made by investigating spin physics. When considering the spin-dependent case we only consider quarks that have a specific spin orientation, namely quarks which have helicity parallel to that of the target nucleon. The polarized case has distributions related by $\Delta q = q^{\uparrow} - q^{\downarrow}$.

The spin dependent structure function is given by [14]

$$g_1(x) = \frac{1}{2}\sum_f e_f^2 \Delta q_f. \tag{2.15}$$

Expanding out the sum, for the proton we have

$$g_{1p}(x,Q^2) = \frac{4}{18}\Delta u(x,Q^2) + \frac{1}{18}\Delta d(x,Q^2) + \frac{1}{18}\Delta s(x,Q^2), \tag{2.16}$$

where

$$\begin{aligned}
\Delta u(x,Q^2) &= u^{\uparrow}(x,Q^2) - u^{\downarrow}(x,Q^2) + \bar{u}^{\uparrow}(x,Q^2) - \bar{u}^{\downarrow}(x,Q^2),\\
\Delta d(x,Q^2) &= d^{\uparrow}(x,Q^2) - d^{\downarrow}(x,Q^2) + \bar{d}^{\uparrow}(x,Q^2) - \bar{d}^{\downarrow}(x,Q^2),\\
\Delta s(x,Q^2) &= s^{\uparrow}(x,Q^2) - s^{\downarrow}(x,Q^2) + \bar{s}^{\uparrow}(x,Q^2) - \bar{s}^{\downarrow}(x,Q^2).
\end{aligned} \tag{2.17}$$

Assuming charge symmetry, as we did for the unpolarized case, we find the spin-dependent structure function for the neutron is

$$g_{1n}(x,Q^2) = \frac{4}{18}\Delta d(x,Q^2) + \frac{1}{18}\Delta u(x,Q^2) + \frac{1}{18}\Delta s(x,Q^2). \tag{2.18}$$

2.3 QCD Evolution

When we determine the structure functions of the nucleon using the bag model, the calculated distributions will be at the model scale ($Q^2 = \mu^2$). In order to compare our model distributions with data they are required to be evolved from the model scale to a scale where they can be compared with experimental data, such as $Q^2 = 10$ GeV^2. To evolve the data the QCD evolution equations are used, also known as the DGLAP equations so named after the authors who first wrote them [17] [18] [19]. The QCD evolution equations determine the rate of change of parton densities when the energy scale at which they are defined is varied. They are essential in order to evolve parton densities from one scale Q^2 to a different one.

2.3.1 Non-Singlet Evolution Equations

The DGLAP evolution equations are simple for the valence quarks, which are good examples of a non-singlet quark distributions. Generally speaking, a flavour non-singlet quark distribution is one which cannot mix with gluons. For the case of the valence distributions, there are always three valence quarks. In this case, the non-singlet DGLAP evolution equations can be expressed as [14]

$$\frac{\partial q_v(x,\mu^2)}{\partial \ln \mu^2} = \frac{\alpha_s(\mu^2)}{2\pi}\int_x^1 \frac{dz}{z} P_{qq}\left(\frac{x}{z},\mu^2\right) q_v(z,\mu^2). \tag{2.19}$$

Here q_v is either the valence u or d distribution, and $P_{qq}\left(\frac{x}{z},\mu^2\right)$ is the $q-q$ splitting function which can be interpreted as the probability for a quark carrying momentum fraction z of the nucleon (in the infinite momentum frame) to radiate a gluon, leaving the quark with momentum fraction x. The momentum carried by the radiated gluon is positive, and so only quarks with $z > x$ can contribute. The QCD coupling constant, $\alpha_s(\mu^2)$, is scale-dependent and to leading order is given as

$$\alpha_s(\mu^2) = \frac{4\pi}{\beta_0 \ln \frac{\mu^2}{\Lambda^2_{\rm QCD}}} \tag{2.20}$$

with

$$\beta_0 = 11 - \frac{2}{3}N_f, \tag{2.21}$$

where $\Lambda_{\rm QCD}$ is a constant determined from experiment, with a value of $\Lambda_{\rm QCD} \approx 200-300$ MeV [14], and N_f are the number of quark flavours allowed at this energy scale.

2.3.2 Singlet Evolution Equations

Unlike the non-singlet case, the singlet quark densities obey evolution equations coupled to the gluon density. The simplest case for the singlet DGLAP equations correspond to a single type of quark with distribution $f_i(x,\mu^2)$. Before writing the evolution equations for such a distribution, we need to generalize the parton densities to include gluons, thus we have $g(x,\mu^2)dx$ is the number of gluons in the momentum interval $[xP,(x+dx)P]$ in a nucleon with momentum $P(P\to\inf)$, when evaluated at the scale μ^2. The singlet DGLAP evolution equations can be expressed as

$$\frac{\partial}{\partial \ln\mu^2} f_i(x,\mu^2) = \frac{\alpha_s(\mu^2)}{2\pi}\int_x^1 \frac{dz}{z}\left(P_{qq}\left(\frac{x}{z},\mu^2\right) f_i(z,\mu^2) + P_{qg}\left(\frac{x}{z},\mu^2\right) g(z,\mu^2)\right), \tag{2.22}$$

$$\frac{\partial}{\partial \ln\mu^2} g(x,\mu^2) = \frac{\alpha_s(\mu^2)}{2\pi}\int_x^1 \frac{dz}{z}\left(P_{gq}\left(\frac{x}{z},\mu^2\right) f_i(z,\mu^2) + P_{gg}\left(\frac{x}{z},\mu^2\right) g(z,\mu^2)\right), \tag{2.23}$$

where the details on the splitting functions can be found in Ref. [14].

Since the DGLAP evolution equations are first-order integro-differential equations, once we know the parton distribution at some scale μ^2, they can be calculated at any other scale where leading order, perturbative QCD applies. Hence, we can evaluate our quark distributions at some model scale, and then evolve them to any other scale for comparison to experimental data. We will perform our QCD evolution using the QCDNUM program [20]. QCDNUM, conveniently, handles the different evolution of the singlet and non-singlet quark distributions. The evolution process will generate quark and anti-quark distributions for the u d and s quarks, as well as a gluon distribution. Even if these distributions are not explicitly calculated to begin with, the evolution process will dynamically generate them at the evolved scale. For more information on the process of QCD evolution, the QCDNUM write up is very useful and can be found in Ref. [20].

2.4 The EMC Effect

We will now give a review of the EMC effect, the understanding of which is crucial to this work. Our understanding of nuclear structure was thrown under spotlight with the unexpected experimental results released by the European Muon Collaboration (EMC) in 1983, who conducted high energy scattering experiments at CERN. The EMC compared the structure function of a free nucleon to the structure function of a bound nucleon [21] and found there was a difference between them. Extensive deep inelastic muon scattering was performed on liquid hydrogen, deuterium, and iron. The measurements with hydrogen and deuterium targets allowed the structure functions for the free nucleon to be determined, and measurements with iron allowed the in-medium structure functions to be determined.

The proton structure function F_2^p is able to be extracted from the hydrogen data alone. The neutron structure function F_2^n is able to be determined using both the hydrogen and deuterium data, where one can subtract the hydrogen data from the deuterium data to obtain the neutron structure function. However, in this procedure of obtaining the neutron structure function, corrections must be made to take into account the effects arising from the nucleon motion in the deuteron nucleus, which is a loosely bound proton-neutron system. After making corrections for this Fermi motion one can determine the neutron structure function.

Prior to this experiment, there were theoretical predictions made of the structure function of a bound nucleon. Such a prediction can be made in a high mass number (A) element, provided the corrections due to the nuclear effects are known. To determine such corrections, it was common to view the nucleus as a collection of weakly bound slowly moving nucleons, each of which had an internal structure that did not change compared to the free nucleon case. The experimental results released by the EMC had a complete disagreement with the theoretical predictions.

In Fig. 2.2a we show the theoretical prediction of the in-medium to free structure function of the nucleon. The general trend shows an enhanced quark distribution for higher x. In Fig. 2.2b we show the experimental results, the in-medium structure function F_2^N is obtained from iron and the free case from deuterium. The general trend shows a decrease in the iron structure function for higher x, which is in complete disagreement with the theoretical expectation based on nucleons with unchanging internal properties.

From the EMC results we see that the structure function of the nucleon is suppressed at larger x values when in a nuclear medium. Therefore, for a bound nucleon, in the valence region, there appears to be a decrease in the number of partons carrying a given fractional momentum x of the nucleon compared to the free case. This suppression of the in-medium structure function for a bound nucleon is known as the EMC effect.

Since the release of the initial EMC results the experimental situation has continued to progress and further in-medium structure functions have been obtained by various groups at SLAC [22] [23] [24], by the New Muon Collaboration (NMC) at CERN [25], and by the BCDMS collaboration [26] [27]. Through this experimental effort the ratio

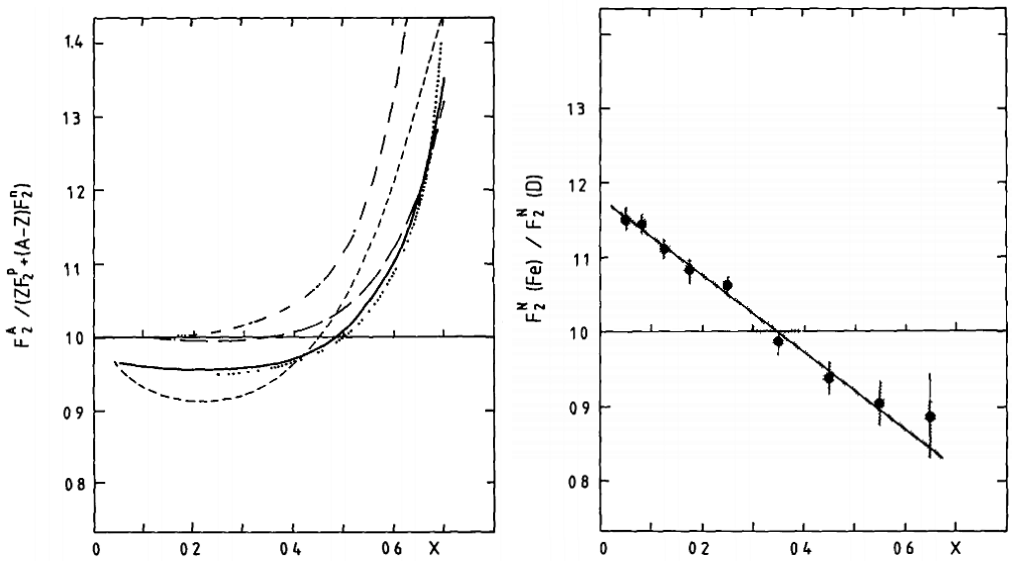

(a) Theoretical prediction. (b) Experimental results.

Figure 2.2: a) Theoretical prediction of the ratio of the in-medium to free structure function of the nucleon as a function of Bjorken variable x. b) Experimental determination of the ratio of the in-medium to free structure function of the nucleon as a function of x. There is a clear disagreement between theoretical and experimental results.

of the in-medium to free structure function of the nucleon has been determined to an improved accuracy. In Fig. 2.3 we show more recent data for the EMC effect from the EMC [28], who took the ratio of the nuclear structure function for copper and deuterium, and SLAC [29], who took the ratio of iron to deuterium. The experimental results show that in the valence region, corresponding to $0.3 \leq x \leq 0.7$, there is a decrease in the in-medium structure function. This means that when a nucleon is placed in a nuclear medium the quark momentum distribution becomes suppressed for increasing x in the valence region. The ratio is at unity around $x = 0.3$, and remains above one for decreasing x until about $x = 0.06$. The low-x region corresponding to $x \leq 0.15$ has also been investigated to a greater accuracy. In this region the ratio of the in-medium to free structure function decreases with decreasing x. This low-x region is dominated by effects related to a phenomena known as shadowing [30].

The results are clear on the experimental front; when immersed in a nuclear medium there is a suppression of the structure function of a bound nucleon compared to the free case. This is an exciting result, any unexpected experimental result is no doubt a spark that excites theorists to come up with a theory or model to explain such observations. The EMC effect is no exception. Many papers were published rapidly in response to the results, and about 35 years on, there is still no widely accepted explanation.

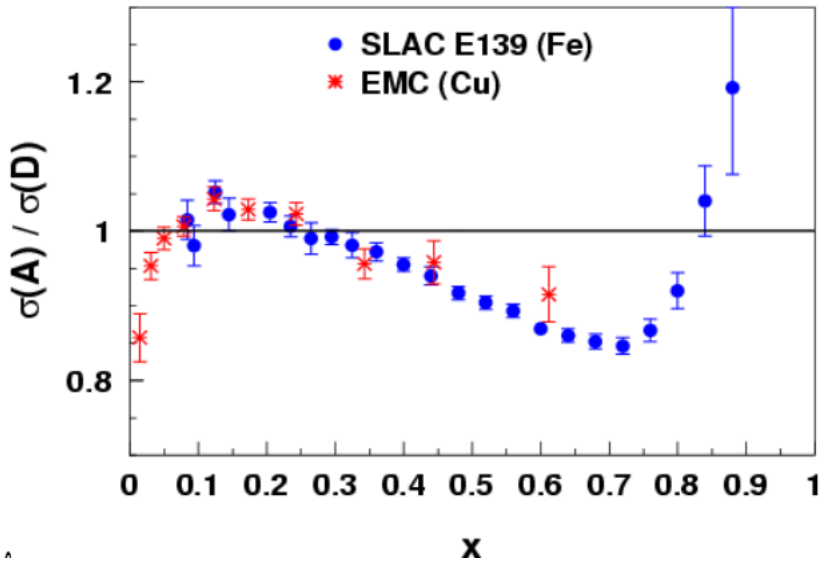

Figure 2.3: The EMC effect from the EMC [28] and SLAC [29].

It became clear that to understand the EMC effect, our view of nuclear structure had to change. Viewing the nucleon as an object with an unchanging internal structure was dubious at best, and the EMC effect gave rise to a new approach of viewing the nucleon; the Quark Meson Coupling (QMC) model, which explicitly includes the quark degrees of freedom thus allowing the internal structure of the nucleon to be altered. Before discussing the QMC model we will discuss the use of the mean field approximation, which is commonly employed when investigating the EMC effect, and we will discuss the attempts to explain the EMC effect through conventional nuclear effects such as Fermi motion and nuclear binding.

2.5 Mean Field Approximation

Bound nucleons experience many interactions with the surrounding nuclear environment. It would be a strenuous task to individually calculate the interaction of one nucleon with all other nucleons in the nucleus, we need to simplify the task and therefore we will take the approach of the mean field approximation.

In order to explain the EMC effect the mean field approximation is used in many theories. In general, a mean field theory is a self consistent field theory which considers a large number of small individual components that interact with each other. The idea is that the effect of all other individuals on a given individual can be approximated by a single averaged effect, this effectively reduces a many-body problem to a simpler one-body problem. This approximation can be adopted for the nucleons in a nucleus. The individual nucleons interact with one another via the exchange of mesons. At our

present understanding, bound nucleons interact with each other through the exchange of the π (pion), σ, ω, and ρ mesons.

The pion has total spin zero ($J = 0$), negative parity (P) ($J^P = 0^-$), and isospin 1 ($I = 1$) [31].The pion is the lightest meson, and the single pion exchange is responsible for the long range part of the nucleon-nucleon interaction. Since the pion has negative parity, the mean pion field must be set to zero to avoid parity breaking [32]. Its contribution can be included through the Fock exchange term, but the pion is not considered in this work.

The σ meson is a scalar meson with total spin zero ($J = 0$), even parity ($J^P = 0^+$), and isospin zero ($I = 0$) [31]. The σ meson is responsible for the intermediate range attractive force between nucleons. Starting with the well known one-boson-exchange potentials [33], it became clear that the intermediate range attractive force between the nucleons of a nucleus had a Lorentz scalar, isoscalar character, which at the time was represented by the exchange of the σ meson. This meson exchange was thought to be unphysical and purely a mathematical construct developed for convenience. The existence and properties of the σ meson have been controversial for almost six decades, however experimental investigation into the dispersion relations seen in pion-nucleon (πN) scattering performed in the past few decades have shown that the σ state does in fact exist [34] [35]. The Lorentz scalar, isoscalar character of the intermediate range attractive force between nucleons was also shown by the group in Paris [36], where a dispersion relation theory of the nucleon-nucleon (NN) force was developed.

The ω and ρ mesons are vector mesons with total spin 1 ($J = 1$), and odd parity ($J^P = 1^-$). The ω meson has isospin 0 ($I = 0$), while the ρ meson has isospin 1 ($I = 1$) [37]. The ω meson is responsible for the short range repulsion between nucleons. The ρ meson accounts for the isospin dependence of the interaction, and is necessary when there is a difference in the proton and neutron densities, so it is of particular importance in the case for $N \neq Z$ nuclei where isovector properties should be taken into account [38]. In this work we will only consider the case where ($N = Z$) and so we need not consider the effect of the ρ meson. A summary of the mesons is shown in table 2.1

Meson	Mass (MeV)	J^P	I	Interaction
π	135	0^-	1	Long range attraction
σ	400-700	0^+	0	Intermediate range attraction
ω	783	1^-	0	Short range repulsion
ρ	775	1^-	1	Isospin dependence ($N \neq Z$)

Table 2.1: Mesons in nucleon-nucleon interactions

For simplicity, we will only consider the effect of the σ and ω mesons on a bound

nucleon. Using the mean field approximation we can combine the effects of these mesons into a single averaged effect for each case. If we consider a single bound nucleon, it will be modelled as sitting in an averaged scalar field, which is formed by all the σ meson interactions, and also sitting in an averaged vector field, which is formed by all the ω meson interactions.

Models of bound nucleons based on a relativistic mean field theory appeared in the 1950's with a paper published by Johnson and Teller [39]. Further work was done by Walecka, who developed the Walecka model [40] in 1974. These models proved to be very successful in describing nuclear matter and provided strong evidence for the applicability of the mean field approximation to bound nucleons.

2.6 Fermi Motion and Nuclear Binding

It was thought that the observed EMC effect could be accounted for by conventional nuclear effects, namely Fermi motion and nuclear binding energy. Nucleons are not stationary within a nucleus, but rather they fluctuate and Fermi motion corresponds to the small motion of a bound nucleon within the nucleus. Fig. 2.4 provides some insight into this phenomena.

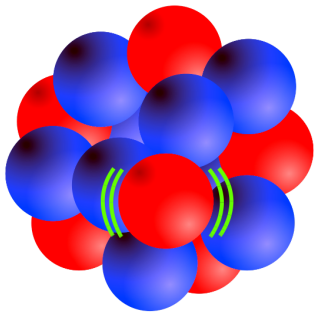

Figure 2.4: Fermi motion of a bound nucleon.

The Fermi motion and nuclear binding effects do not imply a change in internal nucleon structure, and so *if* they did happen to explain the EMC effect then the situation would be resolved without the need to consider a change to the internal structure of the bound nucleon. A study into this idea was performed by Bickerstaff and Thomas [41], who investigated the EMC effect with an emphasis on conventional nuclear corrections, including Fermi motion and nuclear binding. They found that these corrections cannot explain the observed EMC effect. Further investigations were performed by Birse [42], where the effects of nuclear binding energy and Fermi motion on deep-inelastic structure functions were studied in a relativistic mean field treatment. The conclusion was that the mean field contributions to nucleon binding can account for only a rather small fraction of the depletion of the nuclear structure function in the region $x \simeq 0.5$. It was also found that the Fermi motion was too small to give the observed depletion. It was becoming clear that conventional nuclear effects could not explain the EMC effect. This

provided evidence for the modification of the internal nucleon properties when in matter.

These results were confirmed in further studies by Miller and Smith [43], where the relationship between properties of nuclear matter and structure functions were measured in lepton-nucleus deep inelastic scattering using light front dynamics. They looked at relativistic mean field models such as the Walecka [40], Zimanyi-Moszkowski [44], and Rusnak-Furnstahl [45] models. In these models the mesons couple to the nucleons, where the nucleons are treated as immutable. The conclusion of the investigation was that relativistic mean field models of the nuclei, successful for many observables, do not contain the binding effect needed to reproduce the observed EMC effect. The depletion of the deep inelastic structure function observed in the valence region is due to some yet unknown interesting effect involving dynamics that go beyond the conventional nucleon-meson treatment of nuclear physics.

These results pointed to a very important change in our fundamental understanding of the nucleon. *When placed in a nuclear medium the internal structure of the nucleon undergoes a change, pointing to a new view of nuclear theory.*

2.7 The QMC Model

The EMC effect gave rise to a new model of the nucleon, the Quark Meson Coupling (QMC) model. With conventional nuclear effects being insufficient to explain the EMC effect, physicists turned to the internal structure of the nucleon and incorporated the quark degrees of freedom. We will provide a general overview of the QMC model.

To accurately investigate the internal structure of the nucleon, a relativistic treatment is necessary. Quarks are also quantum mechanical objects and so the QMC model is formulated as a Quantum Field Theory (QFT), where the system is described by a Lagrangian density, $\mathcal{L}$. An early attempt to describe the nucleon many-body problem using QFT was Quantum Hadrodynamics (QHD), where the nucleus is described as a relativistic system of baryons and mesons, introduced by Walecka [40] in 1974. QHD generates an effective NN interaction through the exchange of mesons between the nucleons, which were considered to have no internal structure. Walecka and co-workers used the Lorentz scalar nature of the intermediate NN attraction and the Lorentz vector character of the short range repulsion to construct a fully relativistic mean field theory of nuclear matter, which proved to be quite successful. Later the model was extended to finite nuclei [46]. In these models the nucleon was considered to be an immutable object, lacking any internal structure, experiencing a mean field generated by the mesons.

The ideas of Walecka were quite successful but there was one outstanding issue. At nuclear matter densities, where only nuclear forces are at play between protons and neutrons, the typical mean scalar field strength experienced by a bound nucleon in the Walecka model is of the order 500 MeV. This is a huge number, and as a result the effective mass of the bound nucleon is only half of its free mass [47]. At around the same

time that Walecka and collaborators were developing their model, the theory of Quantum Chromodynamics (QCD) was developed as a local gauge theory based on colour symmetry. Experimental results in the late 1960's continuing through to 1970's revealed that the nucleon contains point like constituents called quarks, with the gluon acting as the exchange particle of the strong force. The mesons exchanged between nucleons must couple to the quarks as this is the only component of the nucleon that the mesons can couple to. Thus, the question arose from the more fundamental level of the nucleon. When a nucleon is in medium, how can it be that the exchange of mesons between nucleons, where the mesons must couple to the quarks at such a strength indicated by the Walecka model, can have no effect on the internal structure of the nucleon, which is far from point-like.

Then, in 1983, the EMC results were released, which showed a suppression in the structure function of a bound nucleon compared to a free nucleon. Could it be possible to explain the EMC effect by allowing the quark structure of a bound nucleon to be altered, rather than considering it as an immutable object? Such questions led to a drastically different approach to nuclear binding. The Quark Meson Coupling (QMC) model, initially proposed by Guichon [48] in 1988, has the feature that the meson field couples to the quarks in the nucleon. This model goes far beyond QHD to explicitly include the internal structure of the nucleon through the quark degrees of freedom. The nucleon-nucleon interaction is then explained by meson exchanges between quarks rather than the nucleons as a whole.

In the QMC model, the nucleus is considered to be a collection of nucleons that do not overlap. We are using the MIT bag model to confine the quarks, and so each nucleon is treated as a bag containing three quarks. It is assumed the effect of having the bags overlap, that is clusters of more than three quarks, can be ignored. Of course, this approximation will break down at some density, but is certainly acceptable at nuclear matter densities. In this regard, the bag model is a good approximation to confinement, but should not be taken too literally. From lattice QCD calculations [49] we find that the quarks are more accurately bound to each other through a Y-shaped colour string. Around this thin string is the usual, non-perturbative QCD vacuum in which the quarks from other clusters can pass without disturbing the structure. Therefore, while the bag model imposes a strict boundary condition preventing the quarks from travelling through this boundary, we must view this as an average representation of a more complicated system of confinement, where no deep physical meaning should be given to the bag boundary [50].

In the QMC model the interactions between nucleons are generated by the exchange of mesons coupled locally to the quarks. Combing this with the mean field approximation, we see that a quark inside a bound nucleon is effectively sitting in a mean field generated by the meson exchanges from all other nucleons. Hence, the effect of the mean meson fields generated by other nucleons is treated self-consistently when solving for the

wave function of each confined quark.

The mesons in consideration are the σ and ω mesons. Taking the simplest form of the coupling of the σ and ω mesons to the quarks confined in the MIT bag model, we get two Lorentz components to the nuclear mean field from these mesons; a Lorentz scalar attraction (σ meson), and a Lorentz vector repulsion (ω meson). In nuclear matter the vector field simply shifts the definition of the energy of the system, while the scalar field modifies the Dirac wave function [47]. This difference in the effect of the two Lorentz components of the nuclear mean field is of crucial importance, while their effects essentially cancel when it comes to the total energy of the nucleon, for the quark motion (or wave function) the scalar field is not cancelled. Therefore, when viewing the nucleon from the quark level, we must take into account the effect of the nucleon interactions on the quark structure.

In order to anticipate the possible consequence on the structure of a bound nucleon due to a scalar field we can turn to atomic physics. We know that when an electric field is applied to an atom, its electron structure will rearrange itself in order to the oppose the applied field. In terms of describing the energy of the system, this change in the atoms internal structure can be described in terms of an electric polarizability, where the energy of the systems has a term quadratic in the applied electric field with the coefficient being one half of the electric polarizability. The exact same thing happens when a magnetic field is applied to an atom, where the coefficient of the term that is quadratic in the applied magnetic field involves the magnetic polarizability. Looking at the nucleon itself, we know that applied electric and magnetic fields alter its internal structure, which give rise to electric and magnetic polarizabilities.

In more advance electron scattering experiments, these fields even give rise to what is known as generalized polarizabilites [51] [14]. With this background knowledge of how nuclear systems react to applied fields, it is strange that it took so long for serious attention to be given to the response of the nucleon to an applied scalar field, and its scalar polarizability.

From past experience, one would naturally expect that a nucleon sitting in a scalar field would have an energy dependence that is non-linear with the mean scalar field. In the first investigation into nuclear matter from this point of view, using the MIT bag model to self-consistently describe the quark structure of the bound nucleon, Guichon found exactly this behaviour [48]:

$$M^*(\bar{\sigma}) = M - g_\sigma \bar{\sigma} + \frac{d}{2}\left(g_\sigma \bar{\sigma}\right)^2, \tag{2.24}$$

where $d = 0.22R$, with R the bag radius. The last term is an essential part of the QMC model. It represents the response of the nucleon to the applied scalar field, where d is called the *scalar polarizability*. It is completely analogous to the response of atoms and nucleons to applied electric and magnetic fields.

The idea of the QMC model has been developed and used by many groups to explain various phenomena. Key people have been Saito and Thomas who have applied the

QMC model to many phenomena in nuclear physics with high success.

A key result was the application of the QMC model in exploring the EMC effect. They applied the QMC model as well as the mean field approximation to bound nucleons and found that through this approach the EMC effect can be produced [52]. This was an important result, as it showed that a possible explanation of the EMC effect is that the quark structure of the bound nucleon is altered in a nuclear medium.

The QMC model has also been applied to study the properties of hypernuclei with promising results [53] [54], and also employed to investigate the in-medium nucleon electromagnetic form factors [55]. Both the electric and magnetic form factors were found to be reduced for a nucleon at nuclear density, which agreed with the experimental data.

Our last mention will be the extensive application of the QMC model to investigate the properties of finite nuclei, with many successful results [56] [57] [58] [59]. The QMC model has no doubt proven to be a viable approach in explaining nuclear phenomena.

2.8 The Polarized EMC Effect In The NJL Model

Up until now we have only been talking about the spin-independent structure functions in nuclear medium, and when we refer to the EMC effect we are referring to the unpolarized EMC effect. This is because the data concerning the EMC effect has only been measured on unpolarized targets. However, with the 12 GeV upgrade at Jefferson Lab, we hope that this will bring forth the first data on the polarized EMC effect, where polarized beams and targets will be used.

Predictions on what the polarized EMC data will look like have been made by Cloët, Bentz and Thomas [1]. In their calculations they employ the use of a modified Nambu-Jona-Lasinio (NJL) model. In Fig. 2.5 we show the predictions from Ref. [1] for the unpolarized and polarized EMC effect. The EMC effect is obtained from the ratio of the in-medium to free spin-independent structure function, F_{2N}^A/F_{2N}, which has been experimentally tested. The polarized EMC effect is obtained from the ratio of the in-medium to free spin-dependent structure function, g_{1p}^A/g_{1p}, which is yet to be experimentally tested.

It will be very interesting to follow up this result for the polarized EMC effect found in the NJL model. It is clear that in the NJL model the polarized EMC effect is significantly greater than the unpolarized EMC effect, with the polarized effect being of order twice that of the unpolarized effect. We want to follow up from this result and see if this is purely a model dependent result or if the polarized EMC effect is also enhanced in other model calculations.

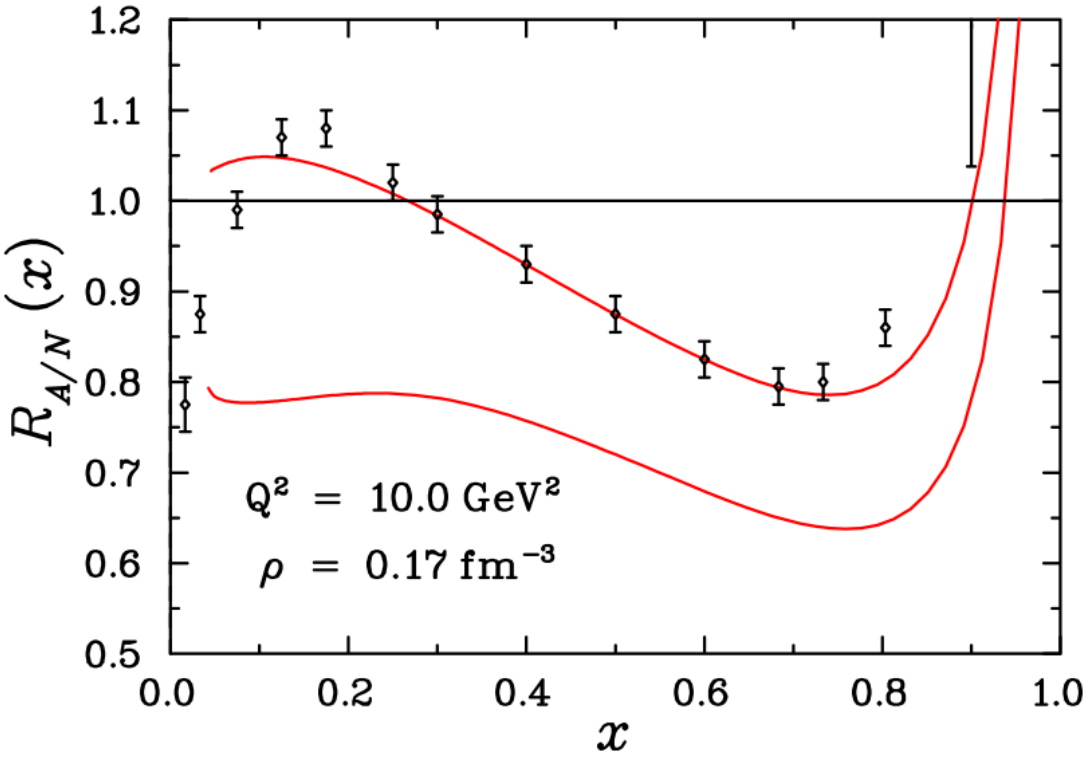

Figure 2.5: Ratios of the in-medium to free structure functions at nuclear matter density for the spin-independent and spin-dependent cases. The top curve is the EMC ratio F_{2N}^A/F_{2N}, where F_{2N} is the isoscalar structure function and the superscript A denotes the in-medium structure function. The EMC data for nuclear matter is taken from Ref. [60]. The prediction of the polarized EMC effect, g_{1p}^A/g_{1p}, obtained from Ref. [1] is the lower curve.

Chapter 3

Free Structure Functions

In order to produce the EMC effect we need to calculate the free and in-medium structure functions of the nucleon. In this chapter we will describe our process for calculating the free structure functions.

Often when modelling complex systems physicists use a method called perturbation theory. Perturbation theory is a technique where one starts be using an easier system with a known solution, then to model the real system one adds small disturbances, known as perturbations. Complex problems simplify greatly using such a technique. However, in QCD the small disturbances are so great that perturbation theory is strictly limited. The quarks in a nucleon are also confined and the force between them increases with distance. This odd behaviour, along with perturbation theory not being adequate, has made it very difficult to find a viable approach to model the nucleon.

Since our goal here is to investigate not just a free nucleon, but also the in-medium effects on a nucleon, we need a simple model that will give us a handle on including the in-medium modifications into the calculations of the nucleon.

The MIT bag model [61] is a successful phenomenological model for quark confinement. In this model, three non-interacting quarks are confined to a spherical region of space, with the boundary condition that the quark vector current normal to the surface vanishes. The quarks being treated as non-interacting is justified by appealing to the idea of asymptotic freedom, and the hard boundary condition is justified by quark confinement. In the MIT bag model all the calculations can be carried through analytically, giving us a viable approach for including the in-medium effects into the calculation of the quark distributions. We shall therefore choose the MIT bag to model the nucleon.

3.1 Overview of the Formalism

In calculating the free structure functions of the nucleon we will take the course of the operator product expansion (OPE). In the context of deep inelastic lepton-hadron scattering, the product of two electromagnetic or weak currents is expressed as a series expansion called the operator product expansion, which enables the extraction of a short

distance piece in the scattering cross sections. This piece is useful to us as it is calculable through the QCD Lagrangian by the use of the renormalization group method [62].

Through the OPE the moments of some arbitrary structure function $\mathcal{F}(x, Q^2)$ can be written as a sum of coefficient functions $\mathcal{C}_{i,n}(\mu^2, Q^2)$ multiplied by matrix elements $\mathcal{A}_{i,n}(\mu^2)$ [62]:

$$\int_0^1 x^{n-1}\mathcal{F}(x, Q^2)dx = \sum_i \mathcal{C}_{i,n}(\mu^2, Q^2)\mathcal{A}_{i,n}(\mu^2). \tag{3.1}$$

The coefficient functions $\mathcal{C}_{i,n}(\mu^2, Q^2)$ are perturbative corrections that describe how the structure functions evolve with Q^2 and can be calculated through the use of the renormalization group equations in perturbative QCD.

The matrix elements $\mathcal{A}_{i,n}(\mu^2)$ that produce the dominant contributions at large Q^2 are those of leading twist-2 and, in the $A^+ = 0$ gauge, have the form [63]

$$\mathcal{A}_{i,n}(\mu^2) \approx \langle\, (p,s)_{\mu^2} \,|\, \Psi^\dagger(0)\, \Gamma_i (i\partial^+)^{n-1}\, \Psi(0) \,|\, (p,s)_{\mu^2} \,\rangle, \tag{3.2}$$

where the subscript μ^2 indicates the renormalization scale at which the matrix element is evaluated, and Γ_i contains the Dirac and spin flavour matrices that are appropriate to the wave function under consideration. Twist is given by the difference of dimension and spin (twist=dimension-spin). The twist-2 contributions to the moments of a structure function correspond to scattering of a lepton off asymptotically free quarks, and calculating the twist-2 contributions will be our focus. Here we will not consider the twist-2 matrix elements which involve gluonic operators. The considered processes contributing to the twist-2 piece of the matrix elements $\mathcal{A}_{i,n}(\mu^2)$ is given in Fig. 3.1.

An important point is that the matrix elements $\mathcal{A}_{i,n}(\mu^2)$ are independent of Q^2 and depend only on the renormalization scale μ^2 [63]. This independence of momentum transfer is key as it makes the matrix element calculations possible in models which would be unable to make a direct calculation of $\mathcal{F}(x, Q^2)$.

The wave functions and operators that appear in Eq. (3.2) are renormalized ones and therefore involve the renormalization scale μ_R. Due to our limited ability to calculate Eq. (3.2) from QCD we will follow the procedure outlined in Ref. [63]. In this approach we assume that at the renormalization scale the renormalized wave functions, as well as the quark field operators, can be approximated by bag wave functions and bag field operators. Therefore, we will proceed by calculating the matrix elements in Eq. (3.2) within the bag model at the scale $\mu = \mu_R$. In a model calculation, μ is an undetermined input and will be obtained by comparison with data. The scale μ will be fitted by comparing the valence quark distribution against experimental data. All quark distributions and structure functions will then be calculated with this scale as the input.

The matrix elements $\mathcal{A}_{i,n}(\mu^2)$ can be expressed in terms of moments of quark and

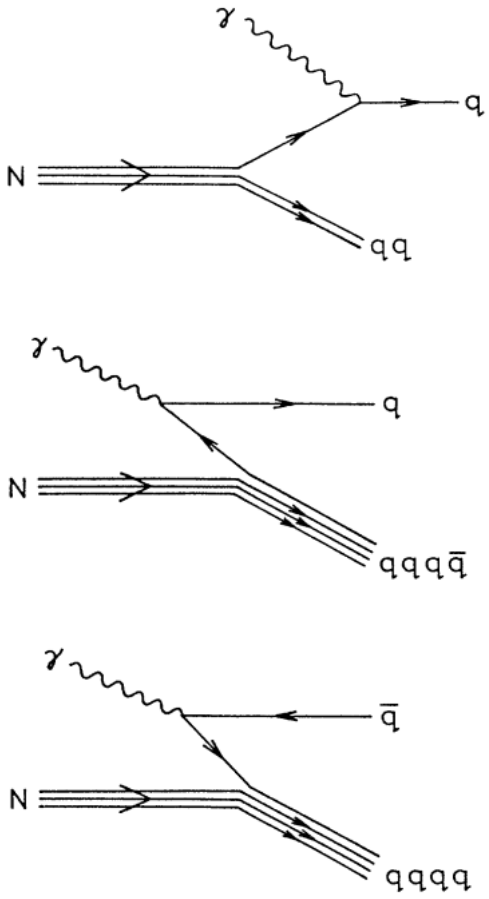

Figure 3.1: Contributions to the twist-2 piece of $\mathcal{A}_{i,n}(\mu^2)$ [63].

anti-quark distribution functions [64]

$$\begin{aligned} q_f^{\uparrow\downarrow}(x) &= p^+ \sum_n \delta(p^+(1-x) - p_n^+) |\langle n|\Psi_{+,f}(0)|p,s\rangle|^2, \\ \bar{q}_f^{\uparrow\downarrow}(x) &= p^+ \sum_n \delta(p^+(1-x) - p_n^+) |\langle n|\Psi_{+,f}^\dagger(0)|p,s\rangle|^2, \end{aligned} \tag{3.3}$$

where the notation $\uparrow\downarrow$ indicates the helicity projection, with $(1 \pm \gamma^5)/2$ for the quarks and $(1 \mp \gamma^5)/2$ for the anti-quarks, with $\uparrow$ indicating a quark with spin parallel to the spin of the target and $\downarrow$ indicating a quark with spin anti-parallel to the spin of the target. The sum runs over all intermediate states, f distinguishes the quark flavour, and the $+$ components of momenta k are defined by $k^+ = k^0 + k^z$.

For positive p^+ and p_n^+, the quark distributions are non-zero for $x \leq 1$. Although $q_f(x)$ and $\bar{q}_f(x)$ have support for negative x, there are other contributions in this region which are not included in Eq. (3.3) [65]. It is only in the region $0 \leq x \leq 1$ that $q_f(x)$ and $\bar{q}_f(x)$ give the full contribution, and so only in this region can we interpret the

structure functions in terms of parton distributions. Therefore, we will limit the explicit calculations of quark distributions to this region.

It can be shown that Eq. (3.3) satisfies the normalization condition

$$\int_0^1 dx \left[q_f^{\uparrow\downarrow}(x) - \bar{q}_f^{\uparrow\downarrow}(x)\right] = N_f^{\uparrow\downarrow} - \bar{N}_f^{\uparrow\downarrow}, \tag{3.4}$$

where $N_f^{\uparrow\downarrow}$ and $\bar{N}_f^{\uparrow\downarrow}$ count the number of quarks and anti-quarks in the target, respectively [63].

We will now look at how we can use Eq. (3.3) to obtain expressions for the processes shown in Fig. 3.1. The field operators Ψ and $\Psi^\dagger$, when expanded in a complete set of states, each yield two distinct contributions. Ψ may destroy a quark contained in the initial state leaving a two-quark intermediate state, or it may create an anti-quark resulting in a three-quark one-anti-quark intermediate state. In a similar way, $\Psi^\dagger$ may insert a quark into the initial state resulting in a four-quark intermediate state, or it could also destroy an anti-quark in the initial state (however, this will have no contribution as our choice of model wave function will only consist of three valence quarks).

The two-quark intermediate state will be our main focus and is calculated explicitly, whereas the four-quark intermediate states will be included in an approximate form to satisfy the normalization requirements of Eq. (3.4).

3.2 Calculating Quark Distributions in the Bag Model

3.2.1 The Two-Quark Intermediate State

We will now focus on the contribution from the two-quark intermediate state, which makes up the dominant part of the calculation for the valence quark distributions. The action of the operator Ψ on a three-quark state is defined by

$$\Psi(\mathbf{x})|\mathbf{x}_1\mathbf{x}_2\mathbf{x}_3\rangle = \delta(\mathbf{x}-\mathbf{x}_3)|\mathbf{x}_1\mathbf{x}_2\rangle + \text{permutations} \tag{3.5}$$

and similarly for a two-quark state. Inserting complete sets of states into Eq. (3.3) we obtain [63]

$$q_f^{\uparrow\downarrow} = \frac{M}{(2\pi)^3}\sum_{n,\alpha}\langle\mu|P_{f,\alpha}|\mu\rangle\delta(M(1-x)-p_n^+)\left|\int d\mathbf{x}_1 d\mathbf{x}_2\langle\mathbf{p}_n|\mathbf{x}_1\mathbf{x}_2\rangle\langle\mathbf{x}_1\mathbf{x}_2\mathbf{0}_\alpha^{\uparrow\downarrow}|\mathbf{0}\rangle\right|^2, \tag{3.6}$$

where $|\mu\rangle$ is the spin-flavour wave function of the initial state which is taken to be at rest and $P_{f,\alpha}$ is a projector operator onto quark flavour f and any other quantum number α. In this case, all initial quarks are taken to be in the lowest-energy state, and so α may be taken to be the quark spin projection m.

We will use the wave functions of the MIT bag model and modify these by a projection, namely the Peierls-Yoccoz projection [66]. This ensures the wave functions are

momentum eigenstates, and also ensures the translational invariance of the matrix elements used for the proof of Eq. (3.4).

Applying the Peierls-Yoccoz projection, we have in the coordinate representation for a three-quark state [63]

$$\langle \mathbf{x}_1\mathbf{x}_2\mathbf{x}_3|\mathbf{p}\rangle = \frac{1}{\phi_3(\mathbf{p})}\int d\mathbf{R}e^{i\mathbf{p}\cdot\mathbf{R}}\Psi(\mathbf{x}_1-\mathbf{R})\Psi(\mathbf{x}_2-\mathbf{R})\Psi(\mathbf{x}_3-\mathbf{R}), \tag{3.7}$$

where $\phi_3(\mathbf{p})$ is given by the normalization requirement

$$\langle \mathbf{p}|\mathbf{p}'\rangle = (2\pi)^3\delta(\mathbf{p}-\mathbf{p}'), \tag{3.8}$$

or more explicitly,

$$|\phi_3(\mathbf{p})|^2 = \int d\mathbf{x}e^{-i\mathbf{p}\cdot\mathbf{x}}\left(\int dy\Psi^\dagger(y-x)\Psi(y)\right)^3. \tag{3.9}$$

Similarly for the diquark state we have

$$\langle \mathbf{x}_1\mathbf{x}_2|\mathbf{p}\rangle = \frac{1}{\phi_2(\mathbf{p})}\int d\mathbf{R}e^{i\mathbf{p}\cdot\mathbf{R}}\Psi(\mathbf{x}_1-\mathbf{R})\Psi(\mathbf{x}_2-\mathbf{R}). \tag{3.10}$$

where $\phi_2(\mathbf{p})$ is given by the normalization requirement

$$|\phi_2(\mathbf{p})|^2 = \int d\mathbf{x}e^{-i\mathbf{p}\cdot\mathbf{x}}\left(\int dy\Psi^\dagger(y-x)\Psi(y)\right)^2. \tag{3.11}$$

Substituting Eq. (3.7) into Eq. (3.6) gives

$$q_f^{\uparrow\downarrow}(x) = \frac{M}{(2\pi)^3}\sum_m\langle\mu|P_{f,m}|\mu\rangle\int d\mathbf{p}_n\frac{|\phi_2(\mathbf{p}_n)|^2}{|\phi_3(\mathbf{0})|^2}\delta(M(1-x)-p_n^+)|\tilde{\Psi}^{\uparrow\downarrow}_{+,f}(\mathbf{p}_n)|^2, \tag{3.12}$$

where M is the nucleon mass and

$$\tilde{\Psi}^{\uparrow\downarrow}_{+,f}(\mathbf{p}_n) \equiv \int d\mathbf{x}e^{i\mathbf{p}_n\cdot\mathbf{x}}\Psi^{\uparrow\downarrow}_{+,f}(\mathbf{x}). \tag{3.13}$$

The best approach to do this integration is to choose the magnitude of $\mathbf{p}_n$ and its transverse component $p_n^\perp$ as the integration variables, as well as using the δ-function to do the $p_n^\perp$ integration. This produces the result

$$\int d\mathbf{p}_n\delta(M(1-x)-p_n^+) = 2\pi\int_{\frac{|M^2(1-x)^2-M_n^2|}{2M(1-x)}}^\infty p_n dp_n, \tag{3.14}$$

where M_n is the mass of the intermediate two-quark state.

In order to prove Eq. (3.14) we note that

$$p_n^+ = \sqrt{\mathbf{p}_n^2+M_n^2}+p_n^z, \tag{3.15}$$

and the δ-function appearing in the integral of Eq. (3.12) means that as we integrate over all of $\mathbf{p}_n$ we will pick out the value of

$$p_n^+ = M(1-x), \tag{3.16}$$

therefore by comparing Eq. (3.15) with Eq. (3.16), we see that

$$p_n^z = M(1-x) - \sqrt{\mathbf{p}_n^2 + M_n^2}. \tag{3.17}$$

Using the fact that $\mathbf{p}_n^2 = p_n^{z2} + p_n^{\perp 2}$, we have

$$p_n^{\perp 2} = 2M(1-x)\sqrt{M_n^2 + \mathbf{p}_n^2} - M^2(1-x)^2 - M_n^2. \tag{3.18}$$

We now apply the result of Eq. (3.14) to Eq. (3.12) and obtain the expression

$$q_f^{\uparrow\downarrow}(x) = \frac{M}{(2\pi)^2}\sum_m \langle\mu|P_{f,m}|\mu\rangle \int_{\frac{|M^2(1-x)^2 - M_n^2|}{2M(1-x)}}^{\infty} p_n dp_n \frac{|\phi_2(\mathbf{p}_n)|^2}{|\phi_3(\mathbf{0})|^2}|\tilde{\Psi}_m^{\uparrow\downarrow}(\mathbf{p}_n)|^2. \tag{3.19}$$

We will now make mention of the shortcomings of the Peierls-Yoccoz projection. Even though it creates a momentum eigenstate, there is still an unphysical dependence on the momentum in the internal wave function. Furthermore, the projection is a nonrelativistic approximation and is not equivalent to a boost. Since the initial state is at rest this is a reasonable assumption. When one might expect the nonrelativistic approximation for the intermediate state to be reasonable we can look at Eq. (3.19). The dominant part of the integral comes from the region of small p_n, therefore the nonrelativistic approximation should be valid while the lower limit of the p_n integration is less than the diquark mass M_n. This is true for x less than about 0.7 for $M_n \approx \frac{3}{4}M_n$ [63].

We are now at the stage to apply our choice of model, the MIT bag. Here we note that in the calculation of the free quark distributions the quark mass is set to zero. For a zero mass quark the MIT bag wave function takes the form [67]

$$\Psi_m(x) = N\begin{pmatrix} j_0\left(\frac{\Omega|x|}{R}\right)\chi_m \\ i\boldsymbol{\sigma}\cdot\hat{\boldsymbol{x}}j_1\left(\frac{\Omega|x|}{R}\right)\chi_m \end{pmatrix}\Theta(R-|x|), \tag{3.20}$$

Here R is the bag radius, Ω is the lowest energy eigenfrequency, j_0 and j_1 are the spherical Bessel functions of the first kind, χ_m are spinors, and $\boldsymbol{\sigma}$ are the Pauli spin matrices. The normalization is given by

$$N^2 = \frac{1}{4\pi}\frac{\Omega^3}{2R^3(\Omega-1)sin^2(\Omega)}. \tag{3.21}$$

In the MIT bag the quarks are confined to the interior of the bag, and so there is no component of the current normal to the surface of the bag. Therefore we have the

requirement that $\bar{\Psi}\Psi$ vanishes at the boundary of the bag, hence we have the boundary condition

$$\begin{aligned} &\bar{\Psi}\Psi|_{x=R} = 0, \\ &\Rightarrow j_0(\Omega) = j_1(\Omega). \end{aligned} \tag{3.22}$$

The lowest energy solution of Eq. (3.22) gives

$$\Omega \simeq 2.04. \tag{3.23}$$

In order to make use of Eq. (3.19) to calculate quark distributions we need to evaluate the normalizations $|\phi_2(\mathbf{p}_n)|^2$ and $|\phi_3(\mathbf{0})|^2$. These are tedious calculations and can be found in the Appendix for the intrigued reader. With the insight that a quark mass will be included for later calculations, it is convenient to keep the normalization term N in its full form in the evaluation of $|\phi_2(\mathbf{p}_n)|^2$ and $|\phi_3(\mathbf{0})|^2$ rather than inserting and simplifying it. This is because when a quark mass is inserted, the normalization term for the bag wave function with a quark mass is known and so can be simply changed in place of the free normalization.

Starting from Eq. (3.10), the full calculation is found in Appendix A, we obtain the result

$$|\phi_2(\mathbf{p}_n)|^2 = \frac{4\pi R}{u}\left(\frac{2\pi N^2 R^4}{\Omega^4}\right)^2 \int \frac{dv}{v} sin\left(\frac{2vu}{\Omega}\right) T^2(v), \tag{3.24}$$

and from Eq. (3.7), the full calculation found in Appendix B, we obtain the result

$$|\phi_3(\mathbf{0})|^2 = 4\pi\left(\frac{2\pi N^2 R^4}{\Omega^4}\right)^3 \int \frac{dv}{v} T^3(v). \tag{3.25}$$

The term resulting from the overlap integral of the bag wave function is given by

$$\begin{aligned} T(v) &= T_t(v) + T_b(v) \\ &= \left[(\Omega - v)sin(2v) + (1 - sin^2(\Omega)) - cos(\Omega)cos(\Omega - 2v)\right] \\ &\quad + \Bigg[\left(1 - \frac{4v^2}{2\Omega^2}\right) sin^2(\Omega) - \frac{2}{\Omega} sin(\Omega)cos(\Omega - 2v) + \frac{2}{\Omega} sin(\Omega)cos(\Omega) + \Omega sin(2v) \\ &\quad - sin(\Omega)sin(\Omega - 2v) - vsin(2v)\Bigg], \end{aligned} \tag{3.26}$$

where the first square bracket corresponds to the overlap integral of the top part of the bag wave function and the second square bracket to the bottom part. We have also made the substitutions

$$v = \frac{|\mathbf{x}|\Omega}{2R}\,, \quad u = |\mathbf{p}_n|R\,. \tag{3.27}$$

The evaluation of $|\tilde{\Psi}^{\uparrow\downarrow}_m(\mathbf{p}_n)|^2$ is taken from Ref. [63] where the Fourier transform of Ψ is given as

$$|\tilde{\Psi}^{\uparrow\downarrow}_m(\mathbf{p}_n)|^2 = \frac{1}{2}\left[f(\mathbf{p}_n) \pm (-1)^{m+3/2} g(\mathbf{p}_n)\right], \tag{3.28}$$

where we have

$$f(\mathbf{p}_n) = \frac{\pi R^3}{2} \frac{\Omega^3}{(\Omega^2 - sin^2(\Omega))} \left[s_1^2(u) + 2\frac{p_n^z}{|\mathbf{p}_n|} s_1(u)s_2(u) + s_2^2(u)\right], \tag{3.29}$$

and

$$g(\mathbf{p}_n) = \frac{\pi R^3}{2} \frac{\Omega^3}{(\Omega^2 - sin^2(\Omega))} \left\{s_1^2(u) + 2\frac{p_n^z}{|\mathbf{p}_n|} s_1(u)s_2(u) + \left[1 - 2\left(\frac{p_n^\perp}{|\mathbf{p}_n|}\right)^2\right] s_2^2(u)\right\}. \tag{3.30}$$

Here we have

$$s_1(u) = \frac{1}{u}\left[\frac{sin(u-\Omega)}{u-\Omega} - \frac{sin(u+\Omega)}{u+\Omega}\right], \tag{3.31}$$

which corresponds to the upper component of the bag wave function, and

$$s_2(u) = 2j_0(\Omega)j_1(u) - \frac{u}{\Omega} s_1(u), \tag{3.32}$$

which corresponds to the lower component of the bag wave function.

We will make a brief note on the inclusion of a quark mass, which will be discussed when looking at the in-medium calculations of the quark distributions. When a quark mass is included the terms that will be altered in the evaluation of the quark wave function will be N, Ω, $T(v)$, and $s_2(u)$.

If we make the assumption that $|\mu\rangle$ is a 56-plet SU(6) wave function for the proton with $m = +\frac{1}{2}$ we have the matrix elements

$$\begin{aligned}
\langle\mu|P_{u,+\frac{1}{2}}|\mu\rangle &= \frac{5}{3}, \\
\langle\mu|P_{u,-\frac{1}{2}}|\mu\rangle &= \frac{1}{3}, \\
\langle\mu|P_{d,+\frac{1}{2}}|\mu\rangle &= \frac{1}{3}, \\
\langle\mu|P_{d,-\frac{1}{2}}|\mu\rangle &= \frac{2}{3},
\end{aligned} \tag{3.33}$$

where $\langle\mu|P_{u,+\frac{1}{2}}|\mu\rangle$ is the number of quarks in the proton with flavour up and spin $+\frac{1}{2}$. We then obtain the expressions for the quark distributions,

$$u^{\uparrow\downarrow}_{(2)}(x) = F_{(2)}(x) \pm \frac{2}{3} G_{(2)}(x), \tag{3.34}$$

and

$$d^{\uparrow\downarrow}_{(2)}(x) = \frac{1}{2}F_{(2)}(x) \mp \frac{1}{6}G_{(2)}(x), \tag{3.35}$$

where the u and d refer to the up and down quark distributions respectively, and the subscript (2) is an indication that this corresponds to the contribution from the two-quark intermediate state, which for now is the only contribution we have considered.

The term $F_{(2)}(x)$ corresponds to the spin-independent distribution. It is determined by replacing $|\tilde{\Psi}^{\uparrow\downarrow}_m(\mathbf{p}_n)|^2$ in Eq. (3.19) with the part of Eq. (3.28) that includes the term $f(\mathbf{p}_n)$. We will note that for the sum over m; if the u-quark matrix elements are used then a factor of 1 will appear in front of $F_{(2)}(x)$, and if the d-quark matrix elements are used then a factor of $\frac{1}{2}$ will appear. Doing this, and performing the sum over m using the u-quark matrix elements, we have

$$\begin{aligned}
F_{(2)}(x) &= \frac{M}{(2\pi)^2}\sum_m \langle\mu|P_{f,m}|\mu\rangle \int_{\frac{|M^2(1-x)^2-M_n^2|}{2M(1-x)}}^{\infty} p_n dp_n \frac{|\phi_2(\mathbf{p}_n)|^2}{|\phi_3(\mathbf{0})|^2}\left(\frac{1}{2}f(\mathbf{p}_n)\right) \\
&= \frac{M}{(2\pi)^2}\left(\frac{1}{3}+\frac{5}{3}\right)\int_{\frac{|M^2(1-x)^2-M_n^2|}{2M(1-x)}}^{\infty} p_n dp_n \frac{|\phi_2(\mathbf{p}_n)|^2}{|\phi_3(\mathbf{0})|^2}\left(\frac{1}{2}f(\mathbf{p}_n)\right) \\
\implies F_{(2)}(x) &= \frac{M}{(2\pi)^2}\int_{\frac{|M^2(1-x)^2-M_n^2|}{2M(1-x)}}^{\infty} p_n dp_n \frac{|\phi_2(\mathbf{p}_n)|^2}{|\phi_3(\mathbf{0})|^2}\left(f(\mathbf{p}_n)\right).
\end{aligned} \tag{3.36}$$

The term $G_2(x)$ corresponds to the spin-dependent distributions. Similarly, it is determined by replacing $|\tilde{\Psi}^{\uparrow\downarrow}_m(\mathbf{p}_n)|^2$ in Eq. (3.19) with the part of Eq. (3.28) that includes the term $g(\mathbf{p}_n)$. We will note that for the sum over m; if the u-quark matrix elements are used then a factor of $\frac{2}{3}$ will appear in front of $G_{(2)}(x)$, and if the d-quark matrix elements are used then a factor of $-\frac{1}{6}$ will appear. Doing this, and performing the sum over m using the u-quark matrix elements, we have

$$\begin{aligned}
\frac{2}{3}G_{(2)}(x) &= \frac{M}{(2\pi)^2}\sum_m \langle\mu|P_{f,m}|\mu\rangle \int_{\frac{|M^2(1-x)^2-M_n^2|}{2M(1-x)}}^{\infty} p_n dp_n \frac{|\phi_2(\mathbf{p}_n)|^2}{|\phi_3(\mathbf{0})|^2}\left(\frac{1}{2}(-1)^{m+\frac{3}{2}}g(\mathbf{p}_n)\right) \\
&= \frac{M}{(2\pi)^2}\left((-1)\frac{1}{3}+(+1)\frac{5}{3}\right)\int_{\frac{|M^2(1-x)^2-M_n^2|}{2M(1-x)}}^{\infty} p_n dp_n \frac{|\phi_2(\mathbf{p}_n)|^2}{|\phi_3(\mathbf{0})|^2}\left(\frac{1}{2}g(\mathbf{p}_n)\right) \\
&= \frac{2}{3}\frac{M}{(2\pi)^2}\int_{\frac{|M^2(1-x)^2-M_n^2|}{2M(1-x)}}^{\infty} p_n dp_n \frac{|\phi_2(\mathbf{p}_n)|^2}{|\phi_3(\mathbf{0})|^2}\left(g(\mathbf{p}_n)\right) \\
\implies G_{(2)}(x) &= \frac{M}{(2\pi)^2}\int_{\frac{|M^2(1-x)^2-M_n^2|}{2M(1-x)}}^{\infty} p_n dp_n \frac{|\phi_2(\mathbf{p}_n)|^2}{|\phi_3(\mathbf{0})|^2}\left(g(\mathbf{p}_n)\right).
\end{aligned} \tag{3.37}$$

We can see from the form of the u and d distributions that the structure functions are just scaled versions of $F_{(2)}(x)$ and $G_{(2)}(x)$.

In Fig. 3.2 we show $F_{(2)}(x)$ and $G_{(2)}(x)$ for a bag radius of $R = 0.8$ fm, a nucleon mass of $M = 938.27$ MeV and an intermediate diquark mass of $M_n = \frac{3}{4}M$. The formalism here

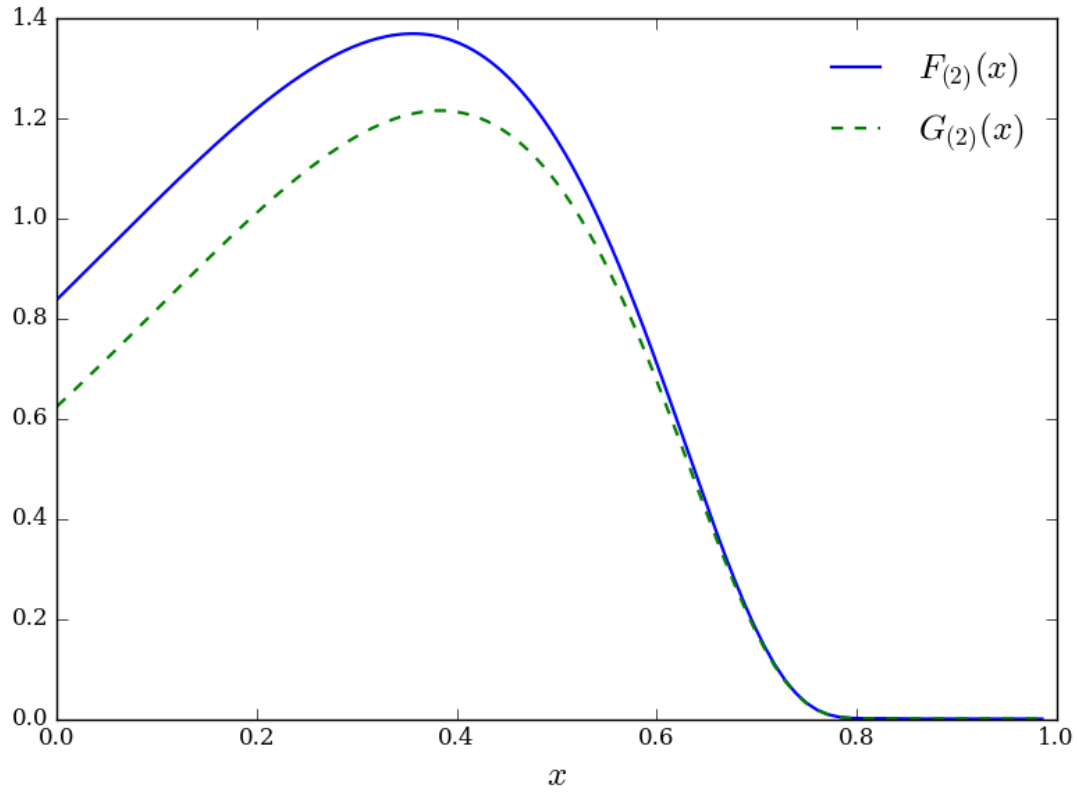

Figure 3.2: The distributions $F_{(2)}(x)$ and $G_{(2)}(x)$.

predicts different x behaviour for the spin-independent and spin-dependent structure functions. This difference arises from the non-zero $p_n^\perp$ of the quarks, and it is seen that the difference between the two distributions is greatest in the small-x region, which is where $p_n^\perp$ is large compared with p^+.

A key feature of these distributions is that the integrals of $F_2(x)$ and $G_2(x)$ can be calculated analytically from $-\infty$ to ∞, or equivalently from $-\infty$ to 1. This will be important for including the four-quark intermediate states. The integrals have the result

$$\int_{-\infty}^{1} F_{(2)}(x)dx = 1, \tag{3.38}$$

and

$$\int_{-\infty}^{1} G_{(2)}(x)dx = 0.789 \text{ for } \Omega = 2.04. \tag{3.39}$$

The integrals from 0 to 1 are determined numerically and have the result

$$\int_{0}^{1} F_{(2)}(x)dx = 0.744, \tag{3.40}$$

and

$$\int_0^1 G_{(2)}(x)dx = 0.645 \text{ for } \Omega = 2.04. \tag{3.41}$$

An important point about these integrals is that they are independent of all parameters, except for the dependence of $G_{(2)}(x)$ on the quark energy Ω and hence the quark mass m_q.

3.2.2 The Four-Quark Intermediate States

We now focus our attention on the four-quark intermediate states depicted in Fig. 3.1. Their contributions can be determined in a similar way to the two-quark intermediate state [63], but such a procedure will not be followed here. We will parametrize the four-quark states such that they simply pick up the contribution of the two-quark state from $-\infty$ to 0. We will include the four-quark states such that we have the condition

$$\int_{-\infty}^1 dx\ F_{(2)}(x) = \int_0^1 dx\left[F_{(2)}(x) + F_{(4)}(x)\right], \tag{3.42}$$

where $F_{(4)}(x)$ denotes the contribution to the integral from only the four-quark intermediate states. $G_{(4)}(x)$ is included in an equivalent way.

The four-quark states will be approximated by the function $C(1-x)^7$, which is very similar to the actual shape of $F_{(4)}(x)$ [63], where C is determined such that we have the desired normalization. We can simply rearrange Eq. (3.42) to obtain the normalisation constant C. Hence, we shall include the four-quark states via the approximation

$$F_{(4)}(x) = C(1-x)^7, \tag{3.43}$$

where

$$C = \frac{\int_{-\infty}^1 dx\ F_{(2)}(x) - \int_0^1 dx\ F_{(2)}}{\int_0^1 dx\ (1-x)^7}. \tag{3.44}$$

An equivalent expression is used for the spin-dependent case.

We take this approach because the calculated model distribution $F_{(4)}(x)$ will peak around the value of $1 - M_4/M$, which will be in the negative-x region. Therefore, the tail of this distribution, which is not so reliable, will be at small positive-x. Hence, if we take the distribution $F_{(2)}(x)$, the integral from 0 to 1 plus a calculated $F_{(4)}(x)$ is not guaranteed to equal one. The valence normalization is fixed correctly by the integral of the two-quark state over x from $-\infty$ to 1. So while the phenomenology of our approach is not ideal it does ensure the correct valence normalization.

Obviously, this procedure will result in some uncertainty in the final result. However, the shape used for the four-quark state will concentrate this uncertainty to small x. This approach will not affect the distributions too much, especially for the region $x > 0.3$,

since the four-quark distribution has a rapid fall off to zero. Furthermore, after the model distributions have been evolved to a scale such that they can be compared with data, $Q^2 = 10$ GeV^2 is a good standard, the uncertainty will move to even smaller x. As a result one should not look too deeply into the results in the low-x region.

3.2.3 The One-Gluon Exchange

We will now look at an improvement of the model. One physical effect that has been known to affect the spin-flavour dependence of the quark distributions is the one-gluon exchange [68]. Due to its noticeable contribution, the one gluon-exchange effect is an important inclusion in model calculations, and it is analogous to the hyperfine splitting in atomic physics. Referring to the process in Fig. 3.1 with the diquark intermediate state; the diquark mass depends on its spin configuration. If the diquark is in a spin-singlet state, then the quark spins are anti-aligned resulting in a spin-zero state ($s = 0$), this is termed the scalar intermediate state and has the lower mass ($M_{n,s}$). If the diquark is in a spin-triplet state, then the quark spins are aligned resulting in a spin-1 state ($s = 1$), this is termed the vector intermediate state and has the higher mass ($M_{n,v}$).

The magnitude of the mass splitting can be determined from the nucleon-delta baryon ($N - \Delta$) mass difference, assuming this has the same origin. Explicitly, one finds the scalar intermediate state mass is about 150 MeV lighter than a diquark without hyperfine splitting, and the vector intermediate state mass is about 50 MeV higher [69]. In the absence of the gluon exchange correction the mass of the diquark bag is taken, by the viral theorem, to be $\frac{3}{4}$ of the nucleon's mass ($M_n = \frac{3}{4}M$).

The spin-flavour matrix elements that appear in Eq. (3.19) are dependent on the spin state of the spectator diquark bag, and are given by

$$\begin{aligned}
\langle \mu, s=0 | P_{u,+\frac{1}{2}} | \mu, s=0 \rangle &= \frac{3}{2}, \quad \langle \mu, s=1 | P_{u,+\frac{1}{2}} | \mu, s=1 \rangle &&= \frac{1}{6}, \\
\langle \mu, s=0 | P_{u,-\frac{1}{2}} | \mu, s=0 \rangle &= 0, \quad \langle \mu, s=1 | P_{u,-\frac{1}{2}} | \mu, s=1 \rangle &&= \frac{1}{3}, \\
\langle \mu, s=0 | P_{d,+\frac{1}{2}} | \mu, s=0 \rangle &= 0, \quad \langle \mu, s=1 | P_{d,+\frac{1}{2}} | \mu, s=1 \rangle &&= \frac{1}{3}, \\
\langle \mu, s=0 | P_{d,-\frac{1}{2}} | \mu, s=0 \rangle &= 0, \quad \langle \mu, s=1 | P_{d,-\frac{1}{2}} | \mu, s=1 \rangle &&= \frac{2}{3}.
\end{aligned} \tag{3.45}$$

Using these matrix elements in Eq. (3.19) gives the quark distributions [63]

$$u^{\uparrow\downarrow}_{(2)}(x) = \left[\frac{3}{4}F_{(2)s}(x) + \frac{1}{4}F_{(2)v}(x)\right] \pm \frac{2}{3}\left[\frac{9}{8}G_{(2)s}(x) - \frac{1}{8}G_{(2)v}(x)\right], \tag{3.46}$$

and

$$d^{\uparrow\downarrow}_{(2)}(x) = \frac{1}{2}F_{(2)v}(x) \mp \frac{1}{6}G_{(2)v}(x). \tag{3.47}$$

The subscripts s and v indicate that the diquark masses $M_{n,s}$ and $M_{n,v}$, respectively, are to be used when evaluating the distributions $F_{(2)}(x)$ and $G_{(2)}(x)$, which are given

in Eq. (3.36) and (3.37). We can see that the u-quark distribution is dominated by the scalar intermediate state, and the d-quark is given solely by the vector intermediate state.

The four-quark intermediate states are included as before and are determined separately for the scalar and vector case for F and G, so before the quark distributions are calculated one must include the four-quark states such that the following is satisfied;

$$\begin{aligned}\int_{-\infty}^{1} dx\ F_{(2)s}(x) &= \int_{0}^{1} dx\ \left[F_{(2)s}(x) + F_{(4)s}(x)\right], \\ \int_{-\infty}^{1} dx\ F_{(2)v}(x) &= \int_{0}^{1} dx\ \left[F_{(2)v}(x) + F_{(4)v}(x)\right],\end{aligned} \tag{3.48}$$

and equivalently for $G_{(2)s}(x)$ and $G_{(2)v}(x)$. As before, the four-quark distribution is given by $C(1-x)^7$, where C ensures that these normalization requirements are satisfied.

3.2.4 Quark Distributions at the Model Scale

We have the required expressions to determine the quark distributions and hence the structure functions for both the spin-independent and spin-dependent case. Starting from the quark expressions in Eq. (3.46) and (3.47) we can determine required distributions needed for the structure functions.

For the unpolarized structure function we will need the following;

$$\begin{aligned}u(x) &= u^{\uparrow}(x) + u^{\downarrow}(x) \\ &= \left[\frac{3}{4}F_s(x) + \frac{1}{4}F_v(x) + \frac{2}{3}\left(\frac{9}{8}G_{(2)s}(x) - \frac{1}{8}G_{(2)v}(x)\right)\right] \\ &\quad + \left[\frac{3}{4}F_s(x) + \frac{1}{4}F_v(x) - \frac{2}{3}\left(\frac{9}{8}G_{(2)s}(x) - \frac{1}{8}G_{(2)v}(x)\right)\right] \\ &= \frac{3}{2}F_s(x) + \frac{1}{2}F_v(x),\end{aligned} \tag{3.49}$$

and

$$\begin{aligned}d(x) &= d^{\uparrow}(x) + d^{\downarrow}(x) \\ &= \left[\frac{1}{2}F_v(x) - \frac{1}{6}G_v(x)\right] + \left[\frac{1}{2}F_v(x) + \frac{1}{6}G_v(x)\right] \\ &= F_v(x).\end{aligned} \tag{3.50}$$

To be clear on notation, choosing one term as an example, $F_s(x)$ contains both the two-quark and four-quark component where the scalar diquark mass $M_{n,s}$ is used as the intermediate state mass for determining Eq. (3.36) and (3.43). The u and d distributions

have the following integral results;

$$\int_0^1 dx\; u(x) = \int_0^1 dx \left(u^{\uparrow}(x) + u^{\downarrow}(x)\right) = 2.00, \tag{3.51}$$

$$\int_0^1 dx\; d(x) = \int_0^1 dx \left(d^{\uparrow}(x) + d^{\downarrow}(x)\right) = 1.00. \tag{3.52}$$

Since there are two valence u-quarks and one valence d-quark in the proton, if we integrate over all polarizations then we expect these results.

The unpolarized structure function of the proton is then given by

$$\begin{aligned}\mathcal{F}_2(x) &= x \sum_f e_f^2 q_f(x) \\ &= x\left[\left(\frac{2}{3}\right)^2 u(x) + \left(\frac{1}{3}\right)^2 d(x)\right].\end{aligned} \tag{3.53}$$

For the polarized structure function we will need the following;

$$\begin{aligned}\Delta u(x) &= u^{\uparrow}(x) - u^{\downarrow}(x) \\ &= \left[\frac{3}{4}F_s(x) + \frac{1}{4}F_v(x) + \frac{2}{3}\left(\frac{9}{8}G_{(2)s}(x) - \frac{1}{8}G_{(2)v}(x)\right)\right] \\ &\quad - \left[\frac{3}{4}F_s(x) + \frac{1}{4}F_v(x) - \frac{2}{3}\left(\frac{9}{8}G_{(2)s}(x) - \frac{1}{8}G_{(2)v}(x)\right)\right] \\ &= \frac{3}{2}G_s(x) - \frac{1}{6}G_v(x),\end{aligned} \tag{3.54}$$

and

$$\begin{aligned}\Delta d(x) &= d^{\uparrow}(x) - d^{\downarrow}(x) \\ &= \left[\frac{1}{2}F_v(x) - \frac{1}{6}G_v(x)\right] - \left[\frac{1}{2}F_v(x) + \frac{1}{6}G_v(x)\right] \\ &= \frac{1}{3}G_v(x).\end{aligned} \tag{3.55}$$

The distributions $G_s(x)$ and $G_v(x)$ contain both the two-quark and four-quark intermediate states. The Δu and Δd distributions have the following integral results;

$$\int_0^1 dx\; \Delta u(x) = \int_0^1 dx \left(u^{\uparrow}(x) - u^{\downarrow}(x)\right) = 1.05, \tag{3.56}$$

$$\int_0^1 dx\; \Delta d(x) = \int_0^1 dx \left(d^{\uparrow}(x) - d^{\downarrow}(x)\right) = -0.26. \tag{3.57}$$

The polarized structure function of the proton is then given by

$$\begin{aligned}g_1(x) &= \frac{1}{2}\sum_f e_f^2 \Delta q_f(x) \\ &= \frac{1}{2}\left[\left(\frac{2}{3}\right)^2 \Delta u(x) + \left(\frac{1}{3}\right)^2 \Delta d(x)\right].\end{aligned} \tag{3.58}$$

The presented distributions will contain the two and four-quark intermediate states as well as the one gluon exchange effect. The approach for producing the quark distributions will be to choose parameters, bag radius and diquark masses, for the two-quark component and then add in the term $C(1-x)^7$ corresponding to the four-quark components to fix the normalization such that Eq. (3.48) is satisfied.

We will first present the quark distributions at the model scale μ^2, in order to compare with experimental data the distributions must be evolved, this is described in the next section. In Fig. 3.3 we show the unpolarized and polarized quark distributions for $R = 0.6$ fm, $M_{n,s} = 550$ MeV, and $M_{n,v} = 750$ MeV. This corresponds to a model scale of about 0.04 GeV^2. This value of μ^2 is quite low, and comes about from the bag model giving quark distributions that peak around the mid-x region.

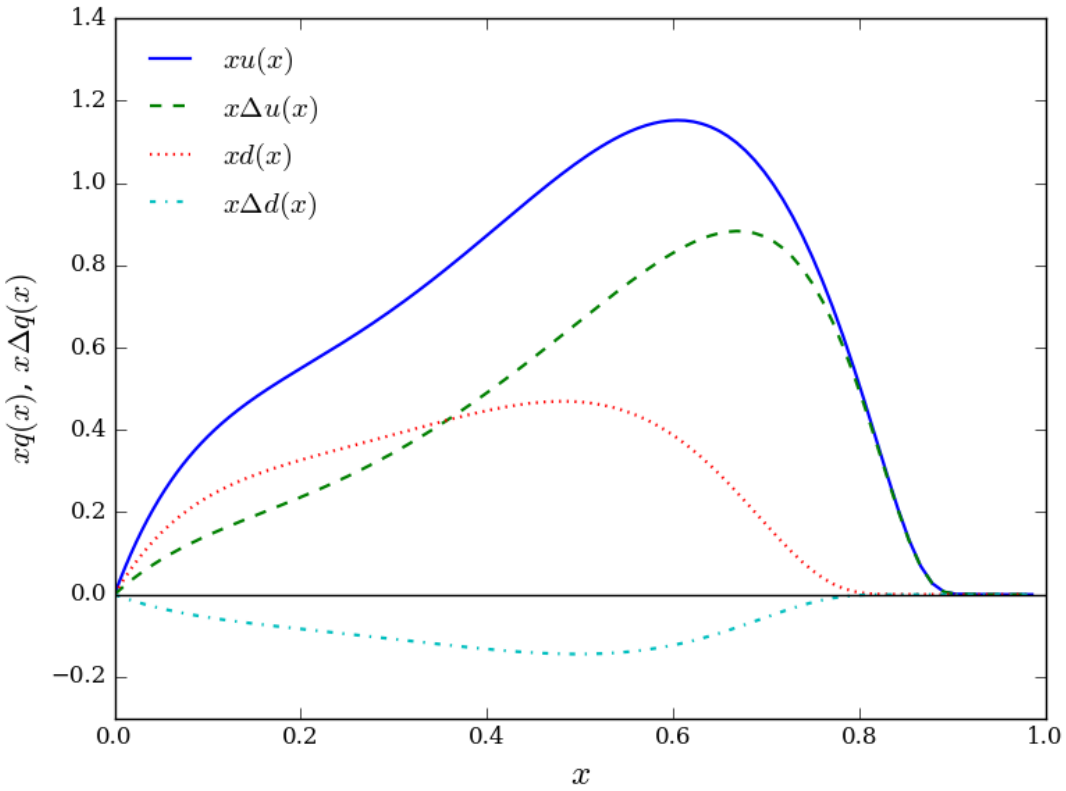

Figure 3.3: Unpolarized and polarized quark distributions in the bag at the model scale.

There are a couple of key features to point out about the quark distributions in the bag model. It can be seen that the distributions peak in the mid-x region, the inclusion of the gluon exchange actually pushes the peak to a larger x value. This is not a problem, and is a property of the bag model, and also depends on the parameters

chosen. However, this does result in the model scale being quite low, around $\mu^2 = 0.04$ GeV^2 (see next section), and one would be hesitant to perform QCD evolution at a starting scale any lower than this as uncertainties in the evolution process become more prominent at starting scales that are too low. It is also important to note that the distributions die off quite rapidly to zero at an x value above 0.8. Therefore, when the ratios of distributions are determined the high-x region should be taken with caution.

3.3 Evolving the Model Distributions

To determine the model scale at which the distributions are calculated, we will evolve the u-quark distribution to a scale of $Q^2 = 10$ GeV^2 and compare the result with known experimental data, the starting scale will be varied until the evolved distribution best matches the experimental data, this starting scale will then be used for all other distributions. The evolution is performed using the QCDNUM program [20].

In Fig. 3.4 we have used the following parameters; $R = 0.6$ fm, $M_{n,s} = 550$ MeV, and $M_{n,v} = 750$ MeV. After testing a few starting scales it was found that the evolved u-quark distribution best matches the data for a starting scale of $\mu^2 = 0.04$ GeV^2. This corresponds to $\alpha_s = 2.05$ at the starting scale, and $\alpha_s = 0.23$ at the finish scale of $Q^2 = 10$ GeV^2, giving a value of $\Lambda_{\rm QCD}$=0.02 GeV^2 (=141 MeV), which can be evaluated from Eq. (2.20). This value for $\Lambda_{\rm QCD}$ is a bit low, which is due to the low model scale. Further details on the $\alpha_s(Q^2)$ evolution can be found in the QCDNUM write up [20]. The data used for comparison is the modified leading order (LO) MRST2007 parametrization of the valence u-quark distribution [70]. The evolved valence u-quark distribution from the bag model matches the data reasonably well, and these parameters give the best fit of our model distribution to the data. In Appendix C we show the model scale corresponding to various parameters.

In Fig. 3.5 and 3.6 we show the spin-independent structure function for the proton and neutron, respectively. In Fig. 3.7 and Fig. 3.8 we show the spin-dependent structure function for the proton and neutron, respectively. The four plots are for the following parameters; $R = 0.6$ fm, $M_{n,s} = 550$ MeV, $M_{n,v} = 750$ MeV, corresponding to a model scale of $\mu^2 = 0.04$ GeV^2.

A few extra components come into the evolved structure functions compared to the model scale. The evolution process produces anti-quark, a strange quark, and a gluon distribution. We will not be including the gluon distribution into our calculations, as this only adds on a small correction to structure function of the nucleon, and also has a negligible impact in the valence region, which is our main area of interest. We will be including the anti-quark distributions into our structure functions as well as the strange quark distribution, which are not explicitly calculated at the model scale, but are dynamically generated in the evolution process.

Therefore, our evolved structure functions are the full structure functions containing

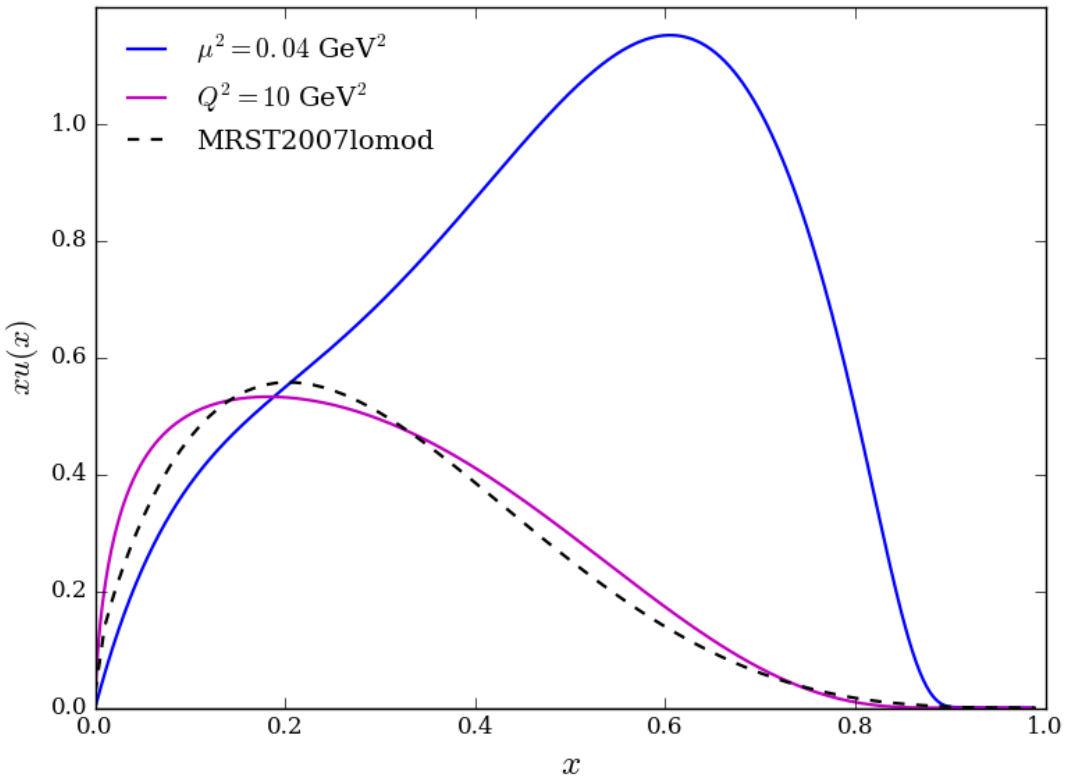

Figure 3.4: u-quark distribution in the bag model. The solid curves correspond to the theoretical results at both the model scale μ^2, corresponding to the largest peak, and then evolved to $Q^2 = 10$ GeV^2 for comparison with data for the valence u-quark distribution from Ref. [70]

the anti-quark as well as strange quark distributions, shown in Eq. (2.11). This can be seen in the unpolarized structure function figures where there is a clear low-x increase in the evolved distributions compared to the model scale distributions.

In a model that has SU(6)-symmetry then $g_1^n(x)$ would be zero everywhere. The splitting from the one gluon exchange is the dominant effect that causes it to become finite. The QCD evolution also results in a small value for $g_1^n(x)$, even if it had been zero everywhere at the model scale. This is because the singlet and non-singlet parts evolve differently. The effect due to the evolution is about $\frac{1}{3}$ of that due to the one gluon exchange.

3.4 Chapter Summary

In this chapter we went through our procedure for calculating the quark distributions in the bag model. With these distributions we were able to determine the spin-dependent

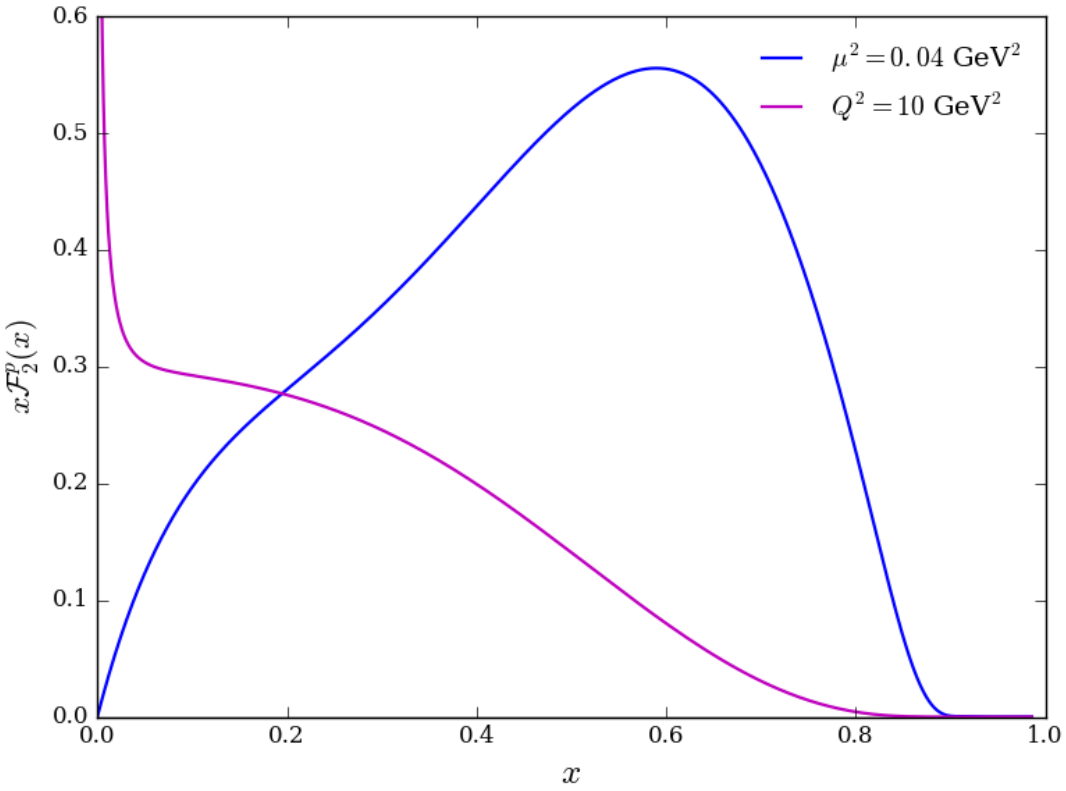

Figure 3.5: Spin-independent structure function for the proton in the bag model. The larger peak corresponds to the model scale μ^2, and then evolved to $Q^2 = 10$ GeV^2.

and spin-independent structure functions for the proton and neutron. For the calculations we set the quark mass to zero. We then evolved the distributions from the model scale to a scale of $Q^2 = 10$ GeV^2.

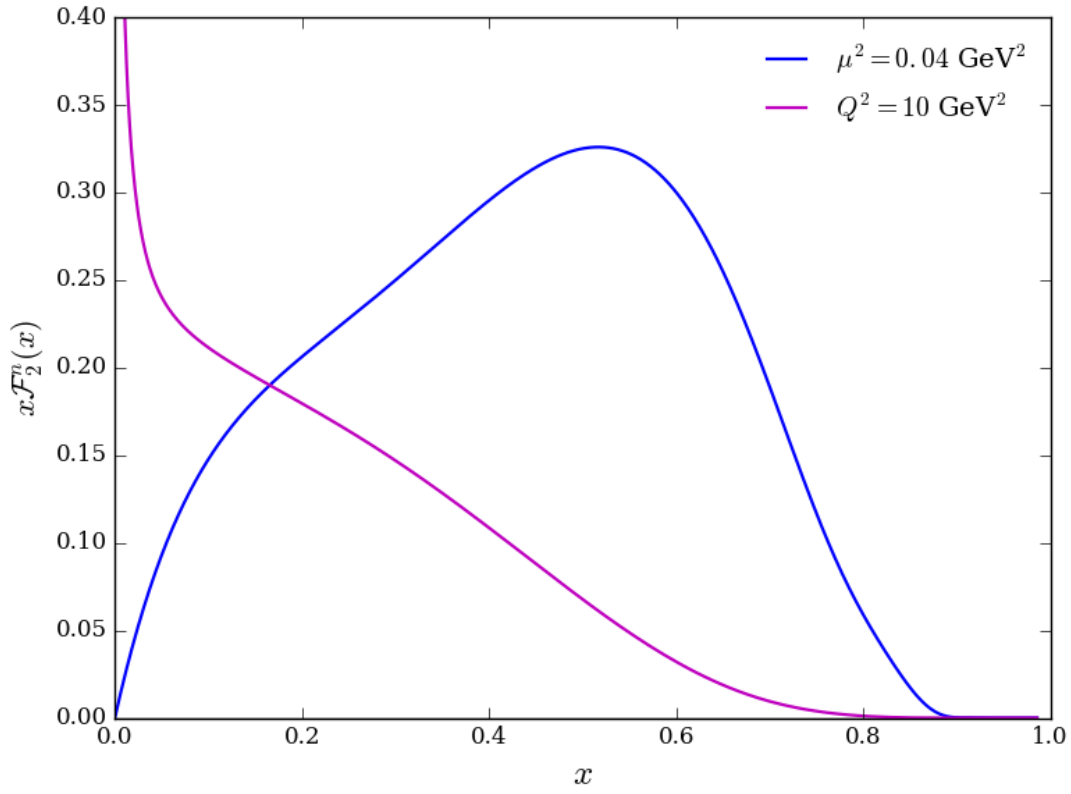

Figure 3.6: Spin-independent structure function for the neutron in the bag model. The larger peak corresponds to the model scale μ^2, and then evolved to $Q^2 = 10$ GeV^2.

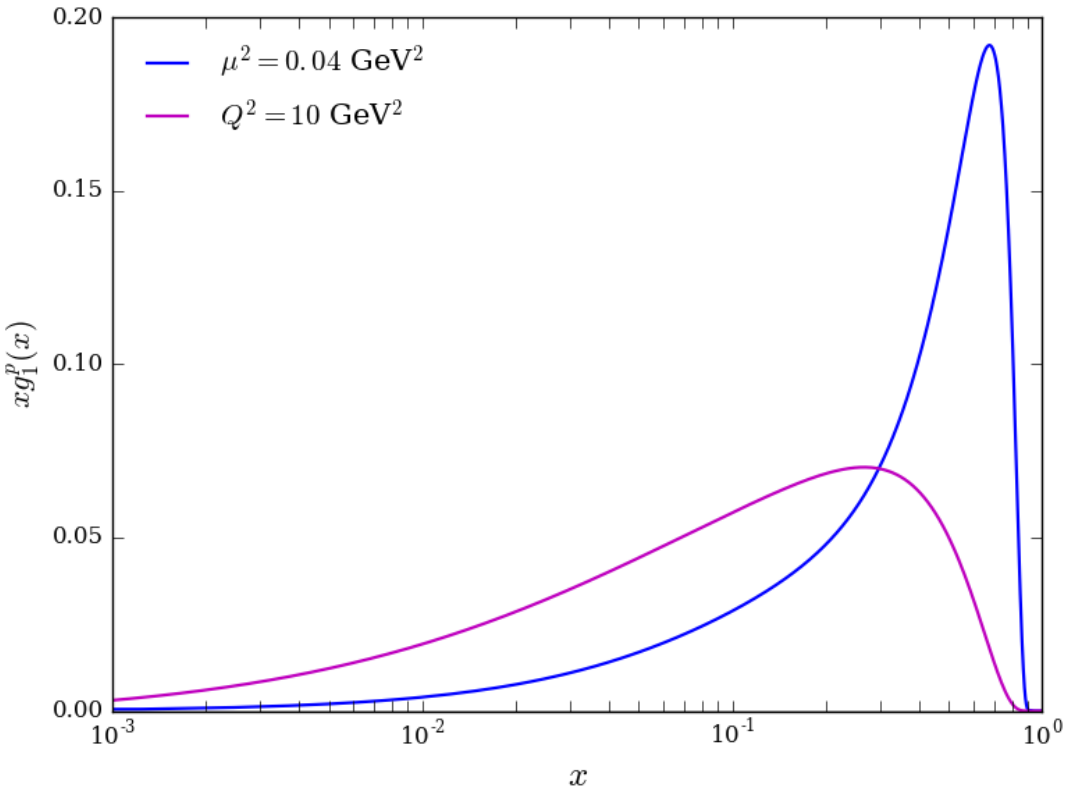

Figure 3.7: Spin-dependent structure function for the proton in the bag model. The larger peak corresponds to the model scale μ^2, and then evolved to $Q^2 = 10$ GeV^2.

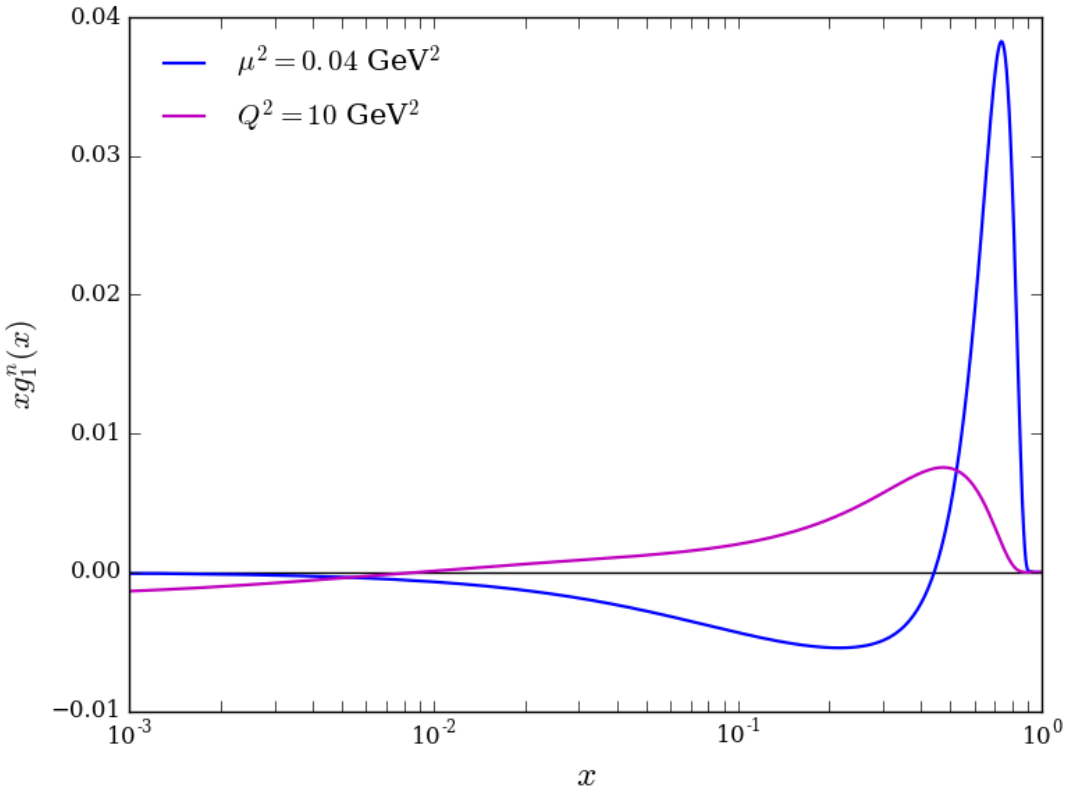

Figure 3.8: Spin-dependent structure function for the neutron in the bag model. The larger peak corresponds to the model scale μ^2, and then evolved to $Q^2 = 10$ GeV^2.

Chapter 4

In-Medium Structure Functions

Having determined the free structure functions of the nucleon, we now move on to discussing the in-medium case. In this chapter we will show how we include the in-medium modifications into the calculation for the quark distributions of the bound nucleon. There are three effects that we will be accounting for in the bound nucleon; the σ mean field, Fermi motion, and the ω mean field. These effects will be explicitly included in the two-quark intermediate state, and the four-quark intermediate states will be included as an approximation at the end to satisfy normalization requirements, as done for the free case.

With our in-medium structure functions we will be able to make predictions of both the unpolarized and polarized EMC effect.

4.1 The σ Field

The σ field, or scalar field, has two effects on a bound nucleon that will be considered. Firstly, the quark wave function will be altered due to the effective quark mass (m_q^*) that comes from the coupling of the σ field to a quark. Secondly, the effect of the overall coupling of the σ field to the nucleon will result in an effective nucleon mass (M^*) as well as effective diquark state masses for both the singlet and vector intermediate states ($M_{n,s}^*$ and $M_{n,v}^*$, respectively).

4.1.1 The Altered Quark Wave Function

We will now look at the effect of the σ mean field on the quark wave function. A quark inside a bound nucleon is effectively sitting in a scalar potential well generated by the σ mesons, and this will alter its mass. The effective quark mass of a bound nucleon is given by [71]

$$m_q^* = m_q - g_\sigma^q \bar{\sigma}, \tag{4.1}$$

where m_q is the quark mass of a free nucleon, and $g_\sigma^q \bar{\sigma}$ is the coupling strength of the σ mean field to the quark inside a bound nucleon. In order to determine this coupling

strength we refer to a plot from Guichon, Saito, Rodionov, and Thomas [56], shown in Fig. 4.1. The symbol $g_\sigma \bar{\sigma}$ is the coupling of the σ mean field to the nucleon in free space. The coupling strength at nuclear matter density corresponds to values along $\frac{\rho_B}{\rho_0} = 1$.

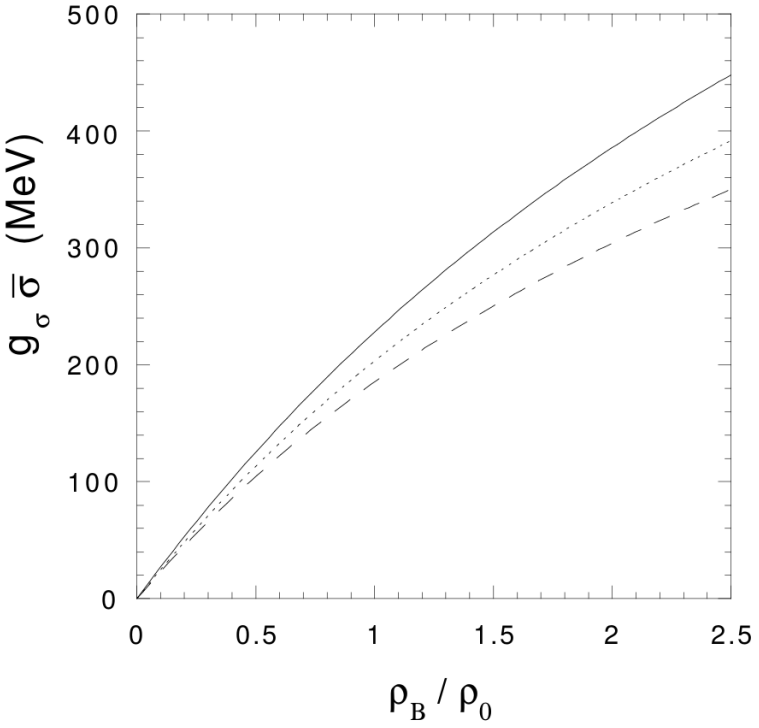

Figure 4.1: Mean-field values of the σ meson for various bag radii as a function of baryonic density of the bound nucleons (ρ_B) as taken from Ref. [56]. The solid, dotted, and dashed curves show $g_\sigma \bar{\sigma}$ for a bag radius of $R = 0.6$, 0.8, and 1.0 fm, respectively.

Referring to Fig. 4.1, at nuclear matter density for a bag radius of $R = 0.6$ fm we have a value of $g_\sigma \bar{\sigma} \simeq 225$ MeV. There is some variation in the strength of the σ mean field coupling in different variations of the QMC model and we will therefore try various values of $g_\sigma \bar{\sigma}$ when looking at the EMC effect. From the coupling of the σ mean field to the nucleon as a whole ($g_\sigma \bar{\sigma}$), we can determine the value of the coupling to an individual quark ($g_\sigma^q \bar{\sigma}$).

The nuclear coupling constant for the σ mean field is given by [56]

$$g_\sigma = 3 g_\sigma^q S(\sigma = 0). \tag{4.2}$$

The final quantity in the above expression is the integral of the quark fields over the bag volume,

$$S(\sigma = 0) = \int_{Bag} dV \; \bar{q} q. \tag{4.3}$$

This integral will be dependant on the bag radius, since the radius will have an effect on the quark fields. For different radii we have the results

$$S(\sigma = 0) = 0.4819 \text{ for } R = 0.6 \text{ fm} , \tag{4.4}$$
$$S(\sigma = 0) = 0.4827 \text{ for } R = 0.8 \text{ fm} , \tag{4.5}$$
$$S(\sigma = 0) = 0.4834 \text{ for } R = 1.0 \text{ fm} . \tag{4.6}$$

Doing some manipulations on Eq. (4.2) we can obtain the expression of the σ field coupling to a quark,

$$g_\sigma^q \bar{\sigma} = \frac{1}{3S(\sigma = 0)} g_\sigma \bar{\sigma}. \tag{4.7}$$

As an example, if we take a bag radius of $R = 0.6$ fm and $g_\sigma \bar{\sigma} = 180$ MeV we get the result $g_\sigma^q \bar{\sigma} \simeq 124.5$ MeV and this corresponds to an effective quark mass of $m_q^* \simeq -124.5$ MeV, where we have taken the quark mass of a free nucleon to be zero.

Because of the modification of the quark mass in a bound nucleon, we must consider how this alters the quark wave function in the bag model. The quark wave function of a bound nucleon in the bag is given by [67]

$$\Psi_m^*(x) = N^{*2} \begin{pmatrix} j_0\left(\frac{\Omega|x|}{R}\right)\chi_m \\ ib\boldsymbol{\sigma}\cdot\hat{\boldsymbol{x}} j_1\left(\frac{\Omega|x|}{R}\right)\chi_m \end{pmatrix} \Theta(R - |x|), \tag{4.8}$$

where

$$b = \left(\frac{E - m_q}{E + m_q}\right)^{\frac{1}{2}}, \tag{4.9}$$
$$E = \frac{1}{R}\left(\Omega^2 + (m_q R)^2\right)^{\frac{1}{2}}, \tag{4.10}$$

and

$$N^{*2} = \frac{1}{4\pi} \frac{E^2 - m_q^2}{R^3 j_0(\Omega)^2 \left[2E\left(E - \frac{1}{R}\right) + \frac{m_q}{R}\right]}. \tag{4.11}$$

The b factor appearing in the lower component of the bag wave function leads to an alteration of the expression for $s_2(u)$ (Eq. (3.32)), where we now have

$$s_2^*(u) = b\left(2j_0(\Omega)j_1(u) - \frac{u}{\Omega}s_1(u)\right), \tag{4.12}$$

while the expression for $s_1(u)$ (Eq. (3.31)) remains unchanged. The normalizations become

$$|\phi_2(\mathbf{p}_n)|^{*2} = \frac{4\pi R}{u}\left(\frac{2\pi N^{*2} R^4}{\Omega^4}\right)^2 \int \frac{dv}{v} sin\left(\frac{2vu}{\Omega}\right) T^{*2}(v), \tag{4.13}$$

and

$$|\phi_3(\mathbf{0})|^{*2} = 4\pi \left(\frac{2\pi N^{*2} R^4}{\Omega^4}\right)^3 \int \frac{dv}{v} T^{*3}(v), \tag{4.14}$$

where the overlap integral of the bag wave function now becomes

$$\begin{aligned} T^*(v) &= T_t + b^2 T_b \\ &= \left[(\Omega - v)sin(2v) + (1 - sin^2(\Omega)) - cos(\Omega)cos(\Omega - 2v)\right] \\ &\quad + b^2 \Bigg[\left(1 - \frac{4v^2}{2\Omega^2}\right) sin^2(\Omega) - \frac{2}{\Omega} sin(\Omega)cos(\Omega - 2v) + \frac{2}{\Omega} sin(\Omega)cos(\Omega) + \Omega sin(2v) \\ &\quad - sin(\Omega)sin(\Omega - 2v) - vsin(2v) \Bigg]. \end{aligned} \tag{4.15}$$

In order to determine the eigenfrequency we need to solve the equation

$$tan(\Omega) = \frac{\Omega}{1 - m_q R - (\Omega^2 + (m_q R)^2)^{\frac{1}{2}}}. \tag{4.16}$$

As an example; a quark mass of $m_q = -124.5$ MeV gives an in-medium eigenfrequency of $\Omega \simeq 1.83$.

We have just considered the effect of the σ mean field on the quark mass and how this alters the quark wave function.

4.1.2 The Altered Nucleon Mass

Having explored the effect of the σ mean field on an individual quark, we will now look at how this mean field impacts the bound nucleon as a whole. The σ mean field for the bound nucleon is included through the effective nucleon and diquark state masses. The effective mass of a bound nucleon is given by [72]

$$M^*(\bar{\sigma}) = M - g_\sigma \bar{\sigma} + \frac{d}{2} (g_\sigma \bar{\sigma})^2, \tag{2.24}$$

where $d = 0.22R$, with R the bag radius. Studies have shown that Eq. (2.24) is quite accurate up to values of $g_\sigma \bar{\sigma} = 400$ MeV [72], which will be sufficient for our purposes.

In order to determine the effective diquark state masses we will first need to work out the strength of the vector field. We will describe how the vector field is used to determine the effective diquark state masses, but save the discussion for including the vector field effects into the quark distributions for the next section. The vector field is generated by the ω mesons, and is responsible for the short range repulsion between nucleons. V_0 is the zeroth component of the vector field felt by the quarks, and is essentially the strength of the vector potential. Since nuclear matter is bound, then $3V_0 = (M - M^*)$

would be an overestimate of the vector field strength, and hence $3V_0$ should be less than this. Figure 21 from Ref. [71] shows the potential strengths for different lambda (Λ) hypernuclei, so only containing two light quarks. Using the results for hypernuclei is acceptable as we will be interested in the ratio of the vector and scalar fields. For the hypernuclei lead ($^{209}_{\Lambda}$Pd), we see that at the centre of lead, which has approximately the density of nuclear matter, the vector potential is around 90 MeV and the scalar potential is around 130 MeV. Therefore, taking $3V_0$ as 65-70% of $M - M^*$ will be acceptable, and we therefore use the expression

$$3V_0 = \left(\frac{90}{130}\right)(M - M^*)\,, \tag{4.17}$$

where V_0 is the vector potential. We have a similar expression for the diquark case,

$$2V_0 = \left(\frac{90}{130}\right)(M_n - M_n^*)\,. \tag{4.18}$$

Our approach to determine the effective diquark state masses will be as follows. Determine the effective nucleon mass from Eq. (2.24). Then determine the vector potential through the equation

$$V_0 = \frac{1}{3}\left(\frac{90}{130}\right)(M - M^*)\,. \tag{4.19}$$

We then use the value of the vector potential to find the diquark state masses through

$$M^*_{n,s} = M_{n,s} - 2V_0\left(\frac{130}{90}\right), \tag{4.20}$$

$$M^*_{n,v} = M_{n,v} - 2V_0\left(\frac{130}{90}\right). \tag{4.21}$$

Having described our approach to determine the effective nucleon and diquark state masses, we can now write the quark distribution for a bound nucleon including the total effect of the σ mean field, which includes the effect on the wave function and the change of the nucleon and diquark state masses. We will drop the subscript (2) on the quark distribution for the sake of reading clarity, but we emphasize that the in-medium modifications are only applied to the two-quark intermediate state. The quark distribution is given by

$$q^{\uparrow\downarrow}_{N_0}(x) = \frac{M^*}{(2\pi)^2}\sum_m \langle\mu|P_{f,m}|\mu\rangle \int_{\frac{|M^{*2}(1-x)^2 - M_n^{*2}|}{2M^*(1-x)}}^{\infty} p_n dp_n \frac{|\phi_2(\mathbf{p}_n)|^{*2}}{|\phi_3(\mathbf{0})|^{*2}} |\tilde{\Psi}^{*\uparrow\downarrow}_m(\mathbf{p}_n)|^2, \tag{4.22}$$

where the subscript 0 indicates that only the scalar field has been included and the vector field is yet to be incorporated. From this we can obtain the expressions

$$F^*_{N_0}(x) = \frac{M^*}{(2\pi)^2}\int_{\frac{|M^{*2}(1-x)^2 - M_n^{*2}|}{2M^*(1-x)}}^{\infty} p_n dp_n \frac{|\phi_2(\mathbf{p}_n)|^{*2}}{|\phi_3(\mathbf{0})|^{*2}}\,(f(\mathbf{p}_n)^*)\,, \tag{4.23}$$

$$G^*_{N_0}(x) = \frac{M^*}{(2\pi)^2}\int_{\frac{|M^{*2}(1-x)^2 - M_n^{*2}|}{2M^*(1-x)}}^{\infty} p_n dp_n \frac{|\phi_2(\mathbf{p}_n)|^{*2}}{|\phi_3(\mathbf{0})|^{*2}}\,(g(\mathbf{p}_n)^*)\,. \tag{4.24}$$

The expressions for $|\phi_2(\mathbf{p}_n)|^{*2}$ and $|\phi_3(\mathbf{0})|^{*2}$ are given in Eq. (4.13) and (4.14), respectively. The stars on f and g are an indication that the effective masses, in-medium Ω, as well as $s_2^*(u)$, must be used for the terms in those expressions.

Summing up this part; we have just explored the effect of the σ mean field on the bound nucleon. The σ field alters the quark wave function as well as the nucleon and diquark masses.

4.2 Fermi Motion

Fermi motion is the next effect that is included into the quark distributions. It has been shown that the effect of Fermi motion on a bound nucleon can be included through a convolution of the quark distribution with a Fermi smearing function, $f_0(\tilde{y}_A)$, which is given by [73]

$$f_0(\tilde{y}_A) = \frac{3}{4}\left(\frac{E_F}{p_F}\right)^3 \left[\left(\frac{p_F}{E_F}\right)^2 - (1-\tilde{y}_A)^2\right], \tag{4.25}$$

where the distribution has support for

$$1 - \frac{p_F}{E_F} < \tilde{y}_A < 1 + \frac{p_F}{E_F}. \tag{4.26}$$

The Fermi energy is given by

$$E_F = \sqrt{p_F^2 + M^{*2}}, \tag{4.27}$$

where p_F is the Fermi momentum. The effective nucleon mass in the Fermi energy shows that the σ mean field must be included in the calculations for the Fermi motion. An acceptable value for the Fermi momentum at nuclear matter density is $p_F \simeq 265$ MeV [74]. We will be testing various values of Fermi momentum to see how this impacts the EMC effect. Since Fermi motion describes the motion of a bound nucleon as a whole, its impact will be predominantly seen in the high-x region.

Performing the convolution of the quark distribution in Eq. (4.22) with $f_0(\tilde{y}_A)$ gives the distribution

$$q_{A_0}(\tilde{x}_A) = \int d\tilde{y}_A \int dx\ \delta(\tilde{x}_A - \tilde{y}_A x)\ q_{N_0}(x) f_0(\tilde{y}_A). \tag{4.28}$$

Eliminating the δ-function integral we obtain the result

$$q_{A_0}(\tilde{x}_A) = \int d\tilde{y}_A\ \frac{1}{\tilde{y}_A}\ q_{N_0}\left(\frac{\tilde{x}_A}{\tilde{y}_A}\right) f_0(\tilde{y}_A), \tag{4.29}$$

where we remind the reader that the subscript 0 indicates that the vector field effects have not been included. From this we can obtain the distributions

$$F_{A_0}^*(\tilde{x}_A) = \int d\tilde{y}_A \, \frac{1}{\tilde{y}_A} \, F_{N_0}^* \left(\frac{\tilde{x}_A}{\tilde{y}_A} \right) f_0(\tilde{y}_A), \tag{4.30}$$

$$G_{A_0}^*(\tilde{x}_A) = \int d\tilde{y}_A \, \frac{1}{\tilde{y}_A} \, G_{N_0}^* \left(\frac{\tilde{x}_A}{\tilde{y}_A} \right) f_0(\tilde{y}_A). \tag{4.31}$$

4.3 The ω Field

Now we will discuss how we include the effect of the ω mean field, or vector field, into the calculation of the quark distribution. The quarks of a bound nucleon feel the zeroth component of the vector field, V_0, which is the strength of the vector potential. As we mentioned previously, the vector field simply shifts the definition of the energy scale. This leads to a predominantly model independent result for the modification of the in-medium quark distribution of a bound nucleon by the vector mean field [38].

The vector field is included by scaling the quark distribution $q_{A_0}(\tilde{x}_A)$, and shifting the Bjorken variable x. The in-medium quark distribution then becomes [73]

$$q_A(x_A) = \frac{\epsilon_F}{E_F} q_{A_0} \left(\tilde{x}_A = \frac{\epsilon_F}{E_F} x_A - \frac{V_0}{E_F} \right), \tag{4.32}$$

where

$$\epsilon_F = \sqrt{p_F^2 + M^{*2}} + 3V_0 \equiv E_F + 3V_0 \tag{4.33}$$

is the Fermi energy with the vector field included. The new variable x_A is the Bjorken scaling variable for the nucleon. From this we obtain our full in-medium distributions

$$F_A^*(x_A) = \frac{\epsilon_F}{E_F} F_{A_0}^* \left(\tilde{x}_A = \frac{\epsilon_F}{E_F} x_A - \frac{V_0}{E_F} \right), \tag{4.34}$$

$$G_A^*(x_A) = \frac{\epsilon_F}{E_F} G_{A_0}^* \left(\tilde{x}_A = \frac{\epsilon_F}{E_F} x_A - \frac{V_0}{E_F} \right). \tag{4.35}$$

These distributions are able to be plotted as a function of x through the relation $x_A = \frac{M}{\epsilon_F} x$ [75].

4.4 In-Medium Distributions

4.4.1 In-Medium Four-Quark Intermediate States

We have considered the effect of the σ mean field, Fermi motion, and ω mean field on the in-medium quark distributions. These effects were only applied to the two-quark intermediate state, which yields the dominant contribution. Since the four-quark

intermediate states are not explicitly calculated, there is no physical significance in applying the in-medium modifications to the four-quark term. Therefore, as done in the free case, we shall include it as a phenomenological term to satisfy normalization requirements. The four-quark term will be included so that it picks up the region of the two-quark state corresponding to the negative-x region. Hence we will desire the following to be satisfied;

$$\int_{-\infty}^{1} dx\, F_A^*(x) = \int_0^1 dx \left[F_A^*(x) + F_{(4)}^*(x)\right], \tag{4.36}$$

$$\int_{-\infty}^{1} dx\, G_A^*(x) = \int_0^1 dx \left[G_A^*(x) + G_{(4)}^*(x)\right]. \tag{4.37}$$

The four-quark term, as before, will take the form of $C^*(1-x)^7$, where C^* refers to the normalization constant such that the above requirements are satisfied.

From these we can determine the quark distributions, given in Eq. (3.46) and (3.47) for the free case, and the equivalent expression for the in-medium case are given by

$$u^{*\uparrow\downarrow}(x) = \left[\frac{3}{4}F_{A,s}^*(x) + \frac{1}{4}F_{A,v}^*(x)\right] \pm \frac{2}{3}\left[\frac{9}{8}G_{A,s}^*(x) - \frac{1}{8}G_{A,v}^*(x)\right], \tag{4.38}$$

$$d^{*\uparrow\downarrow}(x) = \frac{1}{2}F_{A,v}^*(x) \mp \frac{1}{6}G_{A,v}^*(x), \tag{4.39}$$

where we reiterate that the subscripts s and v indicate that the diquark masses $M_{n,s}^*$ and $M_{n,v}^*$, respectively, must be used when evaluating the distributions $F_A^*(x)$ and $G_A^*(x)$. The u and d distributions above include the four-quark term. From these we get the following distributions for the unpolarized case;

$$\begin{aligned} u^*(x) &= u^{*\uparrow} + u^{*\downarrow} \\ &= \frac{3}{2}F_{A,s}^*(x) + \frac{1}{2}F_{A,v}^*(x), \end{aligned} \tag{4.40}$$

and

$$\begin{aligned} d^*(x) &= d^{*\uparrow} + d^{*\downarrow} \\ &= F_{A,v}^*(x), \end{aligned} \tag{4.41}$$

where the unpolarized structure function of the proton is now given by

$$\mathcal{F}_2^*(x) = x\left[\left(\frac{2}{3}\right)^2 u^*(x) + \left(\frac{1}{3}\right)^2 d^*(x)\right]. \tag{4.42}$$

For the polarized case we have

$$\begin{aligned} \Delta u^*(x) &= u^{*\uparrow} - u^{*\downarrow} \\ &= \frac{3}{2}G_{A,s}^*(x) - \frac{1}{6}G_{A,v}^*(x), \end{aligned} \tag{4.43}$$

and

$$\begin{aligned}\Delta d^*(x) &= d^{*\uparrow} - d^{*\downarrow} \\ &= \frac{1}{3} G^*_{A,v}(x).\end{aligned} \tag{4.44}$$

where the polarized structure function of the proton is now given by

$$g_1^*(x) = \frac{1}{2}\left[\left(\frac{2}{3}\right)^2 \Delta u^*(x) + \left(\frac{1}{3}\right)^2 \Delta d^*(x)\right]. \tag{4.45}$$

4.4.2 In-Medium Results

We are now at the stage to present the results for the in-medium quark distributions and structure functions. The presented distributions will contain the two and four-quark intermediate states, as well as the full in-medium contributions, namely the σ and ω mean fields as well as Fermi motion. In Table 4.1 we give the parameters chosen for the distributions that will be shown here. The free nucleon parameters as well as the σ mean field coupling strength are chosen, and from them we can calculate the effective nucleon and quark masses, as well as the eigenfrequency and vector potential.

Set Values					
R (fm)	$g_\sigma \bar{\sigma}$ (MeV)	p_F (MeV)	M	$M_{n,s}$	$M_{n,v}$
0.6	180	220	938.27	550	750
Resultant Values					
m_q^*	Ω	V_0 (MeV)	M^*	$M^*_{n,s}$	$M^*_{n,v}$
-124.51	1.83	39.04	769.12	437.22	637.22

Table 4.1: Set and resultant values. Masses are in units MeV.

In Fig. 4.2 we show the in-medium unpolarized and polarized quark distributions for the parameters shown in Table 4.1. The in-medium quark distributions are shifted slightly to the left and peak at lower x compared to the free case.

For a direct comparison of the structure functions, we will present the in-medium and free structure functions of the proton together. In Fig. 4.3 we present the in-medium and free unpolarized structure functions for the proton at the model scale $\mu^2 = 0.04$ GeV^2 and evolved to $Q^2 = 10$ GeV^2, and in Fig. 4.4 we present the in-medium and free polarized structure functions for the proton at the model scale $\mu^2 = 0.04$ GeV^2 and evolved to $Q^2 = 10$ GeV^2. Both plots are for the parameters shown in Table 4.1.

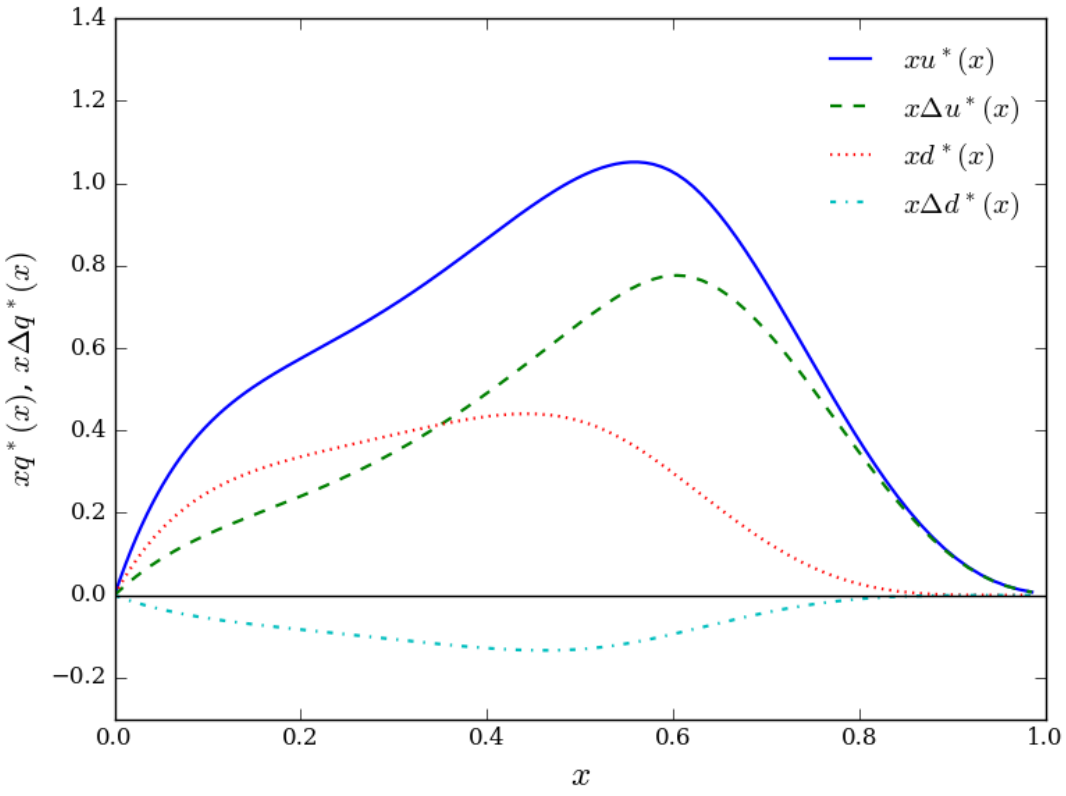

Figure 4.2: In-medium unpolarized and polarized quark distributions in the bag at a model scale of $\mu^2 = 0.04$ GeV^2.

It can be seen that for the evolved case, the in-medium structure function sits below the free one for the majority of x in both the unpolarized and polarized case. This is a very important observation. By modelling the nucleon at the quark level and allowing the quark structure to be altered when in-medium, we are observing the suppression of the in-medium structure function that is associated with the EMC effect. Our approach of applying the in-medium effects at the quark level has naturally given rise to this phenomena.

It is also very important to point out that we are observing a suppression of the in-medium structure function in both the unpolarized and polarized case. A comparison of the suppression for the unpolarized and polarized case will be looked at in the results section. For now we just state that there is definitely an observed EMC effect in both cases.

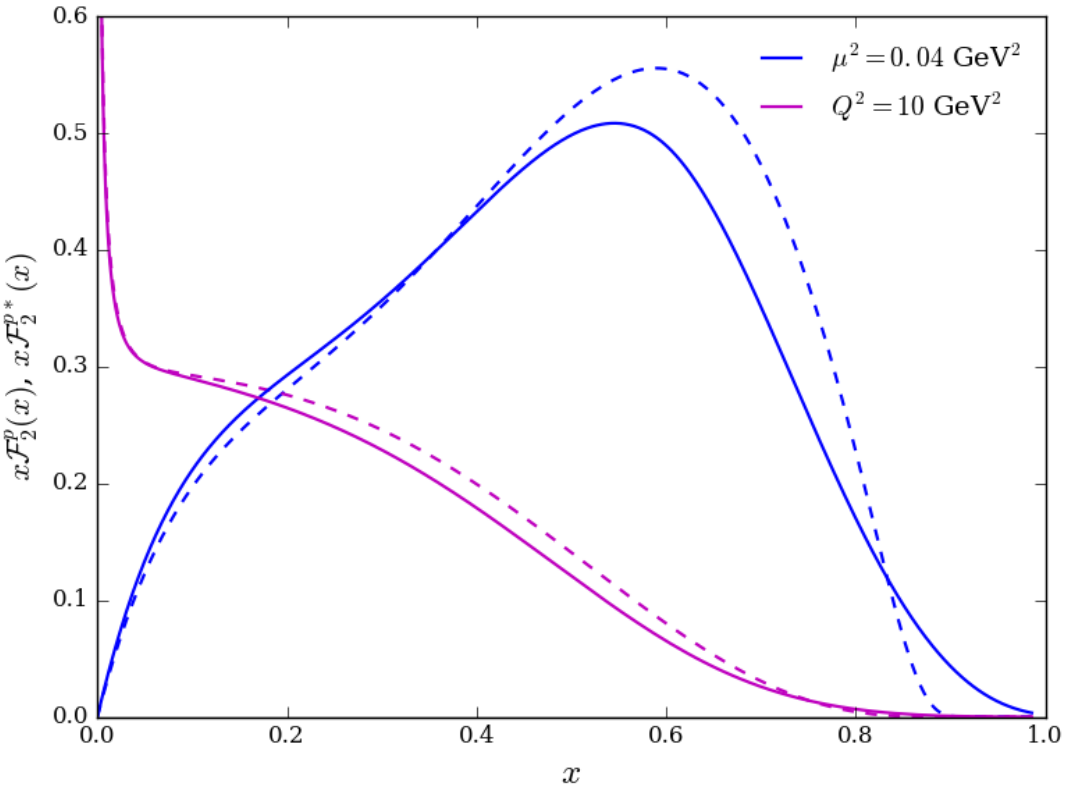

Figure 4.3: Spin-independent structure functions for the proton in the bag model. The dashed lines correspond to the free case and the solid lines correspond to the in-medium case. The larger peaks are at the model scale μ^2, and then evolved to $Q^2 = 10$ GeV^2.

4.5 Chapter Summary

In this chapter we considered the in-medium modifications on a bound nucleon and how this would impact the internal quark structure. We will briefly recap the inclusion of each in-medium modification.

First, the scalar σ mean field is included through the altered quark wave function as well as effective nucleon and diquark state masses. This produces the distribution

$$q_{N_0}^{\uparrow\downarrow}(x) = \frac{M^*}{(2\pi)^2} \sum_m \langle \mu | P_{f,m} | \mu \rangle \int_{\frac{|M^{*2}(1-x)^2 - M_n^{*2}|}{2M^*(1-x)}}^{\infty} p_n dp_n \frac{|\phi_2(\mathbf{p}_n)|^{*2}}{|\phi_3(\mathbf{0})|^{*2}} |\tilde{\Psi}_m^{*\uparrow\downarrow}(\mathbf{p}_n)|^2. \tag{4.22}$$

Next, the Fermi motion of a bound nucleon is included through a convolution with the Fermi smearing function, given in Eq. (4.25), producing the distribution

$$q_{A_0}(\tilde{x}_A) = \int d\tilde{y}_A \, \frac{1}{\tilde{y}_A} \, q_{N_0}\left(\frac{\tilde{x}_A}{\tilde{y}_A}\right) f_0(\tilde{y}_A). \tag{4.29}$$

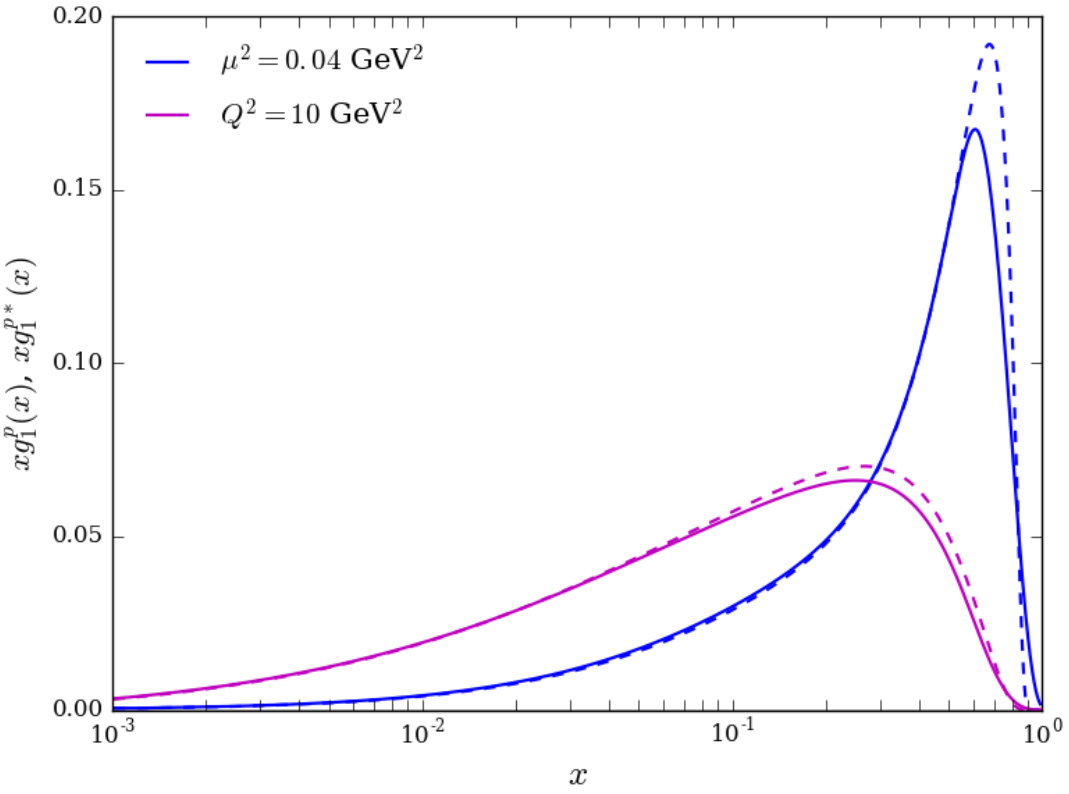

Figure 4.4: Spin-dependent structure functions for the proton in the bag model. The dashed lines correspond to the free case and the solid lines correspond to the in-medium case. The larger peaks are at the model scale μ^2, and then evolved to $Q^2 = 10$ GeV^2.

Finally, the vector ω mean field is included through scaling the distribution and shifting the Bjorken variable to give the distribution

$$q_A(x_A) = \frac{\epsilon_F}{E_F} q_{A_0}\left(\tilde{x}_A = \frac{\epsilon_F}{E_F} x_A - \frac{V_0}{E_F}\right). \tag{4.32}$$

The scalar field is included in the steps for the Fermi motion and the vector field by using the effective nucleon and diquark state masses for in those cases. To compare with the free case, the in-medium distributions can be produced as a function of x through the relation $x_A = \frac{M}{\epsilon_F} x$. With these quark distributions we determined the structure function for a bound nucleon.

We found that by taking the bag model and allowing the quark structure to be altered in-medium, we have observed a suppression in *both* the unpolarized *and* polarized structure functions of a bound nucleon compared to the free case.

Chapter 5

Results

We have described the process for determining the free structure functions of the nucleon, and then the contributions that go into the calculation of the in-medium structure functions. We are now at the stage to take the ratios of these structure functions to see our theoretical prediction of the EMC effect.

We will present the unpolarized EMC ratio for various parameters, and then present the polarized EMC ratio for the same parameters. We will then choose the best parameter set to look at the contribution to the unpolarized and polarized EMC ratios of each in-medium modification considered. When trying different parameters for the bag radius and diquark state masses the model scale varies and so the starting scale for the evolution is dependent on these parameters. Refer to Appendix C for the model scale corresponding to various combinations of radii and diquark state masses.

5.1 Unpolarized EMC Ratios

We will start by looking at the unpolarized EMC ratio for the proton (R_U), which is given by the ratio of the in-medium to free unpolarized structure function of the nucleon;

$$R_U = \frac{F_2^*(x)}{F_2(x)}. \tag{5.1}$$

We will investigate how the unpolarized EMC ratio changes for different values of various parameters.

5.1.1 Changing R

We will first consider how the EMC ratio changes for various choices of bag radius R. Our choice of set parameters is shown in Table 5.1. Apart from the variation in R, these will not be changed. In Table 5.2 we show the resultant values corresponding to various choices of R. In Fig. 5.1 we show the results for the unpolarized EMC ratio of the

Set Values					
R (fm)	$g_\sigma \bar{\sigma}$ (MeV)	p_F (MeV)	M	$M_{n,s}$	$M_{n,v}$
varied	180	220	938.27	550	750

Table 5.1: Set values, where R will be changed. Masses are units MeV.

	Resultant Values					
R (fm)	m_q^*	Ω	V_0 (MeV)	M^*	$M_{n,s}^*$	$M_{n,v}^*$
0.6	-124.51	1.83	39.04	769.12	437.22	637.22
0.8	-124.30	1.75	38.20	772.72	439.63	639.63
1.0	-124.12	1.66	37.37	776.33	442.04	642.04

Table 5.2: Values corresponding to $R = 0.6$, 0.8, and 1.0 fm. Masses are in units MeV.

proton for various bag radii.

From Fig. 5.1 we see that a bag radius of 0.6 fm gives the best fit to the data. To some extent this may be because $R = 0.6$ fm also give the best description of the free structure functions. By giving the quarks a smaller region to move around in, the in-medium modifications have a greater impact on the structure of the bound quarks causing the in-medium structure function to be suppressed to a greater degree compared to a larger bag radius. The general trend of the EMC effect is certainly observed through our approach.

5.1.2 Changing Diquark State Masses

We will now consider how the EMC ratio changes for various choices of diquark state masses $M_{n,s}$ and $M_{n,v}$. Our choice of set parameters is shown in Table 5.3, these will be held constant with only the diquark masses being altered. In Table 5.4 we show the resultant values corresponding to various choices of diquark state masses. In Fig. 5.2 we show the results for the unpolarized EMC ratio of the proton for various diquark state masses.

From Fig. 5.2 we see that as the diquark state masses are made heavier the minimum of the EMC ratio is pushed down and to the left. The best fit to the data in the valence region is for the lightest diquark masses of $M_{n,s} = 550$ MeV and $M_{n,s} = 750$.

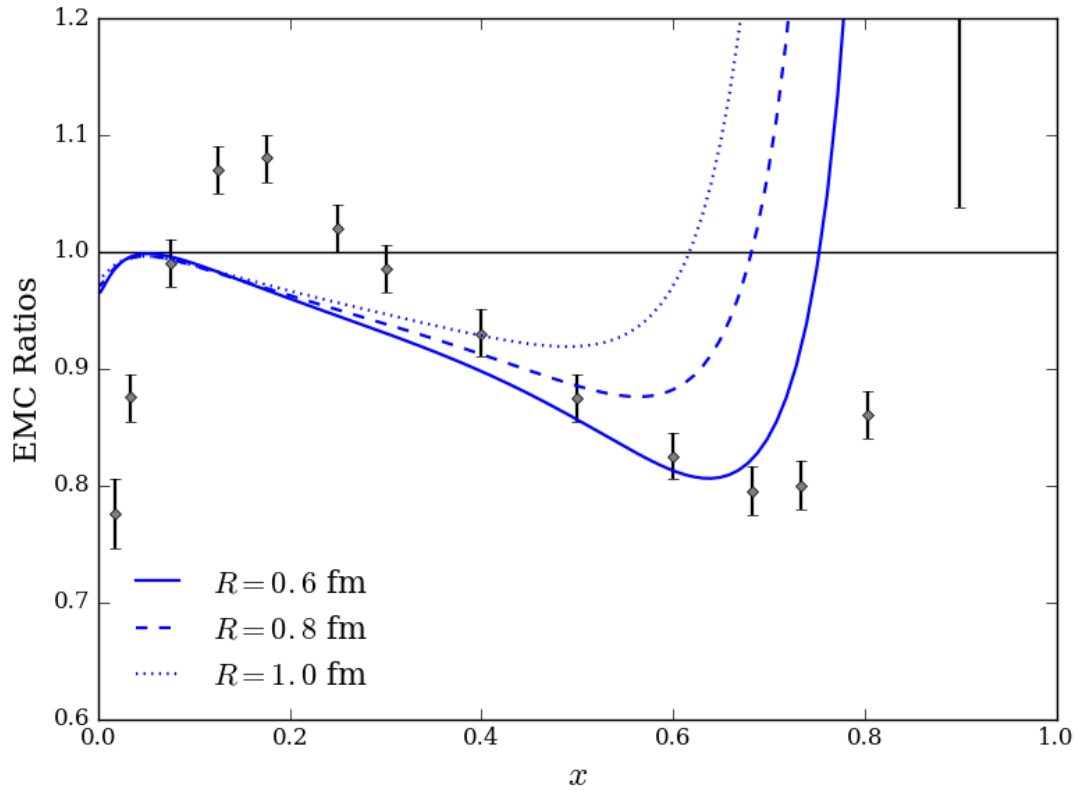

Figure 5.1: Unpolarized EMC ratio for various bag radii. The results are evolved to $Q^2 = 10$ GeV^2. The EMC data for nuclear matter is taken from Ref. [60].

Set Values					
$M_{n,s}$	$M_{n,v}$	R (fm)	$g_\sigma\bar{\sigma}$ (MeV)	p_F (MeV)	M
varied	varied	0.6	180	220	938.27

Table 5.3: Set values, where $M_{n,s}$ and $M_{n,v}$ will be changed. Masses are in units MeV.

5.1.3 Changing $g_\sigma\bar{\sigma}$

We will now consider how the EMC ratio changes for various choices of the coupling strength of the σ mean field, $g_\sigma\bar{\sigma}$. Our choice of set parameters is shown in Table 5.5, these will be held constant with only the σ mean field being altered. In Table 5.6 we show the resultant values corresponding to various choices of the σ mean field. In Fig. 5.3 we show the results for the unpolarized EMC ratio of the proton for various coupling strengths of the σ mean field.

		Resultant Values					
$M_{n,s}$	$M_{n,v}$	m_q^*	Ω	V_0 (MeV)	M^*	$M_{n,s}^*$	$M_{n,v}^*$
550	750	-124.51	1.83	39.04	769.12	437.22	637.22
650	850	-124.51	1.83	39.04	769.12	537.22	737.22
750	950	-124.51	1.83	39.04	769.12	637.22	837.22
850	1050	-124.51	1.83	39.04	769.12	737.22	937.22

Table 5.4: Values corresponding to $(M_{n,s}, M_{n,v}) = (550, 750)$, $(650, 850)$, $(750, 950)$, and $(850, 1050)$ MeV. Masses are in units MeV.

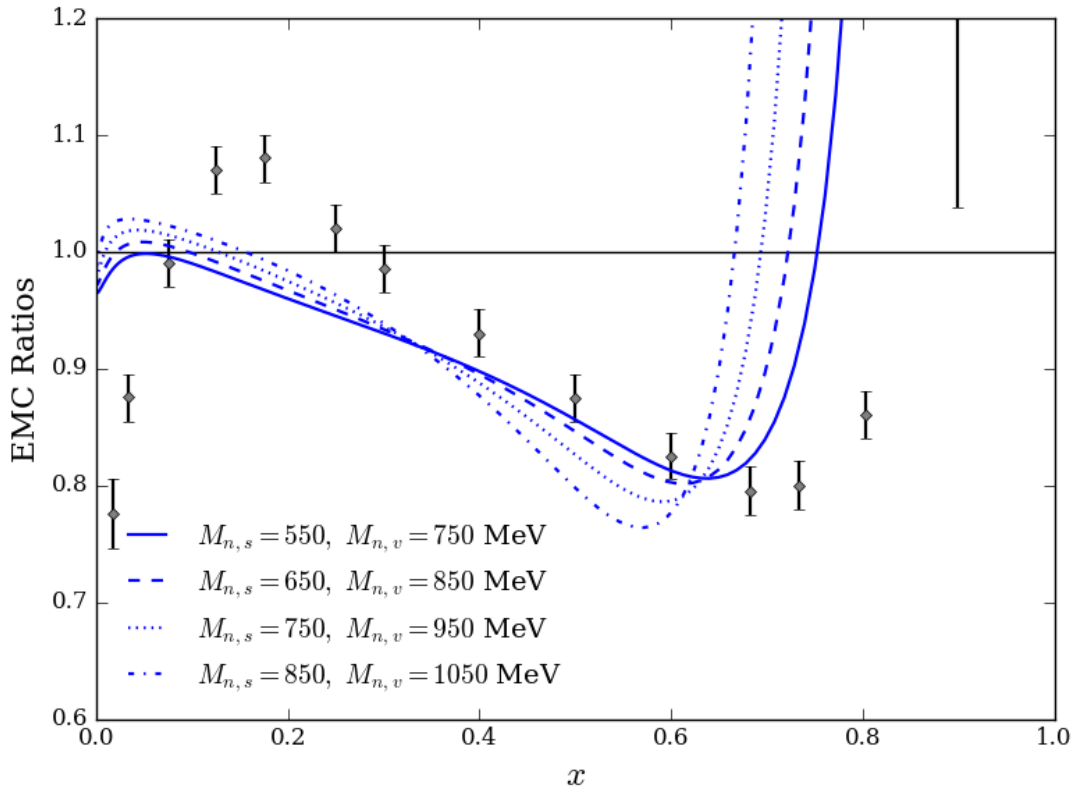

Figure 5.2: Unpolarized EMC ratio for various diquark state masses. The results are evolved to $Q^2 = 10$ GeV^2. The EMC data for nuclear matter is taken from Ref. [60].

From the results in Fig. 5.3 we see that as the coupling strength of the σ mean field is increased the in-medium structure function is suppressed to a greater degree. Therefore, the EMC ratio sits lower for increasing $g_\sigma \bar{\sigma}$. Referring back to Fig. 4.1 we noted that

Set Values					
$g_\sigma\bar{\sigma}$ (MeV)	R (fm)	p_F (MeV)	M	$M_{n,s}$	$M_{n,v}$
varied	0.6	220	938.27	550	750

Table 5.5: Set values, where $g_\sigma\bar{\sigma}$ will be changed. Masses are in units MeV.

	Resultant Values					
$g_\sigma\bar{\sigma}$ (MeV)	m_q^*	Ω	V_0 (MeV)	M^*	$M_{n,s}^*$	$M_{n,v}^*$
180	-124.51	1.83	39.04	769.12	437.22	637.22
200	-138.34	1.81	43.07	751.65	425.59	625.59
220	-152.17	1.78	47.03	734.46	414.13	614.13

Table 5.6: Values corresponding to $g_\sigma\bar{\sigma} = 180$, 200, and 220 MeV. Masses are in units MeV.

at nuclear matter density for a bag radius of $R = 0.6$ fm we had a value of $g_\sigma\bar{\sigma} \simeq 225$ MeV. This value puts the EMC ratio under the data and we find a better fit to valence region for a value of $g_\sigma\bar{\sigma} \simeq 180$ MeV. This is obviously lower than the value shown for the QMC model in Fig. 4.1. However, given the variation possible within the model it is acceptable.

5.1.4 Changing p_F

We will now consider how the EMC ratio changes for various choices of Fermi momentum p_F. Our choice of set parameters is shown in Table 5.7, holding these constant, we will only alter the Fermi momentum. Changing the value of the Fermi momentum does not impact any other values and so the results in Table 5.8 are true for any value of Fermi momentum. In Fig. 5.4 we show the results for the unpolarized EMC ratio of the proton for various choices of Fermi momentum.

Set Values					
p_F (MeV)	R (fm)	$g_\sigma\bar{\sigma}$ (MeV)	M	$M_{n,s}$	$M_{n,v}$
varied	0.6	180	938.27	550	750

Table 5.7: Set values, where p_F will be changed. Masses are in units MeV.

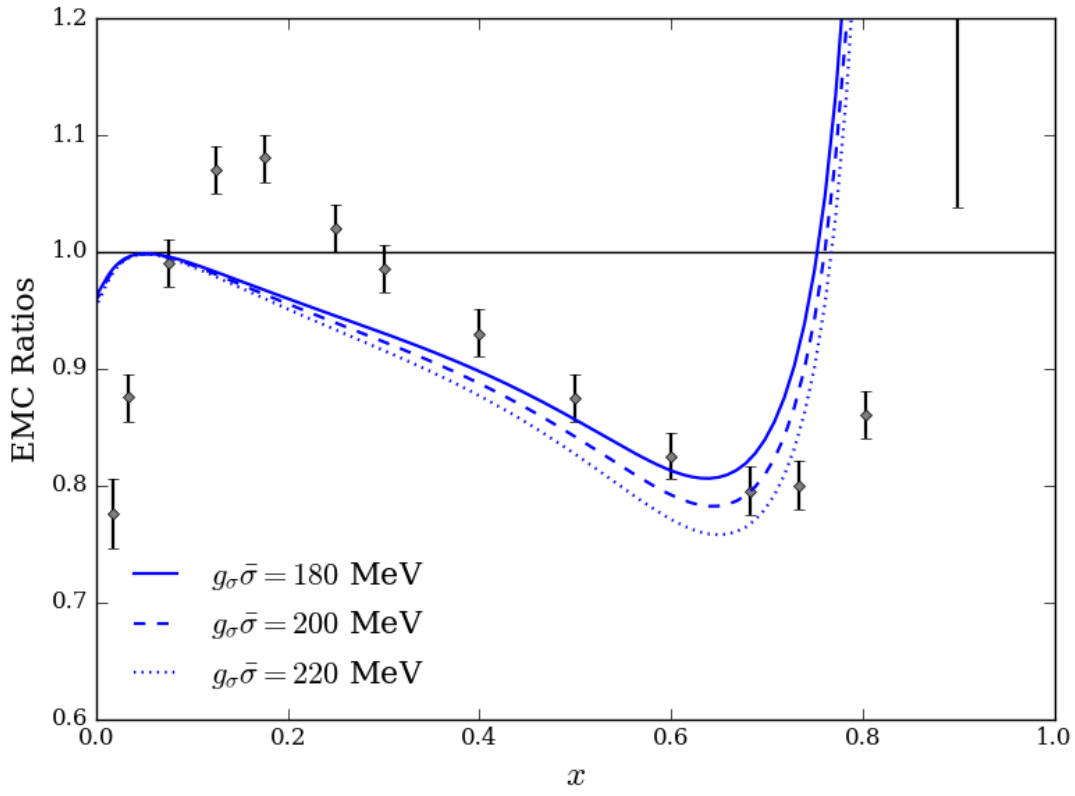

Figure 5.3: Unpolarized EMC ratio for various σ mean field strengths. The results are evolved to $Q^2 = 10$ GeV^2. The EMC data for nuclear matter is taken from Ref. [60].

	Resultant Values					
p_F (MeV)	m_q^*	Ω	V_0 (MeV)	M^*	$M_{n,s}^*$	$M_{n,v}^*$
220, 250, 280	-124.51	1.83	39.04	769.12	437.22	637.22

Table 5.8: Values corresponding to $p_F = 220$, 250, and 280 MeV. Masses are in units MeV.

Fermi momentum corresponds to motion of a bound nucleon and so its effect is predominantly seen in the large-x region. As the Fermi momentum is increased the EMC minimum is pushed up and to the left. From Ref. [74] we see that at nuclear matter density the Fermi momentum is $p_F \simeq 265$ MeV. In our calculations we find dropping the Fermi momentum to a value of 220 MeV gives a better fit to the nuclear matter EMC data in the high-x region.

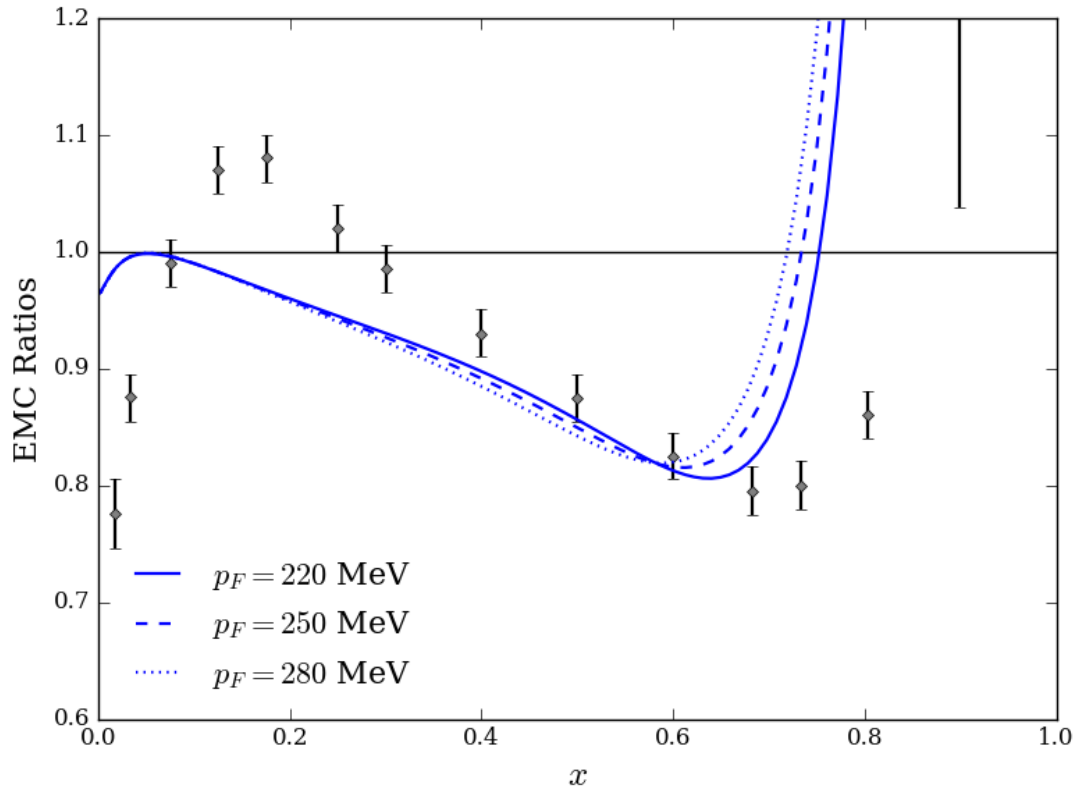

Figure 5.4: Unpolarized EMC ratio for various Fermi momentum p_F. The results are evolved to $Q^2 = 10$ GeV^2. The EMC data for nuclear matter is taken from Ref. [60].

5.1.5 Changing V_0

Finally, we will consider how the EMC ratio changes for various choices of the ω mean field, which corresponds to varying the vector potential V_0. Our choice of set parameters is shown in Table 5.9, these will be held constant, where only the vector potential will be altered. We will not be changing the vector potential directly. If we recall Eq. (4.17) we see that the vector potential is determined through the relation

$$3V_0 = \left(\frac{90}{130}\right)(M - M^*)\,, \tag{4.17}$$

where the ratio 90/130 is the ratio of the vector to scalar potentials at the centre of the hypernuclei lead. We will be varying this ratio of the vector to scalar potential, which is what we use to determine V_0. Hence by varying this ratio we are effectively varying

V_0. We will try three different values:

$$3V_0 = \left(\frac{60}{130}\right)(M - M^*) \quad \Rightarrow \quad V_0 = 26.03, \tag{5.2}$$

$$3V_0 = \left(\frac{90}{130}\right)(M - M^*) \quad \Rightarrow \quad V_0 = 39.04, \tag{5.3}$$

$$3V_0 = \left(\frac{120}{130}\right)(M - M^*) \quad \Rightarrow \quad V_0 = 52.05. \tag{5.4}$$

Changing the value of the vector potential does not impact any other values and so the results in Table 5.10 are true for any value of the vector potential. In Fig. 5.5 we show the results for the unpolarized EMC ratio of the proton for various vector potentials.

Set Values						
V_0 (MeV)	R (fm)	$g_\sigma\bar{\sigma}$ (MeV)	p_F (MeV)	M	$M_{n,s}$	$M_{n,v}$
varied	0.6	180	220	938.27	550	750

Table 5.9: Set values, where V_0 will be changed. Masses are in units MeV.

	Resultant Values				
V_0 (MeV)	m_q^*	Ω	M^*	$M_{n,s}^*$	$M_{n,v}^*$
26.03, 39.04, 52.05	-124.51	1.83	769.12	437.22	637.22

Table 5.10: Values corresponding to $V_0 = 26.03$, 39.04, and 52.05 MeV.

From Fig. 5.5 we see that varying the vector potential has the greatest impact in the mid to high-x region. The EMC ratio is enhanced in the high-x region as the vector potential is increased. Recall that the vector field just shifts the definition of the energy scale, and so by changing the vector field we are simply shifting the quark distributions along the x-axis. Since the quark distributions approach zero quite rapidly for $x \gtrsim 0.7$ the shift is most sensitive in this region.

Of all the parameters tested the EMC ratio is most strongly dependent on the vector potential. The best fit to the nuclear matter EMC data corresponds to a vector potential of $V_0 = 39.04$ MeV. This corresponds to equation

$$3V_0 = \left(\frac{90}{130}\right)(M - M^*)\,, \tag{4.17}$$

where 90/130 is the ratio of the vector to scalar potentials at the centre of the hypernuclei lead as given in Ref. [71].

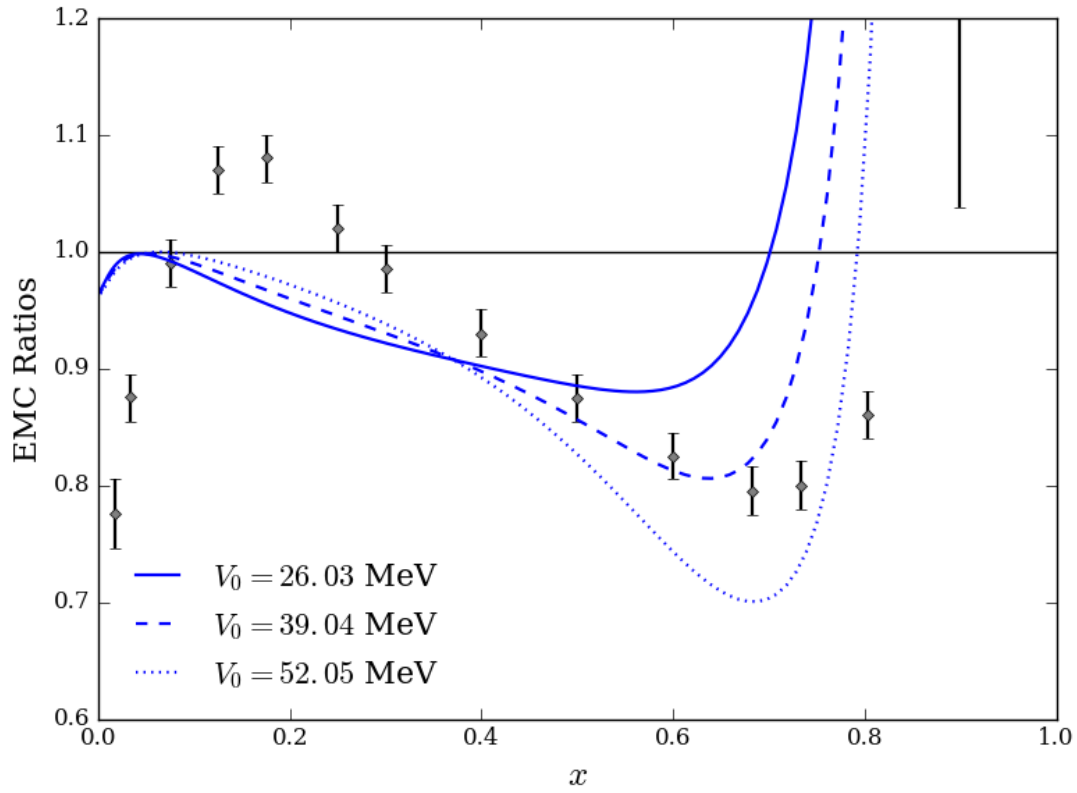

Figure 5.5: Unpolarized EMC ratio for various vector potentials. The results are evolved to $Q^2 = 10$ GeV^2. The EMC data for nuclear matter is taken from Ref. [60].

5.1.6 Best Fit Parameter Set

We will finish off this section by presenting the unpolarized EMC ratio for the parameter set that gives the best fit to the nuclear matter EMC data. Having tried various choices for different parameters, we state the best fit parameter set in Table 5.11, where the vector potential is determined through the relation given in Eq. (4.17). In Fig. 5.6 we present the unpolarized EMC ratio for the best fit parameter set.

From Fig. 5.6 we see that in the region for $x < 0.3$ the theoretical result does not fit the data very well. Since the bag model is a valence picture of the nucleon, and the low-x region is included as an approximation, it is not surprising the theoretical result does not overlap the data in this region. In the valence region for $0.3 < x < 0.7$ the theoretical result is in far better agreement with the data. Overall, while the data is not fitted perfectly, the general trend of the EMC effect is certainly obtained through our approach.

Set Values					
R (fm)	$g_\sigma \bar{\sigma}$ (MeV)	p_F (MeV)	M	$M_{n,s}$	$M_{n,v}$
0.6	180	220	938.27	550	750
Resultant Values					
m_q^*	Ω	V_0 (MeV)	M^*	$M_{n,s}^*$	$M_{n,v}^*$
-124.51	1.83	39.04	769.12	437.22	637.22

Table 5.11: Parameter set resulting in the best fit of the unpolarized EMC ratio to the nuclear matter EMC data. Masses are in units MeV.

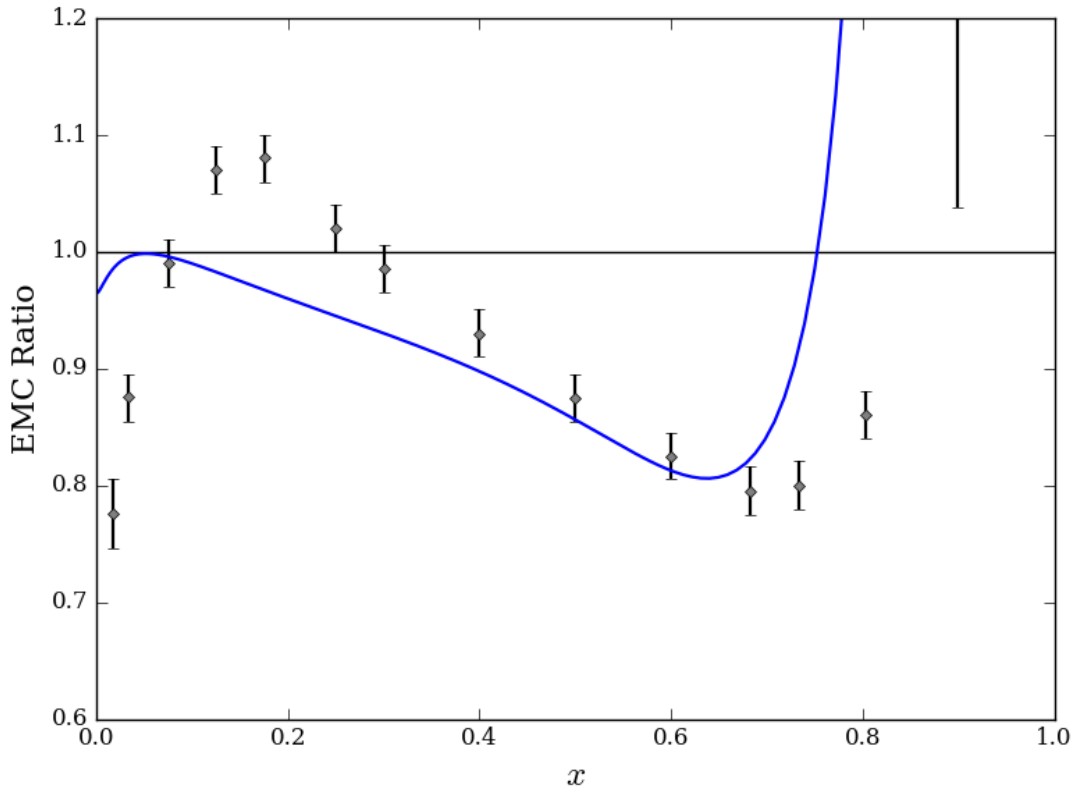

Figure 5.6: Unpolarized EMC ratio for best fit parameter set, shown in Table 5.11. The results are evolved to $Q^2 = 10$ GeV^2. The EMC data for nuclear matter is taken from Ref. [60].

5.2 Polarized EMC Ratios

We will now study the polarized EMC ratio for the proton (R_P), which is given by the ratio of the in-medium to free polarized structure function of the nucleon:

$$R_P = \frac{g_1^*(x)}{g_1(x)}. \tag{5.5}$$

As we did for the unpolarized case, we will examine how our prediction of the polarized EMC ratio changes for different choices of various parameters. In each case we will also include the unpolarized EMC ratio corresponding to the best fit parameter set, shown in Fig. 5.6, as a reference. We will try the same values as we did in the unpolarized case and therefore will not show the tables of values corresponding to the different choices of parameters, since these will be the same as the unpolarized case. We will just refer to these tables for the corresponding case.

5.2.1 Changing R

We will first consider how the polarized EMC ratio changes for various choices of bag radius R. Our choice of set parameters is shown in Table 5.1, and the resultant values corresponding to various choices of R is shown in Table 5.2. In Fig. 5.7 we show the results for the polarized EMC ratio for the proton for various bag radii, along with the unpolarized EMC ratio as a reference.

From Fig. 5.7 we can see that our prediction of the polarized EMC ratio is very similar to our unpolarized prediction. The various choices of R have the same effect on the polarized case as it does on the unpolarized case, which is shown in Fig. 5.1. For the value of $R = 0.6$ fm, which is the preferred value in the unpolarized case, we observe very little difference between the unpolarized and polarized EMC ratio.

5.2.2 Changing Diquark State Masses

We will now consider how the polarized EMC ratio changes for various choices of diquark state masses $M_{n,s}$ and $M_{n,v}$. Our choice of set parameters is shown in Table 5.3, and the resultant values corresponding to various choices of diquark state masses is shown in Table 5.4. In Fig. 5.8 we show the results for the polarized EMC ratio for the proton for various diquark state masses, along with the unpolarized EMC ratio as a reference.

From Fig. 5.8 we can see that changing the diquark state masses has a very similar effect on the polarized case as it does on the unpolarized case, which is shown in Fig. 5.2. The unpolarized case is given at the lightest diquark state masses, and we see little difference between the unpolarized and polarized EMC ratios.

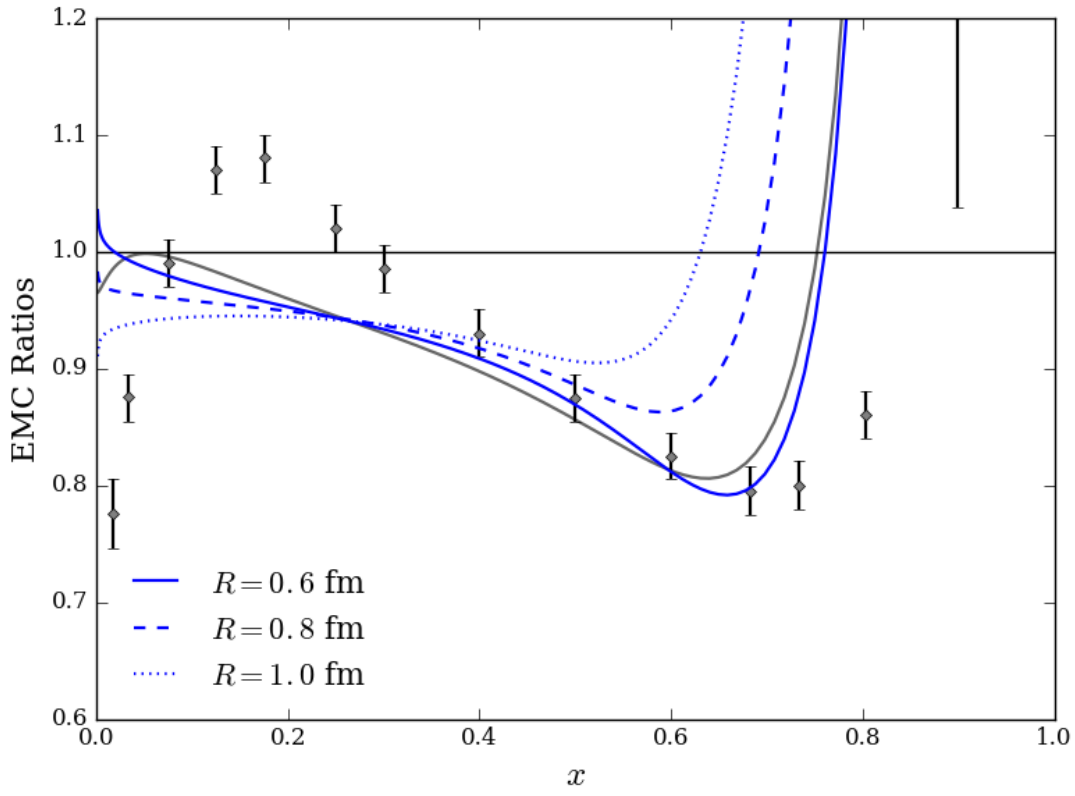

Figure 5.7: Polarized EMC ratio for various bag radii. The results are evolved to $Q^2 = 10$ GeV^2. Our prediction of unpolarized EMC ratio is the solid light grey line with the same parameters with $R = 0.6$ fm. The unpolarized EMC data for nuclear matter is taken from Ref. [60].

5.2.3 Changing $g_\sigma \bar{\sigma}$

We will now consider how the polarized EMC ratio changes for various choices of the coupling strength of the σ mean field, $g_\sigma \bar{\sigma}$. Our choice of set parameters is shown in Table 5.5, and the resultant values corresponding to various choices of the σ mean field is shown in Table 5.6. In Fig. 5.9 we show the results for the polarized EMC ratio for the proton for various coupling strengths of the σ mean field, along with the unpolarized EMC ratio as a reference.

From the results in Fig. 5.9 we see that the coupling strength of the σ mean field has the same effect for the polarized case as for the unpolarized case, which is shown in Fig 5.3, where we see a deeper suppression of the in-medium structure function of the nucleon for larger values of the σ mean field.

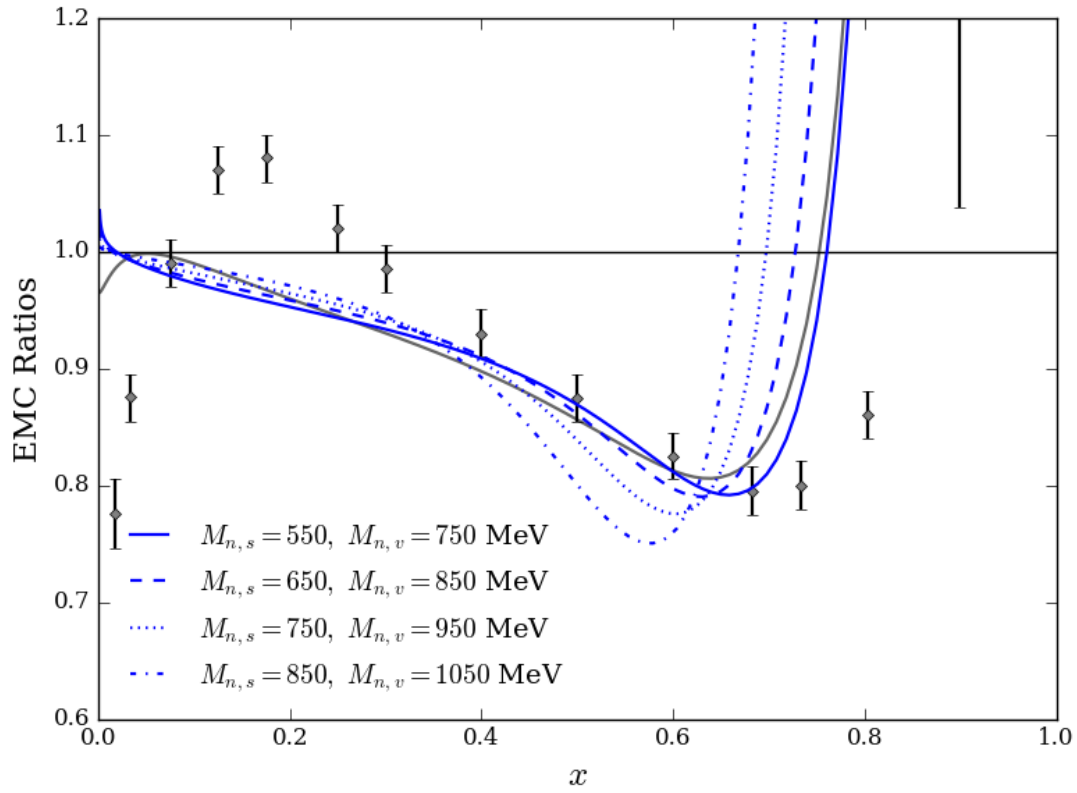

Figure 5.8: Polarized EMC ratio for various diquark state masses. The results are evolved to $Q^2 = 10$ GeV^2. Our prediction of unpolarized EMC ratio is the solid light grey line with the same parameters with $M_{n,s} = 550$ MeV and $M_{n,v} = 750$ MeV. The unpolarized EMC data for nuclear matter is taken from Ref. [60].

5.2.4 Changing p_F

We will now consider how the polarized EMC ratio changes for various choices of Fermi momentum p_F. Our choice of set parameters is shown in Table 5.7, and since changing the Fermi momentum does not impact any other values the results in Table 5.8 are true for any value of Fermi momentum. In Fig. 5.10 we show the results for the polarized EMC ratio for the proton for various values of Fermi momentum, along with the unpolarized EMC ratio as a reference.

From Fig. 5.10 we can see that changing the value of Fermi momentum has the smallest effect on the EMC ratio, this is also true for the unpolarized case, which is shown in Fig. 5.4. The effect of changing the Fermi momentum on the polarized EMC ratio is very similar to the unpolarized case, with the effect being predominantly seen in the large-x region.

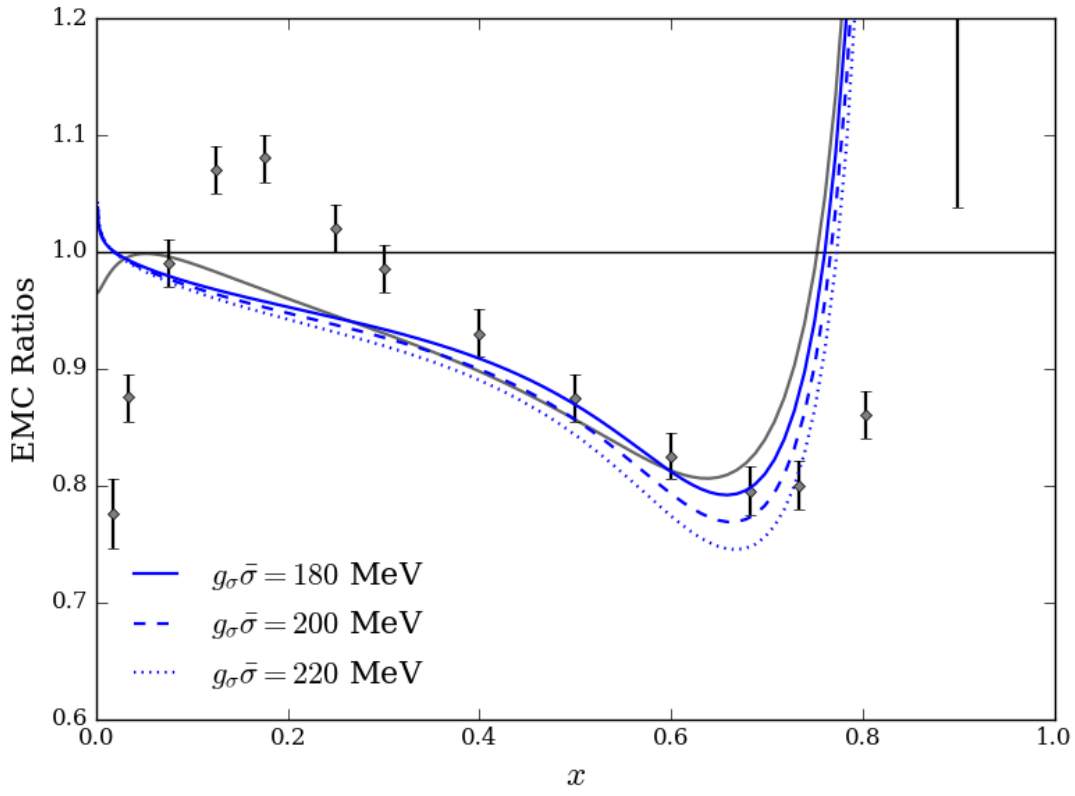

Figure 5.9: Polarized EMC ratio for various σ mean field strengths. The results are evolved to $Q^2 = 10$ GeV^2. Our prediction of unpolarized EMC ratio is the solid light grey line with the same parameters with $g_\sigma\bar{\sigma} = 180$ MeV. The unpolarized EMC data for nuclear matter is taken from Ref. [60].

5.2.5 Changing V_0

Finally, we will consider how the polarized EMC ratio changes for various choices of the ω mean field, which corresponds to varying the vector potential V_0. Our choice of set parameters is shown in Table 5.9. As done in the unpolarized case, we will not vary the vector field directly but will be varying the ratio of the vector to scalar potential, which is what we use to determine V_0. See the unpolarized case (Section 5.1.5) for more detail. Changing the vector potential does not impact any other parameter and so the results in Table 5.10 are true for any value of the vector potential. In Fig. 5.11 we show the results for the polarized EMC ratio for the proton for various vector potentials, along with the unpolarized EMC ratio as a reference.

From Fig. 5.11 we can see that, like the unpolarized case, of all the parameters tested the EMC ratio is most strongly dependent on the vector potential. The effect

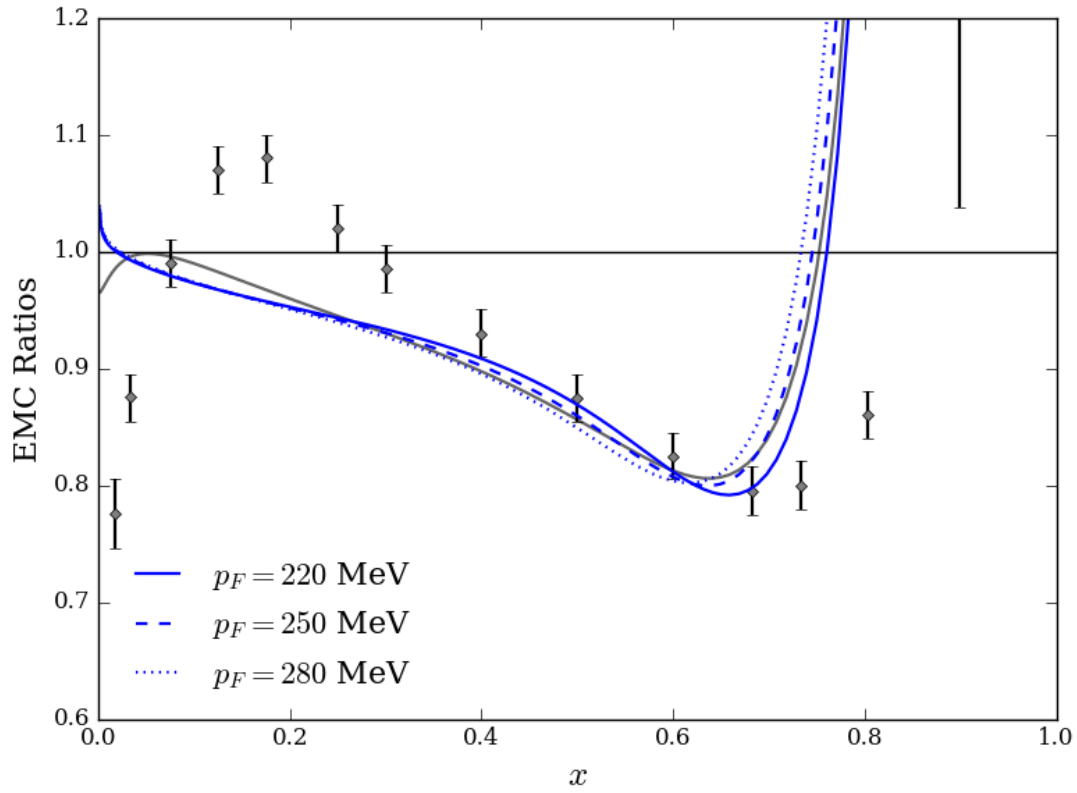

Figure 5.10: Polarized EMC ratio for various Fermi momentum p_F. The results are evolved to $Q^2 = 10$ GeV^2. Our prediction of unpolarized EMC ratio is the solid light grey line with the same parameters with $p_F = 220$ MeV. The unpolarized EMC data for nuclear matter is taken from Ref. [60].

of changing the vector field strength on the polarized EMC ratio is very similar to the unpolarized case, which is shown in Fig. 5.5, where the effect of changing the vector field has the greatest impact in the mid to high-x region.

5.2.6 Best Fit Parameter Set

We will finish this section by presenting both the unpolarized and polarized EMC ratios together for the best fit parameter set found for the unpolarized case, which is given in Table 5.11. In Fig. 5.12 we present our prediction of the unpolarized and polarized EMC ratios together. We are very interested in comparing our prediction of the polarized EMC ratio with that made by Cloët, Bentz and Thomas [1], where they employed modified Nambu-Jona-Lasinio (NJL) model. Therefore, we shall also present their results. In Fig. 5.13 we show the predictions from Ref. [1] for the polarized EMC effect. We shall show the two predictions with the same y-axis scale for easier comparison.

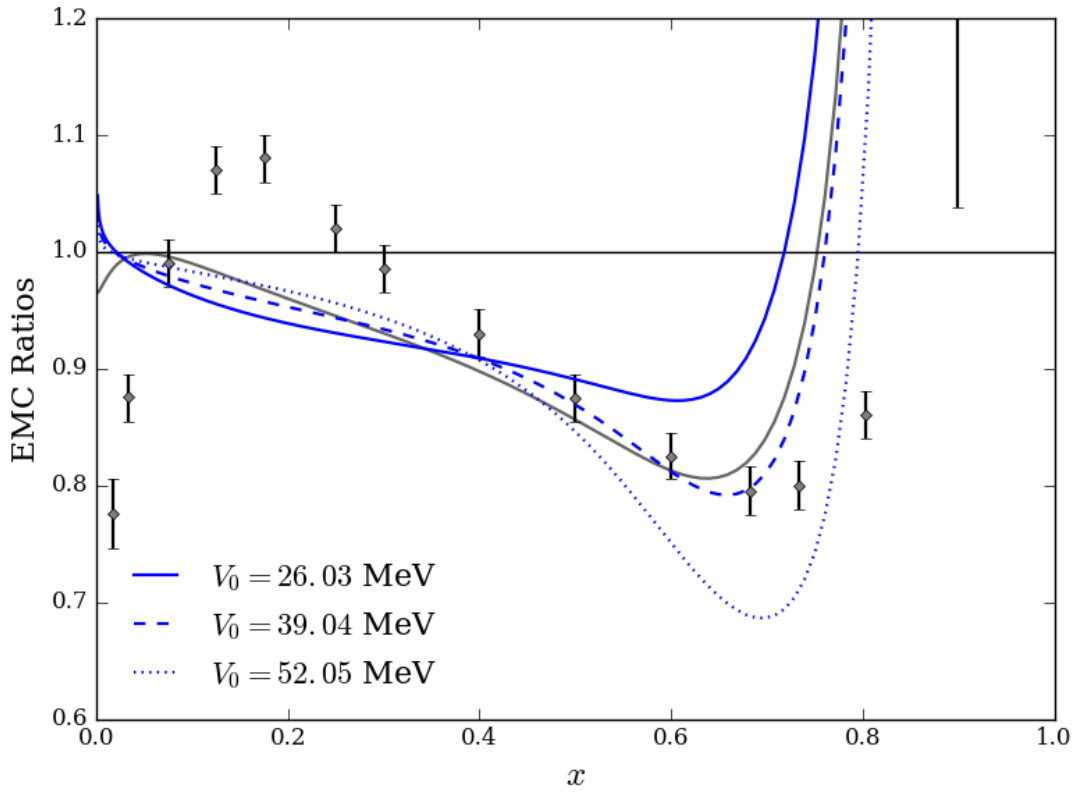

Figure 5.11: Polarized EMC ratio for various vector potentials V_0. The results are evolved to $Q^2 = 10$ GeV^2. Our prediction of unpolarized EMC ratio is the solid light grey line with the same parameters with $V_0 = 39.04$ MeV. The unpolarized EMC data for nuclear matter is taken from Ref. [60].

Our prediction of the polarized EMC ratio along with that of the unpolarized EMC ratio is shown in Fig. 5.12. We can see that through our approach we observe very little difference between the unpolarized and polarized EMC ratios, with the ratio being of the same order in both cases. This is a very interesting result, as it is rather different from the result obtained for the polarized EMC ratio in the NJL model [1], shown in Fig. 5.13. There the polarized EMC ratio is enhanced by about an order twice that compared to the unpolarized case. By taking the bag model and including the quark degrees of freedom in the in-medium calculations through the use of the QMC model, we predict the polarized EMC ratio to be about the same as the unpolarized EMC ratio. Therefore, the enhanced polarized EMC ratio observed in the NJL model appears to be a model dependent phenomena. It will be very exciting to compare the predictions of the polarized EMC ratio to the experimental data. We will make a brief note about the low-x region ($x \lesssim 0.05$), where the unpolarized curve has a small downturn and the

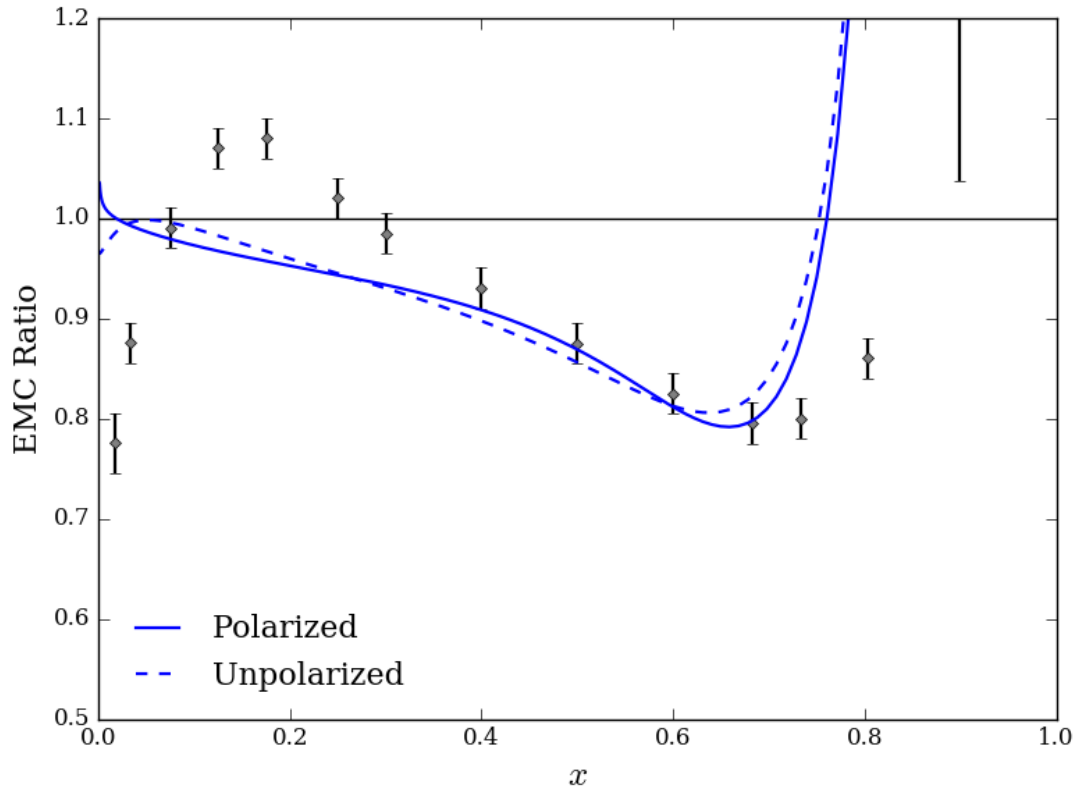

Figure 5.12: Unpolarized and polarized EMC ratio for best fit parameter set for the unpolarized case, shown in Table 5.11. The results are evolved to $Q^2 = 10$ GeV^2. The EMC data for nuclear matter is taken from Ref. [60].

polarized case an upturn. In the model calculations both the ratios tend smoothly up to values of approximately 1.1 for the unpolarized case and 1.05 for the polarized case at $x = 0$. The low-x turns we see here are a result of the QCD evolution.

The results presented in this work are evolved at LO. As a comparison we have produced the next-to-leading order (NLO) results for the unpolarized and polarized EMC ratio and these are presented in Appendix D, where we see little difference between the LO and NLO results.

Recapping our results so far; we have gone through how the changing various parameters effects the EMC ratio for both the unpolarized and polarized case. We observed that changing the strength of the vector field had the greatest impact on the EMC ratio. Having found a best fit parameter set for the unpolarized case, we presented out prediction for the polarized case and found that there is little difference between the two cases in the bag model. This is in contrast to the results found in the NJL model, where the polarized EMC ratio is of order twice that of the unpolarized case.

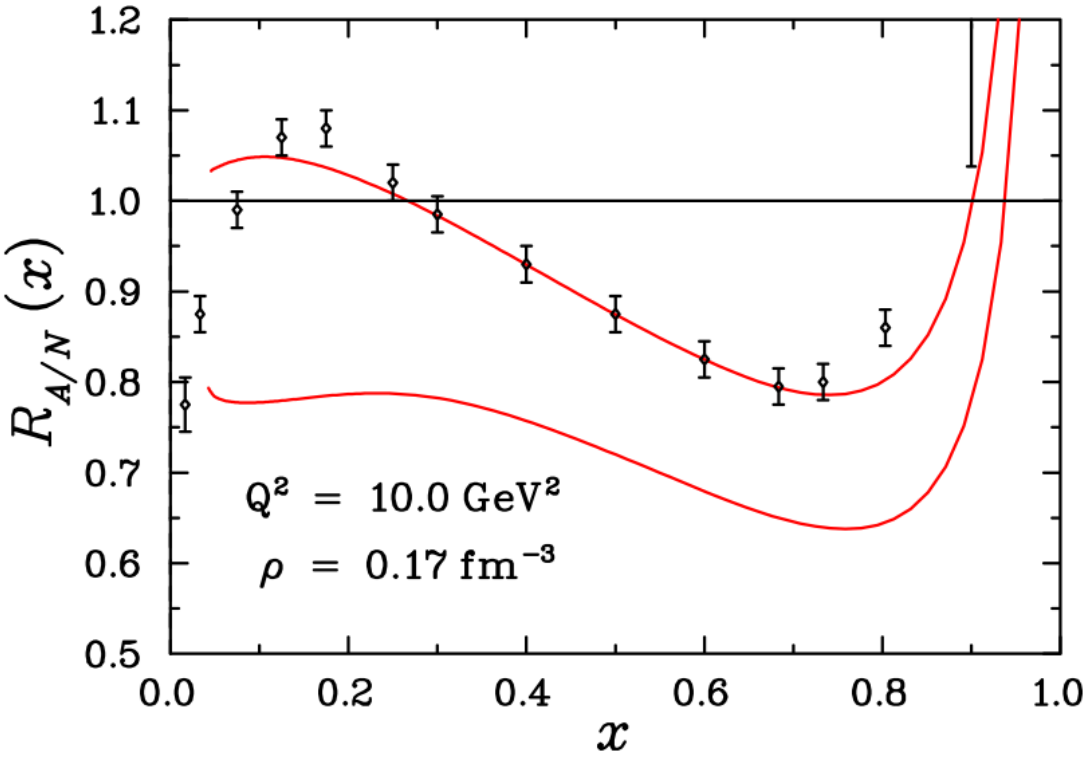

Figure 5.13: Unpolarized and polarized EMC ratio from Ref. [1] where the NJL model was used. The lower curve corresponds to the polarized case. The EMC data for nuclear matter is taken from Ref. [60].

5.3 In-Medium Contributions to the EMC Effect

Having explored the effect of various parameters on the EMC ratio and coming up with the best fit parameter set in the previous section, we are now at the stage to look at the contribution to both the unpolarized and polarized EMC ratio from each in-medium modification included. We will do this by including the in-medium modifications one at a time and looking at how the EMC ratio develops as we do this, where we shall present the results for both the unpolarized and polarized case together at each step. We will start by including the effect of the scalar mean field, this will first be done through the modification to the quark wave function of a bound nucleon, and then through the effective nucleon and diquark state masses, we will then include Fermi motion, and finally include the vector field effects.

5.3.1 σ Mean Field: Wave Function Modification

We will first look at the contribution to the EMC effect from the modified quark wave function caused by the σ mean field. The effect of the σ mean field on the quark wave

function of a bound nucleon is discussed in Section 4.1.1. For this case, when we take the ratio of the in-medium to free structure function of the proton, the in-medium structure function will only contain the altered wave function, we present the results in Fig. 5.14. The values for the parameters are given in Table 5.11.

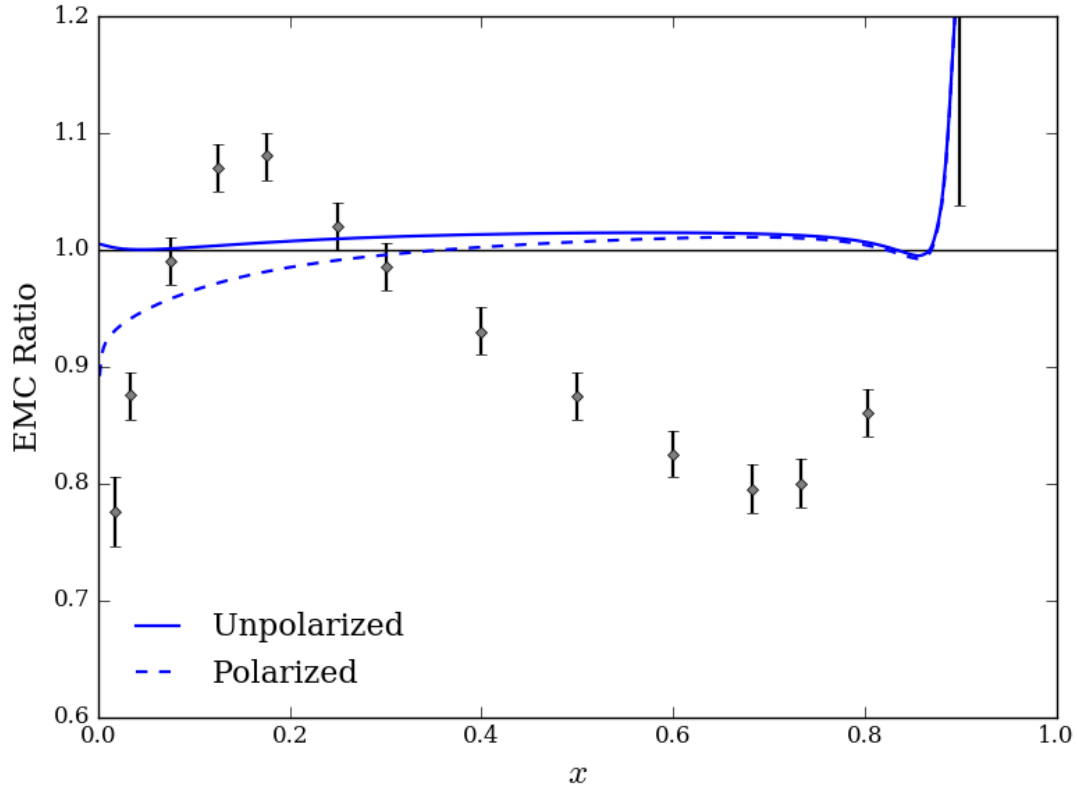

Figure 5.14: Unpolarized and polarized EMC ratio, where only the altered wave function arising from the σ mean field is included in the in-medium structure function. The results are evolved to $Q^2 = 10$ GeV^2. The EMC data for nuclear matter is taken from Ref. [60].

From the result presented in Fig. 5.14 we can see that the altered quark wave function arising from the bound quark experiencing the σ mean field does not play a significant role in producing the EMC effect. The effect is strongest in the polarized case at low-x where the ratio drops below 1 at $x \approx 0.3$ and smoothly decreases to about a value of 0.9 at $x = 0$. Besides the low-x behaviour observed in the polarized case, the ratio for the in-medium to free structure function is approximately unity over the majority of x for the unpolarized case, and at unity over the valence region for the polarized case.

5.3.2 σ Mean Field: Effective Nucleon Masses

We will now extend the effect of the σ mean, and consider the effect of this mean field on the bound nucleon as a whole. The effect of the σ mean field on the bound nucleon is included through the effective nucleon and diquark state masses, as discussed in Section 4.1.2. For this case then, we will be considering the contribution of the total effect of the σ mean field to the EMC effect. Therefore, when we take the ratio of the in-medium to free structure function of the proton, the in-medium structure function will include the effect of both the altered wave function and the effective nucleon and diquark state masses, both arising from the bound nucleon experiencing a σ mean field. We present the results in Fig. 5.15. The values for the parameters are given in Table 5.11.

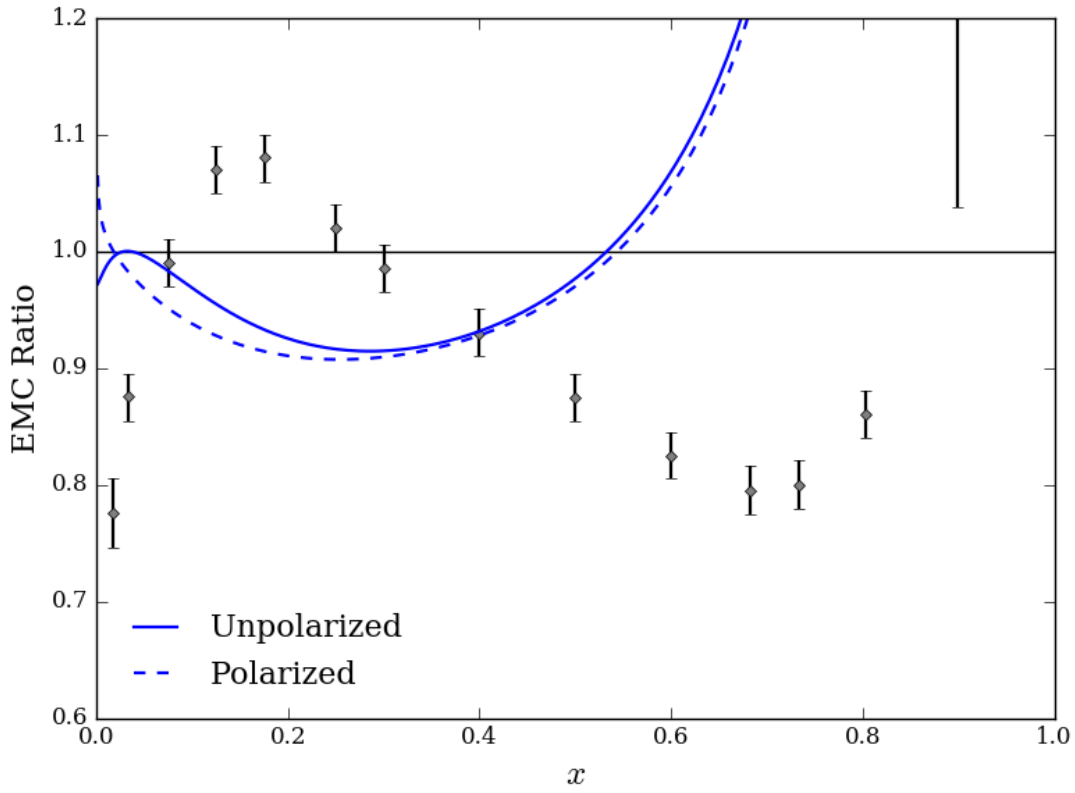

Figure 5.15: Unpolarized and polarized EMC ratio, where only the altered wave function with the altered nucleon and diquark state masses arising from the σ mean field are included in the in-medium structure function. The results are evolved to $Q^2 = 10$ GeV^2. The EMC data for nuclear matter is taken from Ref. [60].

From Fig. 5.15 we can see that introducing the effective nucleon and diquark state masses has a significant effect on the EMC ratio. We are now beginning to see the

trend associated with the EMC effect, where the suppression of the in-medium structure function compared to the free case is becoming apparent, and is seen to occur in the low to mid-x region where the ratio of the in-medium to free structure function of the proton sits below unity. The upward slopping tail has a gradual ascent that starts much earlier compared to the full result. The effective nucleon masses has a similar effect on both the unpolarized and polarized case.

5.3.3 Fermi Motion

We will now extend our calculations to include the effect of Fermi motion on the bound nucleon, which is discussed in Section 4.2. For this case, our bound nucleon will include the effects of σ mean field as well as Fermi motion. Therefore, when evaluating the ratio of the in-medium to free structure function of the proton, the in-medium structure function will include the altered quark wave function with the effective nucleon and diquark state masses, arising from the σ mean field, along with the effect of Fermi motion. We present the results in Fig. 5.16. The values for the parameters are given in Table 5.11.

We can see that the effect of Fermi motion, as taken from the difference between the results in Fig. 5.15 and 5.16, has a relatively small impact on both the unpolarized and polarized EMC ratio. Including Fermi motion into the calculation of the in-medium structure function has the effect of slightly enhancing the EMC ratio where the minimum has been expanded to a small degree and the upward slopping tail now has a more rapid ascent. Overall the effect of Fermi motion does not play a significant role in producing the EMC effect.

It is somewhat interesting that the effect of Fermi motion appears to be so minor. We check the effect of Fermi motion alone without any of the other in-medium modifications in Appendix E.

5.3.4 ω Mean Field: The Vector Potential

Finally, we will extend our calculations to include the of the ω mean field, or vector potential. This is the final effect that is included into the calculations, and incorporating the vector field is discussed in Section 4.3. In this case, we are now considering all in-medium modifications accounted for, and so our in-medium structure function will include; the altered quark wave function with the effective nucleon and diquark state masses, arising from the σ mean field, the effect of Fermi motion, and the vector potential, arising from the ω mean field. We present the result in Fig. 5.17. The values for the parameters are given in Table 5.11.

From the result presented in Fig. 5.17 we can see that the vector potential plays an important role in producing the shape of the EMC effect. The vector potential counters the effect of the σ mean field in the low-x region where the EMC ratio is slightly pushed

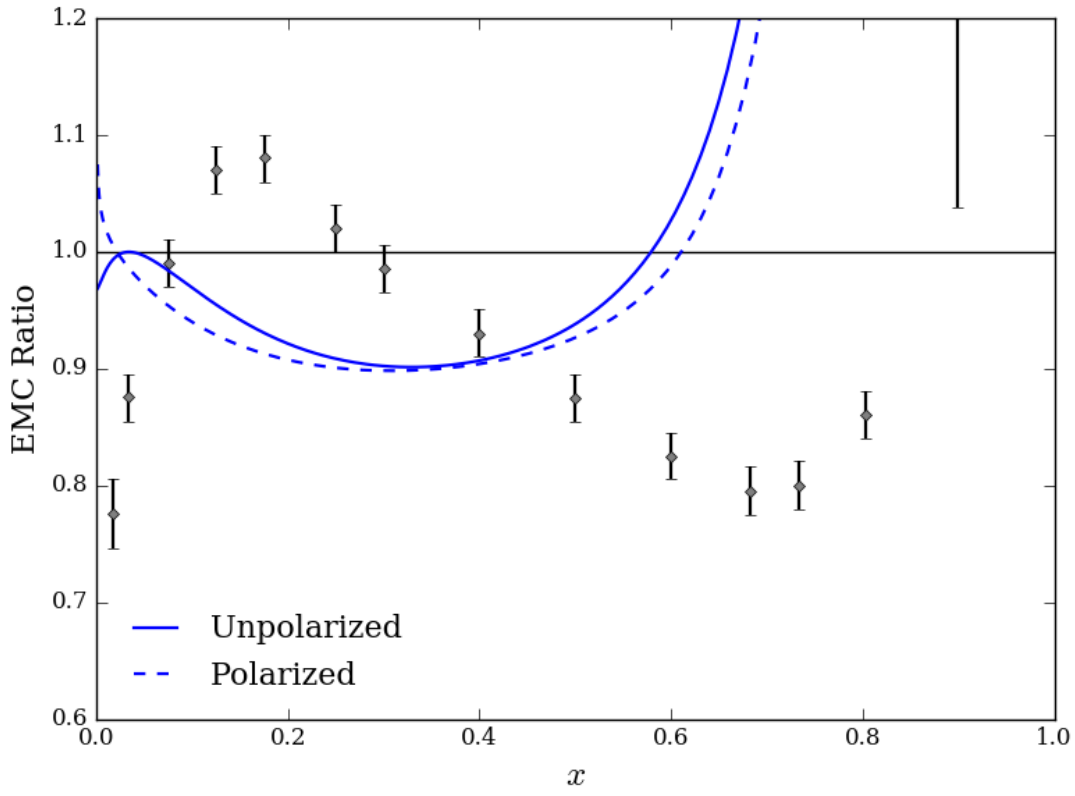

Figure 5.16: Unpolarized and polarized EMC ratio, where only the altered wave function with the effective nucleon and diquark state masses arising from the σ-mean field along with Fermi motion are included in the in-medium structure function. The results are evolved to $Q^2 = 10$ GeV^2. The EMC data for nuclear matter is taken from Ref. [60].

upward toward unity. On the contrary, in the mid to high-x region the vector potential has the effect of drawing down the minimum of the EMC ratio. Hence we see that the vector potential enhances the suppression of the in-medium structure function of the bound nucleon in the mid to high-x region. Overall, the ω mean field, which produces the vector potential, plays a significant role in producing both the unpolarized and polarized the EMC effect.

We will now review this section with the important results. We went through the contribution to both the unpolarized and polarized EMC ratio from each in-medium modification accounted for. We included the in-medium modifications one at a time and watched the EMC ratio develop with each added effect. We found that the altered quark wave function, arising from the σ mean field, as well as the effect of Fermi motion play a minor role in producing the EMC effect. We found the key players in producing

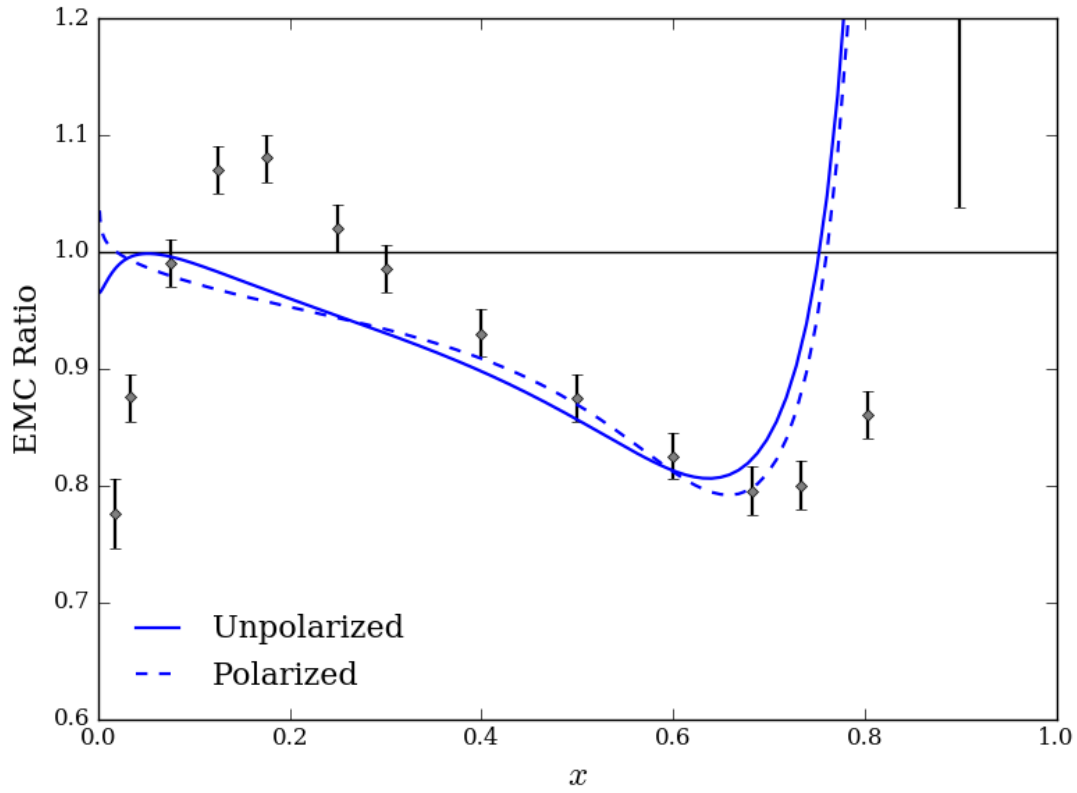

Figure 5.17: Unpolarized and polarized EMC ratio, with all in-medium modifications included; the altered wave function with the altered nucleon and diquark state masses arising from the σ mean field, the effect of Fermi motion, and the vector potential, arising from the ω mean field. The results are evolved to $Q^2 = 10$ GeV^2. The EMC data for nuclear matter is taken from Ref. [60].

the EMC effect are the effect of the σ mean field on the nucleon and the ω mean field. The effective nucleon and diquark state masses, arising from the σ mean field, causes a suppression in the in-medium structure function in the low to mid-x region. The vector potential, arising from the ω mean field, causes a suppression in the in-medium structure function in the mid to high-x region, and also slightly opposes the effect of σ mean field in the low-x region. Hence we find that together, the σ mean field and ω mean field are the dominant contributors to producing the EMC effect in both the unpolarized and polarized case.

5.4 Deuteron Structure Function

We will now discuss a correction that should be made to our calculations. When we determine our unpolarized EMC ratio, the free structure function is that of a free proton.

However, when the EMC ratio is experimentally measured a deuteron target is used. Hence, the ratio actually determined is the structure function of some heavy nucleus, such as lead, divided by the structure function of deuteron. We will apply a correction to account for the fact that the free structure function in experiment actually corresponds to the deuteron, rather than just a free proton, structure function and see how this impacts our result for the EMC ratio. The unpolarized deep inelastic structure function of a relativistic deuteron has been previously investigated by Melnitchouk and Thomas, where they determined the fully off-shell calculation of the deuteron structure function and presented the ratio of the total deuteron to nucleon structure functions [76] [77]. The on-mass-shell calculations have also been determined by Frankfurt and Strikman [78] [79]. In Fig. 5.18 We will present the results of the off-shell and on-shell ratio of the deuteron to nucleon structure function from the previously mentioned references.

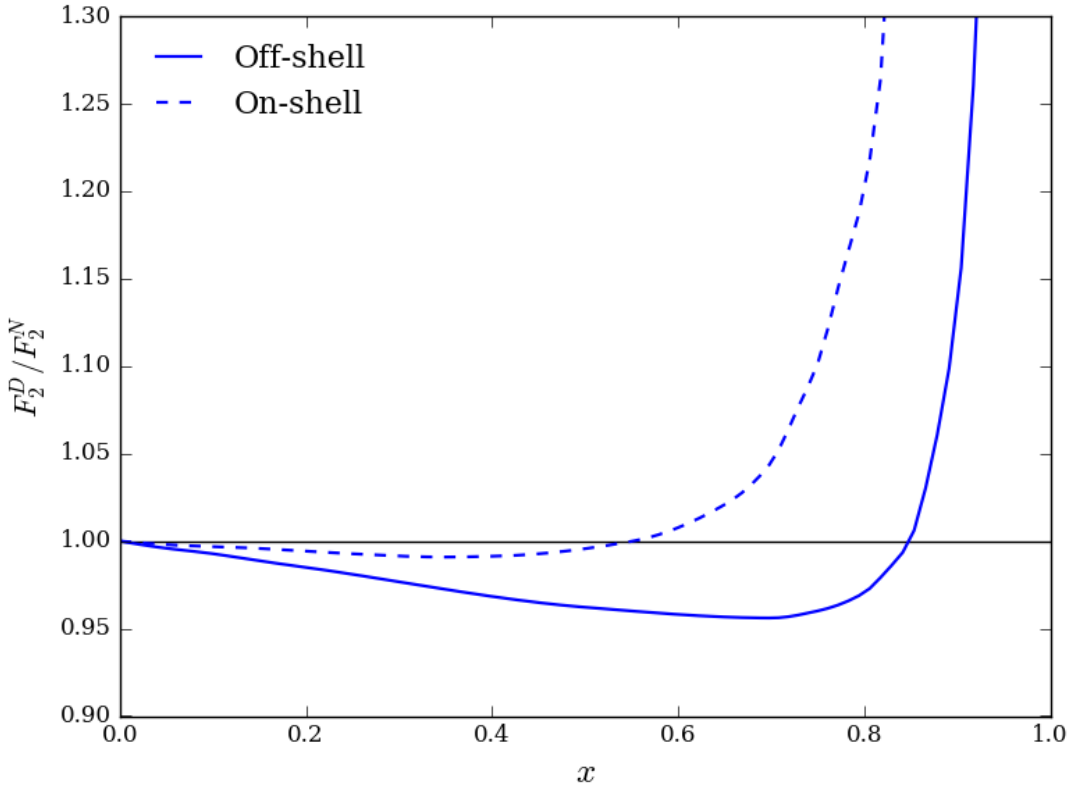

Figure 5.18: Ratio of the deuteron to nucleon unpolarized structure function, F_2^D/F_2^N, as a function of x for the off-shell correction from Refs. [76] [77], and the on-shell correction from Refs. [78] [79]. The results are evolved to $Q^2 = 5$ GeV^2.

The results presented in Fig. 5.18 have been evolved to $Q^2 = 5$ GeV^2, up until this stage we have been evolving all our distributions from the model scale to a scale

of $Q^2 = 10$ GeV^2. Since the evolution progresses logarithmically, the difference in the result from $Q^2 = 5$ GeV^2 to 10 GeV^2 is minor. However, to be consistent we will evolve our unpolarized EMC ratio to a value of $Q^2 = 5$ GeV^2 and then apply both the off-shell and on-shell corrections to see how these impact our result. In Fig. 5.19 we present the result for the off-shell and on-shell deuteron structure function correction applied to the unpolarized EMC ratio, $F_2^*(x)/F_2(x)$.

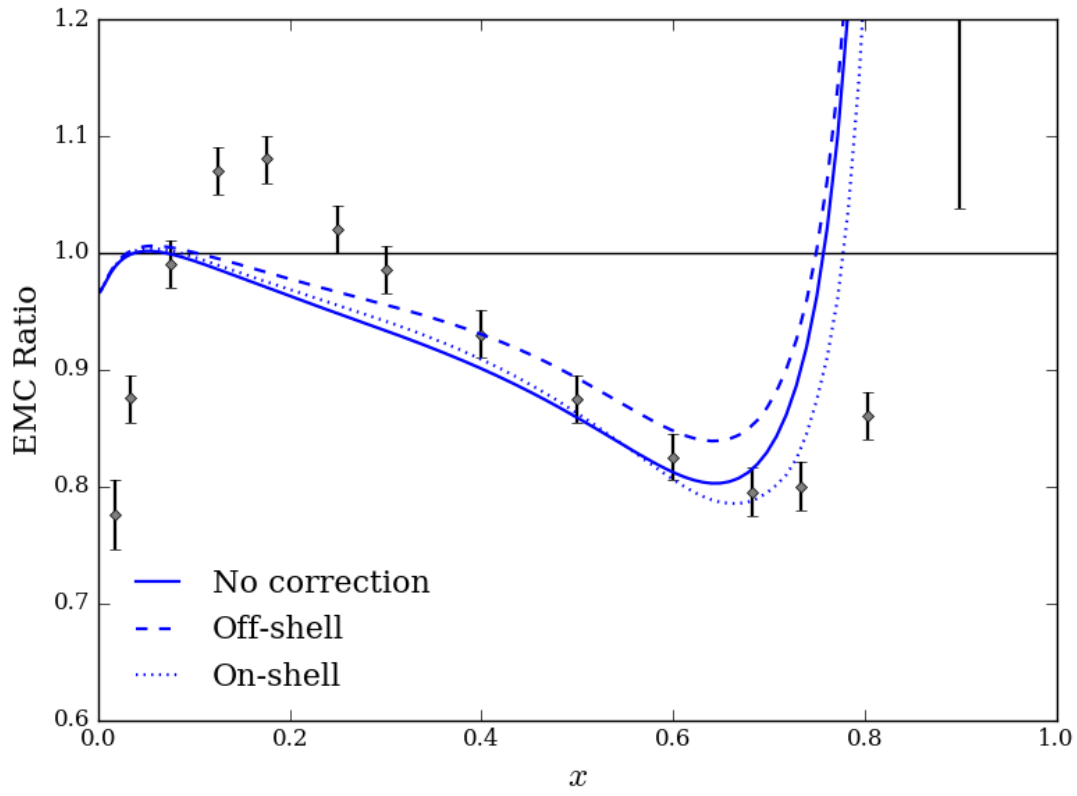

Figure 5.19: Unpolarized EMC ratio with no correction, and with the off-shell and on-shell deuteron structure function corrections applied. The results are evolved to $Q^2 = 5$ GeV^2. The EMC data for nuclear matter is taken from Ref. [60].

The first thing to point out about Fig. 5.19 is that the results are evolved to $Q^2 = 5$ GeV^2, compared to our previous results, which have been evolved to $Q^2 = 10$ GeV^2. This was done so the deuteron corrections could be applied. The nuclear matter EMC data corresponds to $Q^2 = 10$ GeV^2, but this is not a big issue. Take Fig. 5.17 for example, by comparing the unpolarized EMC ratio to that of Fig. 5.19 we can see that the difference between a Q^2 of 5 GeV^2 and 10 GeV^2 is only minor.

The deuteron structure function corrections predominantly impact the mid to high-x region. The off-shell correction gives a better fit to the data in the mid-valence region, as

is also true for the on-shell correction, but to a lesser degree. Toward the upper-valence region the on-shell correction gives a better fit to the data by drawing down the minimum slightly.

Finally, in Fig. 5.20 we present the unpolarized EMC ratio with the deuteron structure function corrections applied, along with our polarized EMC ratio for comparison. We can see that the polarized EMC ratio fits very well with the unpolarized on-shell correction in the mid to high-valence region. On the contrary, the polarized EMC ratio sits under the unpolarized off-shell correction for essentially the entire x region.

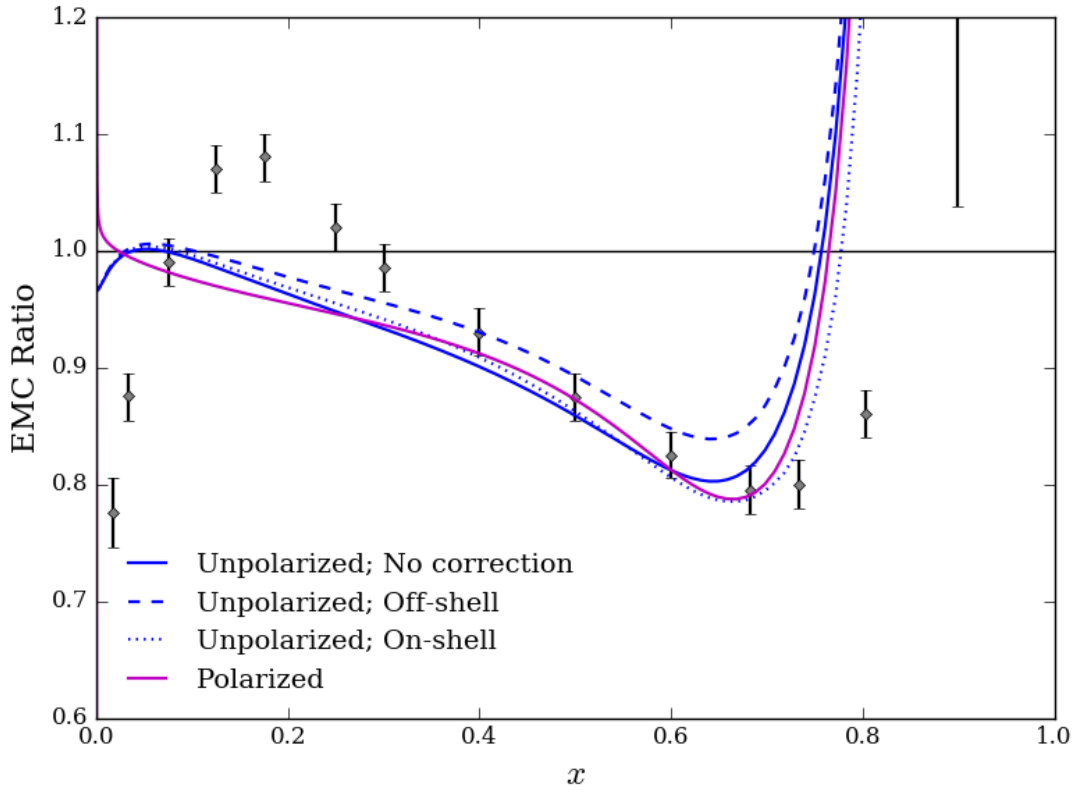

Figure 5.20: Unpolarized EMC ratio with no correction, with the off-shell and on-shell deuteron structure function corrections applied, along the polarized EMC ratio. The results are evolved to $Q^2 = 5$ GeV^2. The EMC data for nuclear matter is taken from Ref. [60].

In Appendix F we look at some more recent phenomenological extractions of the off-shell corrections by Accardi et al. [80], as well as earlier by Kulagin and Petti [81].

5.5 Chapter Summary

In this chapter we presented the results of our investigation into the unpolarized and polarized EMC effect using the bag model. Firstly, we presented our unpolarized EMC ratio and saw how varying different parameters affected the result. We then did the same for our polarized EMC ratio. In both cases we saw that varying the vector potential had the biggest impact on the EMC ratio. Through varying different parameters we found a parameter set that gave the best fit to the EMC data. This parameter set is given in Table 5.11 with the corresponding unpolarized and polarized EMC ratios shown in Fig. 5.12. We found that our prediction of the polarized EMC effect is very similar to our unpolarized prediction. This is in contrast to the prediction from the NJL model, Fig. 5.13 [1], where the polarized EMC effect is of order twice that of the unpolarized effect.

We then went through and included the in-medium modifications step by step into the calculations of the structure function of the bound nucleon so that we could see how each effect contributes to both the unpolarized and polarized EMC ratio. The altered quark wave function of the bound nucleon, arising from the σ mean field, and Fermi motion play a minor role in explaining the EMC effect. The effective nucleon and diquark state masses, arising from the σ mean field, as well as the vector potential, arising from the ω mean field, play the dominant role in producing the EMC effect for both the unpolarized and polarized EMC ratio. The effect of σ mean field is observed in the low to mid-x region and the effect of the vector field is predominantly seen in the mid to high-x region.

Finally, we looked at how the deuteron structure function correction impacts our results. Our EMC ratio was found using the structure function of a free proton, whereas in reality the structure function of deuteron is used. Applying this correction had the biggest impact in the mid to high-x region, where the off-shell correction gave a better fit to the EMC data in the mid-valence region, which was also true for the on-shell correction, but to a lesser degree. Toward the upper-valence region the on-shell correction gave a better fit to the data by drawing down the minimum slightly. Overall, the deuteron correction did not have an overwhelming effect on the results.

Chapter 6

Conclusion

We performed a detailed investigation into the unpolarized and polarized EMC effect using the MIT bag to model the free nucleon, and then applied the mean field approximation along with the QMC model to model the bound nucleon, with the key feature that we included the quark degrees of freedom and hence allowed the internal quark structure of the nucleon to be altered when placed in a nuclear medium.

With the MIT bag model we calculated the unpolarized and polarized structure function of the proton. The u-quark distribution calculated from the bag model was checked against experimental data and found to be in good agreement.

To calculate the structure function of the bound nucleon, we considered the in-medium modifications on the bound nucleon and how this would impact its structure. To start with, we considered the σ mean field, which is first included through the altered quark wave function of the bound nucleon, and then through the effective nucleon and diquark state masses. Next the Fermi motion of a bound nucleon was considered, which is included into the calculations through a convolution with the Fermi smearing function. The final effect we considered was the ω mean field, which gives rise to the vector potential and is included into the calculations through scaling the quark distributions and shifting the Bjorken variable. We then calculated the unpolarized and polarized structure function for the bound proton.

We then produced our EMC ratios for both the unpolarized and polarized case. We changed various parameters to see how this would impact the EMC ratio and observed that changing the strength of the vector potential had the greatest impact on both the unpolarized and polarized EMC ratio. Through testing different parameters we found a parameter set that gave the best fit of the unpolarized EMC ratio to the data. We then presented the unpolarized and polarized EMC ratios with this parameter set and found that there is little difference between the unpolarized and polarized EMC ratios in the bag model. This is an interesting result, as it is in contrast to the results found in the NJL model, where the polarized EMC ratio is of order twice that of the unpolarized

case. Hopefully, there will be data out of JLab in the near future for the polarized EMC effect so the different predictions can be compared with experimental data.

We went through the contribution to both the unpolarized and polarized EMC ratio for each in-medium modification accounted for, where the in-medium modifications were included one at a time and we saw how the EMC ratio developed with each added effect. We found that the altered quark wave function, which arises from the σ mean field, as well as the effect of Fermi motion play a negligible role in producing the EMC effect. The key players in producing the EMC effect, for both the unpolarized and polarized case, are the effect of the σ mean field on the nucleon and the ω mean field. The effective nucleon and diquark state masses, arising from the σ mean field, cause a suppression in the in-medium structure function in the low to mid-x region. The vector potential, arising from the ω mean field, causes a suppression of the in-medium structure function in the mid to high-x region, and also slightly opposes the effect of the σ mean field in the low-x region.

We also applied a deuteron correction to our calculations. This altered our free structure function such that it effectively became that of a deuteron. We checked both the off-shell and on-shell case and found that applying this correction had the biggest impact in the mid to high-x region, where the off-shell correction gave a better fit to the EMC data in the mid-valence region, which was also true for the on-shell correction, but to a lesser degree. Toward the upper-valence region the on-shell correction gave a better fit to the data by drawing down the minimum slightly.

Concluding our most important findings; we found that together, the effective nucleon and diquark state masses arising from σ mean field, and the vector potential arising from the ω mean field are the dominant contributors in producing the EMC effect for both the unpolarized and polarized case. Using the bag model, along with the mean field approximation and QMC model, we found that the polarized EMC effect is essentially the same as the unpolarized EMC effect.

6.1 Future Work

The bag model is a fairly crude model of the nucleon. It would be good to improve on the model. A pion cloud will carry some fraction of the nucleon's momentum and also change its spin-isospin distribution. It would be very interesting to include the pion into the calculations of both the free and in-medium structure function of the nucleon and see how this changes the results.

On the experimental front, we are hoping that JLab will obtain data on the polarized EMC effect shortly, as the proposals have been approved [82]. It is crucial to compare the predictions of polarized EMC effect from different models, such as the bag model, done in this work, and the NJL model, too see which predictions best match the experimental data. This would provide us with further insight into the structure of the

nucleon, as there is no doubt that spin physics has played a crucial role in developing our understanding of the nucleon, among many other things.

Appendix A

Calculation of $|\phi_2(\mathbf{p}_n)|^2$

First we need the overlap integral of the bag wave function,

$$I(x) = \int d\boldsymbol{y}\ \Psi^\dagger(\boldsymbol{y})\ \Psi(\boldsymbol{y}-\boldsymbol{x}), \tag{A.1}$$

where the bag wave function, given in Eq. (3.20) is given by

$$\Psi_m(x) = N \begin{pmatrix} j_0\left(\frac{\Omega|x|}{R}\right)\chi_m \\ i\boldsymbol{\sigma}\cdot\hat{\boldsymbol{x}}\, j_1\left(\frac{\Omega|x|}{R}\right)\chi_m \end{pmatrix} \Theta(R-|x|), \tag{3.20}$$

with the normalisation constant

$$N^2 = \frac{1}{4\pi}\frac{\Omega^3}{2R^3(\Omega-1)sin^2\Omega}, \tag{3.21}$$

resulting in the overlap

$$\begin{aligned} I(x) = N^2 \int d\boldsymbol{y} \Bigg[& j_0\left(\frac{\Omega}{R}\boldsymbol{y}\right) j_0\left(\frac{\Omega}{R}|\boldsymbol{y}-\boldsymbol{x}|\right) \\ & + b^2 j_1\left(\frac{\Omega}{R}\boldsymbol{y}\right) j_1\left(\frac{\Omega}{R}|\boldsymbol{y}-\boldsymbol{x}|\right) \frac{\boldsymbol{\sigma}\cdot\boldsymbol{y}\ \boldsymbol{\sigma}\cdot(\boldsymbol{y}-\boldsymbol{x})}{y|\boldsymbol{y}-\boldsymbol{x}|}\Bigg] \\ & \times\ \theta(R-y)\ \theta(R-|\boldsymbol{y}-\boldsymbol{x}|). \end{aligned} \tag{A.2}$$

The result from the integral, with the substitution $v = |\boldsymbol{x}|\Omega/2R$, is

$$\begin{aligned} I(v) = \frac{\pi N^2 R^3}{\Omega^3 v}\Bigg\{ & \left[(\Omega-v)sin(2v) + (1-sin^2(\Omega)) - cos(\Omega)cos(\Omega-2v)\right] \\ & + \Bigg[\left(1-\frac{4v^2}{2\Omega^2}\right)sin^2(\Omega) - \frac{2}{\Omega}sin(\Omega)cos(\Omega-2v) + \frac{2}{\Omega}sin(\Omega)cos(\Omega) + \Omega sin(2v) \\ & - sin(\Omega)sin(\Omega-2v) - vsin(2v)\Bigg]\Bigg\}, \end{aligned} \tag{A.3}$$

which we will write as

$$I(v) = \frac{\pi N^2 R^3}{\Omega^3 v} \left(T_t(v) + T_b(v)\right), \tag{A.4}$$

where T_t is the first square bracket corresponding to the overlap integral of the top part of the bag wave function, and T_b is the second square bracket corresponding to the overlap integral of the bottom part of the bag wave function. We will define the variable T as the addition of these two components, used in Eq. (3.26), so we have

$$\begin{aligned} T(v) &= T_t(v) + T_b(v) \\ &= \left[(\Omega - v)sin(2v) + (1 - sin^2(\Omega)) - cos(\Omega)cos(\Omega - 2v)\right] \\ &\quad + \left[\left(1 - \frac{4v^2}{2\Omega^2}\right) sin^2(\Omega) - \frac{2}{\Omega} sin(\Omega)cos(\Omega - 2v) + \frac{2}{\Omega} sin(\Omega)cos(\Omega) + \Omega sin(2v)\right. \\ &\quad \left. - sin(\Omega)sin(\Omega - 2v) - vsin(2v)\right]. \end{aligned} \tag{3.26}$$

We are now at the stage to evaluate the expression for the normalization term $|\phi_2(\mathbf{p}_n)|^2$, where we have

$$\begin{aligned} |\phi_2(\boldsymbol{p}_n)|^2 &= 4\pi \int_0^\infty dx\ x^2\ j_0(\mathbf{p}_n x)\ |I(x)|^2 \\ &= 4\pi \int_0^\infty dx\ x^2\ \frac{sin(\boldsymbol{p}_n x)}{\boldsymbol{p}_n x}\ |I(x)|^2 \\ &= 4\pi \int_0^\infty dx\ x\ \frac{sin(\boldsymbol{p}_n x)}{\boldsymbol{p}_n}\ |I(x)|^2, \end{aligned}$$

now using the substitutions

$$v = \frac{|\mathbf{x}|\Omega}{2R}\,, \quad u = |\mathbf{p}_n| R\,, \tag{3.27}$$

we have

$$dx = dv \frac{2R}{\Omega}\,, \quad \mathbf{p}_n x = \frac{2vu}{\Omega}. \tag{A.5}$$

Continuing our calculation for $|\phi_2(\mathbf{p}_n)|^2$ with these substitutions, we have

$$\begin{aligned} |\phi_2(\boldsymbol{p}_n)|^2 &= 4\pi \int_0^\Omega dv\ \frac{2R}{\Omega}\frac{2Rv}{\Omega} sin\left(\frac{2vu}{\Omega}\right)\left(\frac{R}{u}\right)|I(v)|^2 \\ &= \frac{4\pi R}{u} \int_0^\Omega dv\ \left(\frac{2R}{\Omega}\right)^2 v\ sin\left(\frac{2vu}{\Omega}\right)\left(\frac{\pi N^2 R^3}{\Omega^3 v}\right)^2 |T(v)|^2, \end{aligned}$$

which then gives our final expression

$$|\phi_2(\boldsymbol{p}_n)|^2 = \frac{4\pi R}{u}\left(\frac{2\pi N^2 R^4}{\Omega^4}\right)^2 \int_0^\Omega \frac{dv}{v}\ sin\left(\frac{2vu}{\Omega}\right)|T(v)|^2. \tag{3.24}$$

Appendix B

Calculation of $|\phi_3(\mathbf{0})|^2$

Having gone through the overlap integral in Appendix A we can go straight into determining the expression for the normalization term $|\phi_3(\mathbf{0})|^2$. In order to evaluate $|\phi_3(\mathbf{0})|^2$ we will first determine $|\phi_3(\mathbf{p}_n)|^2$, where we have

$$\begin{aligned}|\phi_3(\boldsymbol{p}_n)|^2 &= 4\pi \int_0^\infty dx\; x^3\; j_0(\mathbf{p}_n x)\; |I(x)|^3 \\ &= 4\pi \int_0^\infty dx\; x^3\; \frac{sin(\boldsymbol{p}_n x)}{\boldsymbol{p}_n x}\; |I(x)|^3 \\ &= 4\pi \int_0^\infty dx\; x^2\; \frac{sin(\boldsymbol{p}_n x)}{\boldsymbol{p}_n}\; |I(x)|^3,\end{aligned}$$

using the substitutions found in Eq. (3.27) and (A.5) from Appendix A we have

$$\begin{aligned}|\phi_3(\boldsymbol{p}_n)|^2 &= 4\pi \int_0^\Omega dv\; \frac{2R}{\Omega}\left(\frac{2Rv}{\Omega}\right)^2 sin\left(\frac{2vu}{\Omega}\right)\left(\frac{R}{u}\right)|I(v)|^3 \\ &= \frac{4\pi R}{u}\int_0^\Omega dv\; \left(\frac{2R}{\Omega}\right)^3 v^2\; sin\left(\frac{2vu}{\Omega}\right)\left(\frac{\pi N^2 R^3}{\Omega^3 v}\right)^3 |T(v)|^3,\end{aligned}$$

which then gives us the expression

$$|\phi_3(\boldsymbol{p}_n)|^2 = \frac{4\pi R}{u}\left(\frac{2\pi N^2 R^4}{\Omega^4}\right)^3 \int_0^\Omega \frac{dv}{v}\; sin\left(\frac{2vu}{\Omega}\right)|T(v)|^3. \tag{B.1}$$

The expressions for $I(x)$, $I(v)$, and $T(v)$ can be found in Eqs. (A.2), (A.3), and (3.26), respectively.

To obtain our desired result, we set $\mathbf{p}_n = \mathbf{0}$, which removes the *sin* from the expression as well as an R/u factor. Hence, we arrive at the final expression

$$|\phi_3(\mathbf{0})|^2 = 4\pi\left(\frac{2\pi N^2 R^4}{\Omega^4}\right)^3 \int_0^\Omega \frac{dv}{v}\; |T(v)|^3. \tag{3.25}$$

Appendix C

Model Scale for Various Parameters

R (fm)	$M_{n,s}$ (MeV)	$M_{n,v}$ (MeV)	μ^2 (GeV^2)
0.6	550	750	0.040
0.6	650	850	0.056
0.6	750	950	0.100
0.6	850	1050	0.280
0.8	550	750	0.036
0.8	650	850	0.052
0.8	750	950	0.098
0.8	850	1050	0.260
1.0	550	750	0.034
1.0	650	850	0.050
1.0	750	950	0.096
1.0	850	1050	0.240

Table C.1: Corresponding model scale for various parameters

The parameters that give the best fit of the evolved u-quark distribution to data corresponds to $R = 0.6$ fm, $M_{n,s} = 550$ MeV and $M_{n,v} = 750$ MeV ☺.

Appendix D

EMC Effect at NLO

Our prediction of the unpolarized and polarized EMC effect is evolved at NLO to a scale of $Q^2 = 10$ GeV^2, and compared to the same results evolved at LO. The main difference between the orders of evolution is the value of the model scale, which is the starting scale for the evolution. Our valence u-quark distribution is evolved at NLO and compared to the MSTW2008 NLO valence u-quark distribution [83] to determine the model scale. At LO we previously found that the model scale corresponds to $\mu^2 = 0.04$ GeV^2, while for the evolution at NLO the model scale is much higher at a value of $\mu^2 = 0.20$ GeV^2. We present the results in Fig. D.1.

The NLO results give a slightly better fit to the data, but there is only a minor difference between the LO and NLO results for both the unpolarized and polarized EMC ratio.

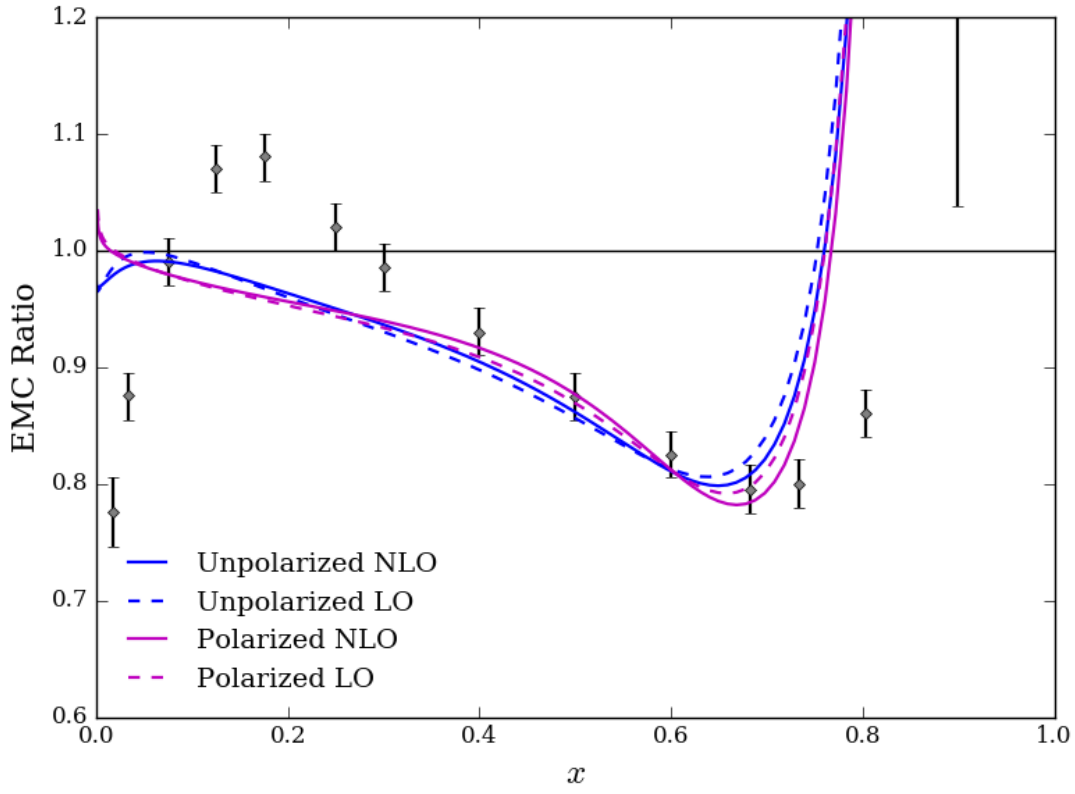

Figure D.1: Unpolarized and polarized EMC ratio. The results are evolved to $Q^2 = 10$ GeV^2 at NLO, corresponding to the solid lines, and at LO, corresponding to the dashed lines. The EMC data for nuclear matter is taken from Ref. [60].

Appendix E

EMC Effect with only Fermi Motion

In Section 5.3.3 we notice that the effect of Fermi motion plays only a minor role in producing the EMC effect for both the unpolarized and polarized case. Here we check the effect of the Fermi motion alone, without any of the other in-medium modifications. Therefore, when evaluating the ratio of the in-medium to free structure function of the proton, the in-medium structure function will include only the effect of Fermi motion, which is discussed in Section 4.2. We present the results in Fig. E.1 for the parameters $R = 0.6$ fm, $M = 938.27$ MeV, $M_{n,s} = 550$ MeV, $M_{n,v} = 750$ MeV, along with a Fermi momentum of $p_F = 220$ MeV for the in-medium structure function.

From Fig. E.1 we do indeed see only a minor effect from Fermi motion, which is consistent with the results presented in Section 5.3.3.

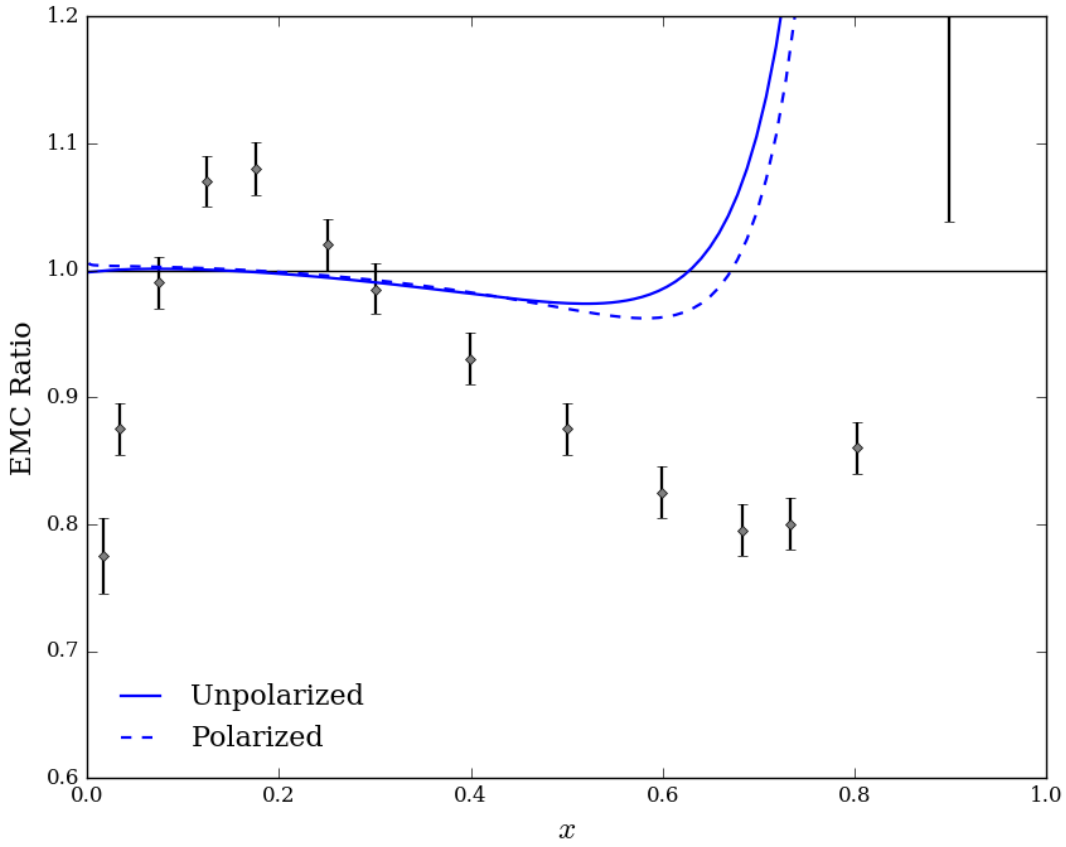

Figure E.1: Unpolarized and polarized EMC ratio, where only Fermi motion is included in the in-medium structure function. The results are evolved to $Q^2 = 10$ GeV^2. The EMC data for nuclear matter is taken from Ref. [60].

Appendix F

Deuteron Correction to the EMC Ratio

We apply the phenomenological extractions of the off-shell deuteron corrections from Accardi et al. [80] as well as Kulagin and Petti [81] to our unpolarized EMC effect. The ratio of the deuteron to nucleon structure function is presented in Fig. F.1. The results from Accardi et al. correspond to Fig. 9 from Ref. [80] where the AV18 curve is reproduced here. The results from Kulagin and Petti correspond to Fig. 13 from Ref. [81] where the uncertainties have not been included.

In Fig. F.2 we present the result of the off-shell deuteron corrections applied to our prediction of the unpolarized EMC ratio, where the values for the parameters are given in Table 5.11. Applying the deuteron correction from Accardi et al. gives a better fit to the EMC data over the majority of x. Applying the correction from Kulagin and Petti gives a very similar result to that presented in Fig. 5.19. It is interesting to see that using the more recent data for the off-shell deuteron correction from Accardi et al. we see a better fit to the data in the mid to high-x region while this was not case for the other off-shell deuteron corrections we looked at. It is also interesting to point out that the off-shell correction of Accardi et al. presented in Fig. F.2 is more reminiscent of the on-shell correction presented in Fig. 5.19.

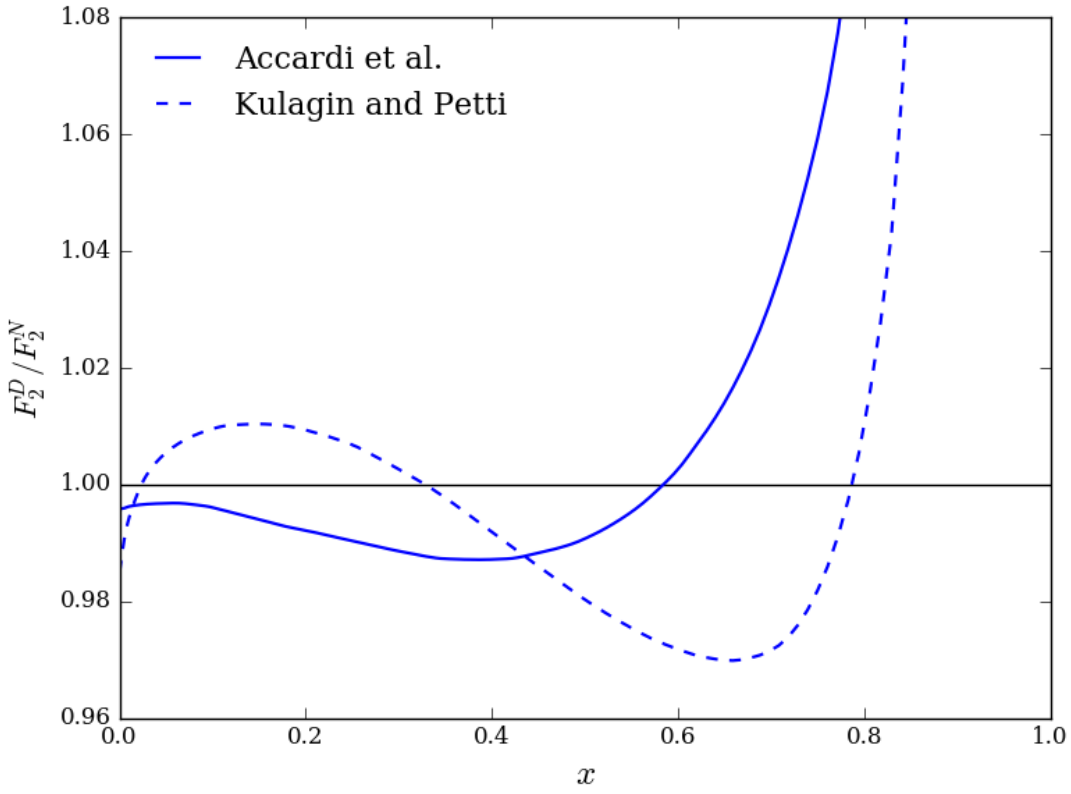

Figure F.1: Ratio of the deuteron to the isoscalar nucleon unpolarized structure function, F_2^D/F_2^N, from Ref. [80] and [81]. The results are evolved to $Q^2 = 10$ GeV^2.

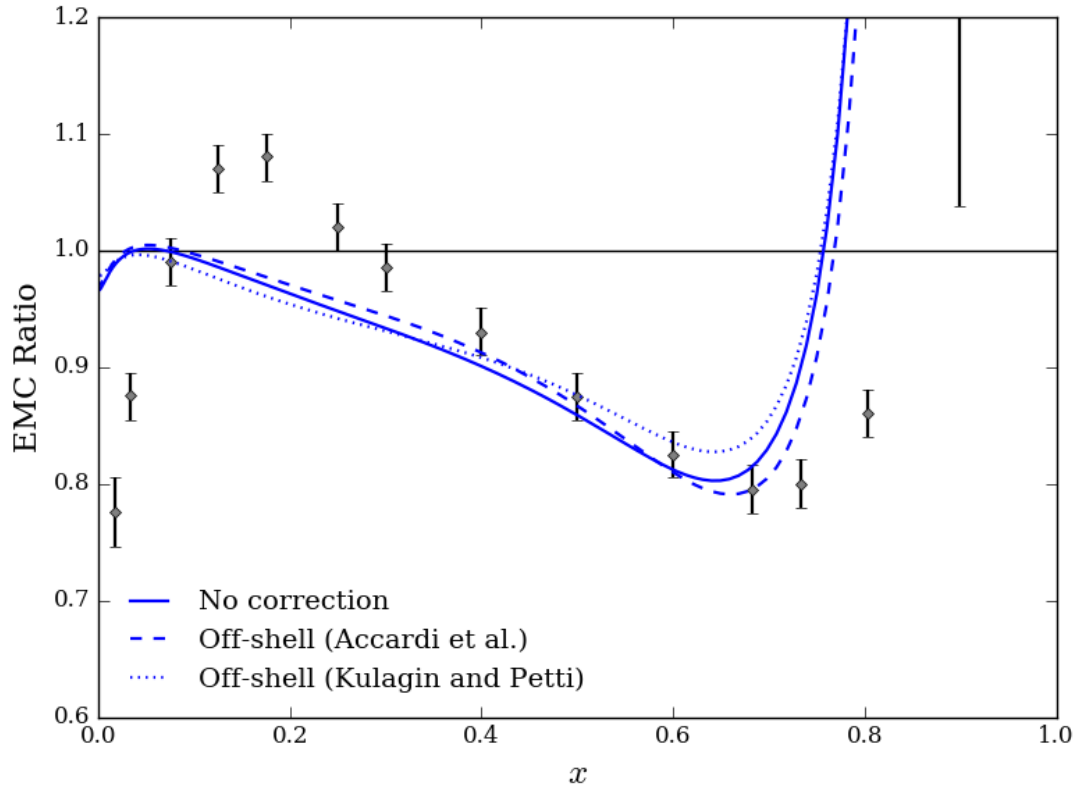

Figure F.2: Unpolarized EMC ratio with no correction, and then with the off-shell deuteron corrections from Ref. [80] and [81] applied. The results are evolved to $Q^2 = 10$ GeV^2. The EMC data for nuclear matter is taken from Ref. [60].

Bibliography

[1] I. C. Cloet, W. Bentz, and A. W. Thomas, "Spin-dependent structure functions in nuclear matter and the polarized EMC effect," *Phys. Rev. Lett.*, vol. 95, p. 052302, 2005.

[2] M. Gell-Mann, "The Eightfold Way: A Theory of Strong Interaction Symmetry," Tech. Rep. Report No. CTSL-20, Caltech Synchrotron Laboratory, 1961.

[3] Y. Ne'eman, "Derivation of strong interactions from a gauge invariance," *Nucl. Phys.*, vol. 26, pp. 222–229, 1961.

[4] M. Gell-Mann, "A Schematic Model of Baryons and Mesons," *Phys. Lett.*, vol. 8, pp. 214–215, 1964.

[5] G. Zweig, "An $SU3$ Model for Strong Interaction Symmetry and its Breaking," Tech. Rep. No. 8419/TH.412, CERN, 1964.

[6] V. E. Barnes *et al.*, "Observation of a Hyperon with Strangeness -3," *Phys. Rev. Lett.*, vol. 12, pp. 204–206, 1964.

[7] H. Filthuth, *Proceedings of the Heidelberg International Conference on Elementary Particles*. Amsterdam: North Holland Pub. Co., 1968.

[8] J. D. Bjorken, "Asymptotic Sum Rules at Infinite Momentum," *Phys. Rev.*, vol. 179, pp. 1547–1553, 1969.

[9] R. P. Feynman, "Very High-Energy Collisions of Hadrons," *Phys. Rev. Lett*, vol. 23, pp. 1415–1417, 1969.

[10] M. S. Chanowitz and S. D. Drell, "Speculations on the Breakdown of Scaling at 10^{-15} cm," *Phys. Rev. Lett.*, vol. 30, p. 807, 1973.

[11] J. Greensite, *An Introduction to the Confinement Problem*. New York: Springer, 2011.

[12] D. J. Gross and F. Wilczek, "Ultraviolet Behavior of Nonabelian Gauge Theories," *Phys. Rev. Lett.*, vol. 30, pp. 1343–1346, 1973.

[13] H. D. Politzer, "Reliable Perturbative Results for Strong Interactions?," *Phys. Rev. Lett.*, vol. 30, pp. 1346–1349, 1973.

[14] A. W. Thomas and W. Weise, *The Structure of the Nucleon*. Berlin: WILEY-VCH, 2001.

[15] C. G. Callan and D. J. Gross, "Crucial Test of a Theory of Currents," *Phys. Rev. Lett.*, vol. 21, pp. 311–313, 1968.

[16] J. T. Londergan and A. W. Thomas, "The Validity of charge symmetry for parton distributions," *Prog. Part. Nucl. Phys.*, vol. 41, pp. 49–124, 1998.

[17] G. Altarelli and G. Parisi, "Asymptotic Freedom in Parton Language," *Nucl. Phys.*, vol. B126, pp. 298–318, 1977.

[18] Y. L. Dokshitzer, "Calculation of the Structure Functions for Deep Inelastic Scattering and e+ e- Annihilation by Perturbation Theory in Quantum Chromodynamics.," *Sov. Phys. JETP*, vol. 46, pp. 641–653, 1977. [Zh. Eksp. Teor. Fiz.73,1216(1977)].

[19] V. N. Gribov and L. N. Lipatov, "Deep inelastic e p scattering in perturbation theory," *Sov. J. Nucl. Phys.*, vol. 15, pp. 438–450, 1972. [Yad. Fiz.15,781(1972)].

[20] M. Botje, "QCDNUM: Fast QCD Evolution and Convolution," *Comput. Phys. Commun.*, vol. 182, pp. 490–532, 2011.

[21] J. J. Aubert *et al.*, "The ratio of the nucleon structure functions $F2_n$ for iron and deuterium," *Phys. Lett.*, vol. B123, pp. 275–278, 1983.

[22] R. G. Arnold *et al.*, "Measurements of the a-Dependence of Deep Inelastic electron Scattering from Nuclei," *Phys. Rev. Lett.*, vol. 52, p. 727, 1984.

[23] S. Stein, W. B. Atwood, E. D. Bloom, R. L. Cottrell, H. C. DeStaebler, C. L. Jordan, H. Piel, C. Y. Prescott, R. Siemann, and R. E. Taylor, "Electron Scattering at 4-Degrees with Energies of 4.5-GeV - 20-GeV," *Phys. Rev.*, vol. D12, p. 1884, 1975.

[24] A. Bodek *et al.*, "Electron Scattering from Nuclear Targets and Quark Distributions in Nuclei," *Phys. Rev. Lett.*, vol. 50, p. 1431, 1983.

[25] P. Amaudruz *et al.*, "Precision measurement of the structure function ratios F2 (He) / F2 (D), F2 (C) / F2 (D) and F2 (Ca) / F2 (D)," *Z. Phys.*, vol. C51, pp. 387–394, 1991.

[26] G. Bari *et al.*, "A Measurement of Nuclear Effects in Deep Inelastic Muon Scattering on Deuterium, Nitrogen and Iron Targets," *Phys. Lett.*, vol. B163, p. 282, 1985.

[27] A. C. Benvenuti *et al.*, "Nuclear Effects in Deep Inelastic Muon Scattering on Deuterium and Iron Targets," *Phys. Lett.*, vol. B189, pp. 483–487, 1987.

[28] J. Ashman *et al.*, "A Measurement of the ratio of the nucleon structure function in copper and deuterium," *Z. Phys.*, vol. C57, pp. 211–218, 1993.

[29] J. Gomez *et al.*, "Measurement of the A-dependence of deep inelastic electron scattering," *Phys. Rev.*, vol. D49, pp. 4348–4372, 1994.

[30] L. Frankfurt, M. Strikman, and S. Liuti, "Nuclear shadowing and the EMC effect," *Nucl. Phys.*, vol. A527, pp. 571C–574C, 1991.

[31] K. A. Olive *et al.*, "Review of Particle Physics," *Chin. Phys.*, vol. C38, p. 090001, 2014.

[32] B. D. Serot and J. D. Walecka, "The Relativistic Nuclear Many Body Problem," *Adv. Nucl. Phys.*, vol. 16, pp. 1–327, 1986.

[33] T. Ueda and A. E. S. Green, "Realistic n-n one-boson-exchange potentials," *Phys. Rev.*, vol. 174, pp. 1304–1312, 1968.

[34] B. Ananthanarayan, G. Colangelo, J. Gasser, and H. Leutwyler, "Roy equation analysis of $\pi\,\pi$ scattering," *Phys. Rept.*, vol. 353, pp. 207–279, 2001.

[35] J. R. Pelaez, "From controversy to precision on the sigma meson: a review on the status of the non-ordinary $f_0(500)$ resonance," *Phys. Rept.*, vol. 658, p. 1, 2016.

[36] W. N. Cottingham, M. Lacombe, B. Loiseau, J. M. Richard, and R. Vinh Mau, "Nucleon nucleon interaction from pion nucleon phase shift analysis," *Phys. Rev.*, vol. D8, pp. 800–819, 1973.

[37] C. Patrignani *et al.*, "Review of Particle Physics," *Chin. Phys.*, vol. C40, no. 10, p. 100001, 2016.

[38] I. C. Cloet, W. Bentz, and A. W. Thomas, "Isovector EMC effect explains the NuTeV anomaly," *Phys. Rev. Lett.*, vol. 102, p. 252301, 2009.

[39] M. H. Johnson and E. Teller, "Classical Field Theory of Nuclear Forces," *Phys. Rev.*, vol. 98, pp. 783–787, 1955.

[40] J. D. Walecka, "A Theory of highly condensed matter," *Annals Phys.*, vol. 83, pp. 491–529, 1974.

[41] R. P. Bickerstaff and A. W. Thomas, "The EMC Effect: With Emphasis on Conventional Nuclear Corrections," *J. Phys.*, vol. G15, pp. 1523–1569, 1989.

[42] M. C. Birse, "Relativistic mean fields and the EMC effect," *Phys. Lett.*, vol. B299, pp. 186–188, 1993.

[43] G. A. Miller and J. R. Smith, "Return of the EMC effect," *Phys. Rev.*, vol. C65, p. 015211, 2002. [Erratum: Phys. Rev.C66,049903(2002)].

[44] J. Zimanyi and S. A. Moszkowski, "Nuclear Equation of state with derivative scalar coupling," *Phys. Rev.*, vol. C42, pp. 1416–1421, 1990.

[45] J. J. Rusnak and R. J. Furnstahl, "Relativistic point coupling models as effective theories of nuclei," *Nucl. Phys.*, vol. A627, pp. 495–521, 1997.

[46] B. D. Serot and J. D. Walecka, "Properties of Finite Nuclei in a Relativistic Quantum Field Theory," *Phys. Lett.*, vol. B87, pp. 172–176, 1979.

[47] A. W. Thomas, "QCD and a New Paradigm for Nuclear Structure," 2016.

[48] P. A. M. Guichon, "A Possible Quark Mechanism for the Saturation of Nuclear Matter," *Phys. Lett.*, vol. B200, pp. 235–240, 1988.

[49] F. Bissey, F.-G. Cao, A. Kitson, B. G. Lasscock, D. B. Leinweber, A. I. Signal, A. G. Williams, and J. M. Zanotti, "Gluon field distribution in baryons," *Nucl. Phys. Proc. Suppl.*, vol. 141, pp. 22–25, 2005. [,22(2005)].

[50] P. A. M. Guichon, H. H. Matevosyan, N. Sandulescu, and A. W. Thomas, "Physical origin of density dependent force of the skyrme type within the quark meson coupling model," *Nucl. Phys.*, vol. A772, pp. 1–19, 2006.

[51] P. A. M. Guichon, G. Q. Liu, and A. W. Thomas, "Virtual Compton scattering and generalized polarizabilities of the proton," *Nucl. Phys.*, vol. A591, pp. 606–638, 1995.

[52] K. Saito and A. W. Thomas, "A microscopic understanding of the structure functions of finite nuclei," *Nucl. Phys.*, vol. A574, pp. 659–684, 1994.

[53] K. Tsushima, K. Saito, and A. W. Thomas, "Selfconsistent description of Lambda hypernuclei in the quark - meson coupling model," *Phys. Lett.*, vol. B411, pp. 9–18, 1997. [Erratum: Phys. Lett.B421,413(1998)].

[54] K. Tsushima, K. Saito, J. Haidenbauer, and A. W. Thomas, "The Quark - meson coupling model for Lambda, Sigma and Xi hypernuclei," *Nucl. Phys.*, vol. A630, pp. 691–718, 1998.

[55] D.-H. Lu, A. W. Thomas, K. Tsushima, A. G. Williams, and K. Saito, "In-medium electron - nucleon scattering," *Phys. Lett.*, vol. B417, pp. 217–223, 1998.

[56] P. A. M. Guichon, K. Saito, E. N. Rodionov, and A. W. Thomas, "The Role of nucleon structure in finite nuclei," *Nucl. Phys.*, vol. A601, pp. 349–379, 1996.

[57] K. Saito, K. Tsushima, and A. W. Thomas, "Selfconsistent description of finite nuclei based on a relativistic quark model," *Nucl. Phys.*, vol. A609, pp. 339–363, 1996.

[58] K. Saito, K. Tsushima, and A. W. Thomas, "Variation of hadron masses in finite nuclei," *Phys. Rev.*, vol. C55, pp. 2637–2648, 1997.

[59] P. A. M. Guichon, K. Saito, and A. W. Thomas, "Quarks in finite nuclei," *Austral. J. Phys.*, vol. 50, pp. 115–122, 1997.

[60] I. Sick and D. Day, "The EMC effect of nuclear matter," *Phys. Lett.*, vol. B274, pp. 16–20, 1992.

[61] A. Chodos, R. L. Jaffe, K. Johnson, C. B. Thorn, and V. F. Weisskopf, "A New Extended Model of Hadrons," *Phys. Rev.*, vol. D9, pp. 3471–3495, 1974.

[62] T. Muta, *Foundations of Quantum Chromodynamics.* Singapore: World Scientific, 2010.

[63] A. W. Schreiber, A. I. Signal, and A. W. Thomas, "Structure functions in the bag model," *Phys. Rev. D*, vol. 44, pp. 2653–2662, Nov 1991.

[64] R. L. Jaffe, "Relativistic dynamics and quark-nuclear physics," in *Proceedings of the Workshop, Los Alamos, New Mexico, 1985, edited by M. B Johnson and A. Pickleseimer*, Wiley, New York, 1985.

[65] R. L. Jaffe, "Parton Distribution Functions for Twist Four," *Nucl. Phys.*, vol. B229, pp. 205–230, 1983.

[66] R. E. Peierls and J. Yoccoz, "The Collective model of nuclear motion," *Proc. Phys. Soc.*, vol. A70, pp. 381–387, 1957.

[67] A. W. Thomas, "Chiral Symmetry and the Bag Model: A New Starting Point for Nuclear Physics," *Adv. Nucl. Phys.*, vol. 13, pp. 1–137, 1984.

[68] F. E. Close, *An Introduction to Quarks and Partons.* United Kingdom: Academic Press, 1979.

[69] F. E. Close and A. W. Thomas, "The Spin and Flavor Dependence of Parton Distribution Functions," *Phys. Lett.*, vol. B212, pp. 227–230, 1988.

[70] A. Sherstnev and R. S. Thorne, "Parton Distributions for LO Generators," *Eur. Phys. J.*, vol. C55, pp. 553–575, 2008.

[71] K. Saito, K. Tsushima, and A. W. Thomas, "Nucleon and hadron structure changes in the nuclear medium and impact on observables," *Prog. Part. Nucl. Phys.*, vol. 58, pp. 1–167, 2007.

[72] P. A. M. Guichon and A. W. Thomas, "Quark structure and nuclear effective forces," *Phys. Rev. Lett.*, vol. 93, p. 132502, 2004.

[73] H. Mineo, W. Bentz, N. Ishii, A. W. Thomas, and K. Yazaki, "Quark distributions in nuclear matter and the EMC effect," *Nucl. Phys.*, vol. A735, pp. 482–514, 2004.

[74] E. J. Moniz, I. Sick, R. R. Whitney, J. R. Ficenec, R. D. Kephart, and W. P. Trower, "Nuclear Fermi momenta from quasielastic electron scattering," *Phys. Rev. Lett.*, vol. 26, pp. 445–448, 1971.

[75] I. C. Cloet, W. Bentz, and A. W. Thomas, "Spin-dependent parton distributions in the nucleon," *Nucl. Phys. Proc. Suppl.*, vol. 141, pp. 225–232, 2005. [,225(2005)].

[76] A. W. Thomas and W. Melnitchouk, "Deuteron structure functions in the context of few body physics," *Nucl. Phys.*, vol. A631, pp. 296C–315C, 1998.

[77] W. Melnitchouk, A. W. Schreiber, and A. W. Thomas, "Relativistic deuteron structure function," *Phys. Lett.*, vol. B335, pp. 11–16, 1994.

[78] L. L. Frankfurt and M. I. Strikman, "On the Problem of Neutron Structure Function Extraction from Deep Inelastic e d Scattering," *Phys. Lett.*, vol. 76B, pp. 333–336, 1978.

[79] L. L. Frankfurt and M. I. Strikman, "High-Energy Phenomena, Short Range Nuclear Structure and QCD," *Phys. Rept.*, vol. 76, pp. 215–347, 1981.

[80] A. Accardi, L. T. Brady, W. Melnitchouk, J. F. Owens, and N. Sato, "Constraints on large-x parton distributions from new weak boson production and deep-inelastic scattering data," *Phys. Rev.*, vol. D93, no. 11, p. 114017, 2016.

[81] S. A. Kulagin and R. Petti, "Global study of nuclear structure functions," *Nucl. Phys.*, vol. A765, pp. 126–187, 2006.

[82] P. Bosted, W. Brooks, V. Dharmawardane, R. Ent, S. Kuhn, and D. Crabb, "The emc effect in spin structure functions," 2005.

[83] A. D. Martin, W. J. Stirling, R. S. Thorne, and G. Watt, "Parton distributions for the LHC," *Eur. Phys. J.*, vol. C63, pp. 189–285, 2009.